# Correlated Studies of Spectral and Timing Aspects of X-ray Binaries

A dissertation submitted to

THE DEPARTMENT OF PHYSICS
UNIVERSITY OF CALICUT
CALICUT, KERALA

in partial fulfilment of the requirements
for the degree of

## Doctor of Philosophy

in the subject of

## Physics

under the Faculty of Science
by

## Blessy Elizabeth Baby
URSC, Bengaluru

Thesis advisors :
**Dr. Ramadevi M. C., URSC, ISRO**
**Dr. C. D. Ravikumar, Department of Physics, University of Calicut**

May 2024

# CERTIFICATE

This is to certify that the thesis titled "**Correlated Studies of Spectral and Timing Aspects X-ray Binaries**" submitted to the Department of Physics, University of Calicut by **Blessy Elizabeth Baby** in partial fulfilment of the requirements of the award of **Doctor of Philosophy** is a bonafide record of the work done by her, under our joint supervision and that no part of it has been included anywhere previously for the award of any degree, either in this university or any other institution. The thesis has been checked for plagiarism, using the OURIGINAL software, at the CHMK Library, University of Calicut and the similarity index is found within the permissible limit. Also, no changes were suggested by the thesis referees after evaluation, and therefore, there are no further changes to be made in this thesis.

**Dr. Ramadevi M. C.,**
Scientist 'SF',
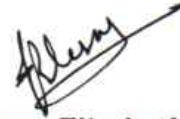Space Astronomy Group (SAG),
URSC, Bengaluru.

**Dr. C. D. Ravikumar,**
Professor,
University of Calicut,
Calicut, Kerala.

iii

# Declaration of Authorship

I hereby declare that the thesis titled "**Correlated Studies of Spectral and Timing Aspects of X-ray Binaries**" is an authentic record of the research work carried out by me under the supervision of Dr. Ramadevi M. C, URSC and Dr. C. D. Ravikumar, Department of Physics, University of Calicut. No part of this thesis has formed the basis for any award or any other degree or diploma in any university or institution. The thesis has been checked for plagiarism, using the OURIGINAL software, at the CHMK Library, University of Calicut and the similarity index is found within the permissible limit.

Date: 08|05|2024

**Blessy Elizabeth Baby**
Research Scholar
Department of Physics
University of Calicut

iv

*DEDICATED TO MY PAPPAJI.....*

# Acknowledgements

Thesis advisors:
Dr. Ramadevi M. C., URSC, ISRO
Dr. C. D. Ravikumar, Department of Physics, University of Calicut   Blessy E. Baby

# Correlated Studies of Spectral and Timing Aspects of X-ray Binaries

## Abstract

X-ray Binaries (XRBs) are a class of binaries which emit in X-rays. They consist of a compact object, which could be a White Dwarf, Neutron Star or a Black Hole, in orbit with a normal companion star. Black Hole Binaries (BHBs) are XRBs in which the compact object is a Black Hole. BHBs are studied in pursuit of a better understanding of physics in extreme gravity. The physical processes behind the origin of X-ray radiation has been the subject of many studies. Although direct imaging of the sources is next to impossible, spectral and temporal analysis of BHBs can help us 'see' the nature and geometry of the sources.

Transient BHBs are interesting systems which remain in quiescence for a long period of time but show occasional flaring activity, recurring at different timescales. These flares or 'outbursts' are often accompanied by changes in both spectral and temporal properties. Over the last few decades, the sources have been found to undergo various phases or 'states' in a specific order during an outburst, which are classified as canonical outbursts. In the present studies, we focus on different sources which do not conform to the accepted picture of the canonical outbursts. We perform a comparative study on the nature of the outbursts and attempt to understand the physical processes which drive them.

We begin with a brief introduction to different topics like types of X-ray binaries, radiation processes, the evolution of an outburst and the various states associated with them, and so on in **Chapter 1**. The instruments used to obtain data from these sources and the reduction methods are detailed in **Chapter 2**. For instruments with a large Field of View (FOV), like *Large Area X-ray Proportional Counter (LAXPC)* onboard *AstroSat*, contamination from other sources in the FOV is a challenging issue to be dealt with, while performing spectral analysis. A complete section is dedicated to the method followed to minimize the effects of contamination in such cases in the second half of Chapter 2.

We study three such BHB sources in this work - 4U1630-472, MAXI J0637-430 and Swift J1753.5-0127 in subsequent chapters. 4U 1630-472 is a recurrent X-ray binary, which exhibits two different types of outbursts, called 'mini' and 'super'-outbursts. We focus on the 2016 and 2018 'mini'-outbursts of the source in **Chapter 3**. The primary instrument used for analysis is the Indian multi-wavelength astronomy satellite *AstroSat*. The source was initially known to re-

Thesis advisors:
Dr. Ramadevi M. C., URSC, ISRO
Dr. C. D. Ravikumar, Department of Physics, University of Calicut    Blessy E. Baby

main in the disc-dominant state throughout the outburst. The initial transition from a low/hard state to an intermediate state is observed for the first time using *AstroSat* during its 2016 outburst. The transition occurred within a span of $\sim 11$ hrs, which was not caught by any pointed instrument previously. The Hardness Intensity Diagram (HID) seems to follow a 'c'- shaped profile instead of the generally accepted 'q' shaped profile observed for BHBs. We also attempt to establish a link between 'mini'-outbursts and the 'super'-outbursts, by comparing the HIDs of the 'mini'-outbursts in 1998 and 1999, and the HID of the 'super'-outburst of 2002-2004. The spectra are fit using both phenomenological and physical models. Classification into states is performed based on the phenomenological modelling. We also fit the spectra using a two component flow model and comment on the accretion parameters. Mass estimation of the compact object is also obtained from three different methods.

MAXI J0637-430 is a relatively new transient source discovered on 2 November 2019, which seems to share some of its properties with the BHB 4U 1630-472. Apparently, this source also remained in the soft state for the most part of the outburst. Similar to 4U 1630-472, no Quasi periodic Oscillations (QPOs) are observed in the Power Density Spectra (PDS). As with the source 4U 1630-472, we perform spectral fits using phenomenological and physical models and try to divide the outburst into different states. We also obtain mass estimates using different methods. We try to establish a possible link between the two sources by studying the individual HID patterns. Finally, we comment on the underlying physical mechanisms which could possibly drive the two sources. This is presented in **Chapter 4**.

In **Chapter 5**, we move on to the source Swift J1753.5-0127, which remained in the hard state for most of the outburst. This is diametrically opposite to the two sources studied in previous chapters. Prominent QPOs are observed in the PDS and the duration of the outburst is much longer than that observed for the other two sources. Here, we adopt a different approach and try to comment on the accretion geometry using Frequency Resolved Spectroscopy (FRS). We find that the comparison of the QPO and time-averaged spectra hint at the presence of a stable disc even in the low/hard state of the source.

In **Chapter 6**, we present a summary of our results and comment on the future studies based on the obtained results. The recommendations based on this work are listed in **Chapter 7**.

# Contents

# List of Abbreviations

*In order of appearance*

**WD** ...................... White Dwarf

**NS** ...................... Neutron Star

**BH** ...................... Black Hole

**XRB** ................... X-ray Binaries

**HMXB** ................. High Mass X-ray Binary

**LMXB** ................. Low Mass X-ray Binary

**IMXB** ................. Intermediate Mass X-ray Binary

**BHB** .................... Black Hole Binary

**PDS** .................... Power Density Spectrum (or Spectra)

**QPO** ................... Quasi-periodic Oscillation

**LFQPO** ................ Low Frequency Quasi-periodic Oscillation

**HFQPO** ............... High Frequency Quasi-periodic Oscillation

**HWHM** ................ Half Width at Half Maximum

**rms** ..................... root mean square

**HID** .................... Hardness Intensity Diagram

**LHS** .................... Low/Hard State

**BLN** ................... Band Limited Noise

**HIMS** ................. Hard Intermediate State

| | | |
|---|---|---|
| **SIMS** | . . . . . . . . . . . . . . . . . . | Soft Intermediate State |
| **HSS** | . . . . . . . . . . . . . . . . . . | High/Soft State |
| **ISCO** | . . . . . . . . . . . . . . . . . . | Innermost Stable Circular Orbit |
| **ADAF** | . . . . . . . . . . . . . . . . . . | Advection Dominated Accretion Flow |
| **ADIOS** | . . . . . . . . . . . . . . . . | Adiabatic Inflow-Outflow Solution |
| **CDAF** | . . . . . . . . . . . . . . . . . . | Convection Dominated Accretion Flow |
| **LHAF** | . . . . . . . . . . . . . . . . . . | Luminous Hot Accretion Flow |
| **RPM** | . . . . . . . . . . . . . . . . . . | Relativistic Precession Model |
| **TCAF** | . . . . . . . . . . . . . . . . . . | Two-Component Advective Flow |
| **CENBOL** | . . . . . . . . . . . . . . | CENtrifugal pressure supported BOundary Layer |
| **SXT** | . . . . . . . . . . . . . . . . . . | Soft X-ray Transient |
| **RXTE** | . . . . . . . . . . . . . . . . . . | Rossi X-ray Timing Explorer |
| **NICER** | . . . . . . . . . . . . . . . . | Neutron Star Interior Composition Explorer |
| **MAXI** | . . . . . . . . . . . . . . . . . . | Monitor of All-sky X-ray Imaging |
| **FOV** | . . . . . . . . . . . . . . . . . . | Field Of View |
| **SSM** | . . . . . . . . . . . . . . . . . . | Scanning Sky Monitor |
| **SXT** | . . . . . . . . . . . . . . . . . . | Soft X-ray Telescope |
| **LAXPC** | . . . . . . . . . . . . . . . . | Large Area X-ray Proportional Counter |
| **CZTI** | . . . . . . . . . . . . . . . . . . | Cadmium Zinc Telluride Imager |
| **UVIT** | . . . . . . . . . . . . . . . . . . | Ultra-Violet Imaging Telescope |
| **PC** | . . . . . . . . . . . . . . . . . . | Photon Counting |
| **FW** | . . . . . . . . . . . . . . . . . . | Fast Windowed |
| **XTI** | . . . . . . . . . . . . . . . . . . | X-ray Timing |
| **PCA** | . . . . . . . . . . . . . . . . . . | Proportional Counter Array |
| **HEXTE** | . . . . . . . . . . . . . . . . | High Energy X-ray Timing Experiment |

**ASM** . . . . . . . . . . . . . . . . . . . .  All Sky Monitor

**BAT** . . . . . . . . . . . . . . . . . . . .  Burst Alert Telescope

**XRT** . . . . . . . . . . . . . . . . . . . .  X-ray Telescope

**UVOT** . . . . . . . . . . . . . . . . . .  Ultra-Violet and Optical Telescope

**SAA** . . . . . . . . . . . . . . . . . . . .  South Atlantic Anomaly

**GTI** . . . . . . . . . . . . . . . . . . . .  Good Time Interval

**QDP** . . . . . . . . . . . . . . . . . . . .  Quick and Dandy Plotter

**FRS** . . . . . . . . . . . . . . . . . . . .  Frequency Resolved Spectroscopy

**RA** . . . . . . . . . . . . . . . . . . . . .  Right Ascension

**DEC** . . . . . . . . . . . . . . . . . . . .  Declination

**GT** . . . . . . . . . . . . . . . . . . . . .  Guaranteed Time

**ToO** . . . . . . . . . . . . . . . . . . . .  Target of Opportunity

**IMS** . . . . . . . . . . . . . . . . . . . .  InterMediate State

**PSC** . . . . . . . . . . . . . . . . . . . .  Post Shock Corona

**RMF** . . . . . . . . . . . . . . . . . . . .  Redistribution Matrix File

**ARF** . . . . . . . . . . . . . . . . . . . .  Ancillary Response File

**ISSDC** . . . . . . . . . . . . . . . . . .  Indian Space Science Data Centre

**EA** . . . . . . . . . . . . . . . . . . . . .  Event Analysis

**WT** . . . . . . . . . . . . . . . . . . . . .  Windowed Timing

**HR** . . . . . . . . . . . . . . . . . . . . .  Hardness Ratio

**FRED** . . . . . . . . . . . . . . . . . .  Fast Rise and Exponential Decay

**LHXT** . . . . . . . . . . . . . . . . . .  Low Hard X-ray Transient

**XRISM** . . . . . . . . . . . . . . . . .  X-ray Imaging Spectroscopy Mission

**XPoSat** . . . . . . . . . . . . . . . . .  X-ray Polarimeter Satellite

# List of figures

# List of Tables

# Chapter 1

# Introduction

> Sometimes you get to what you thought was the end and you find its a whole new beginning.
>
> —————————————————————
> Anne Tyler, Ladder of Years

Gazing up at the night sky and pondering over the mysteries of the universe has been one of mankind's oldest hobbies. The shiny bright points of light, staring solemnly down towards the Earth, forming numerous beautiful patterns in the sky, have always captivated our interest. Although unsure of the physical processes behind them, cultures all over the world shared equal interest in observing these bright objects, cataloguing them and meticulously charting their paths across the magnificent night sky. In India, the oldest records of sophisticated astronomical data is found in the Rig Veda which dates back to at least 2000 BCE. Things became more interesting when astronomy was expanded to include the whole range of electromagnetic waves, from low energy radio to high energy gamma rays, aided by multiple observatories and instruments, both in space and on the ground. Some stars were found to be sources of highly energetic X-rays, prompting the birth of a new branch of astronomy called X-ray astronomy. Digging into the physical origin of these radiations gave rise to theories suggesting that stars were not the permanent beacons of light that they were assumed to be. Rather, it would seem that the stars in the sky were at different stages in their lives, characterized by the emission of radiation in different wavelengths, each unique to the physical process underlying their origin. In this introductory chapter, we will cover the various stages in the life cycle of a star, with our primary focus on the objects capable of giving rise to high energy. Next, we move on to the radiation processes capable of generating such a huge amount of energy. Following sections deal with specifics and more details on the production of energy when compact objects are

considered. We then narrow down our discussion to the object(s) of interest in this study and finish with a description of the motivation for this work.

## 1.1 Beyond the death of a star

Famous American author Jack Kornfield says in *Buddha's Little Instruction Book*, that "Everything that has a beginning, has an ending". Although the author meant it in a philosophical sense in that context, the statement holds true even in the literal sense. It can also be said of stars - they are born and hence, need to die. A star is born from a gas cloud and passes through about 7 stages[1] before turning into an extremely dense object with strong gravitational pull. These end objects are called compact objects. These are stars in which there is no fuel left to burn and hence cannot rely on thermal pressure against the gravitational pressure. They are White Dwarfs (WD), Neutron Stars (NS) and Black Holes (BH). WD and NS are supported by pressure of degenerate electrons and degenerate neutrons respectively. When a star completely collapses on itself to form a singularity, it becomes a BH. The final stage a star can reach, and the time it takes to do so, is governed by the initial mass of the star. Stars like our sun end up as White Dwarfs, while the more massive stars can turn into Neutron Stars or Black Holes. Compact objects are of a much smaller size when compared to normal stars of similar masses. A 1 $M_\odot$ WD has a radius similar to that of Earth. However, the density of WD lies between $10^7 - 10^9$ kg/m$^3$, which is roughly more than 200,000 times the density of the Earth. A NS has a higher density approximately equal to $10^{17}$ kg/m$^3$ and a radius of the order of tens of kilometres (Shapiro et al., 1976). Compact objects in general, and black holes in particular, are tough to detect directly and hence, indirect methods are relied upon. The super-massive black holes at the centre of a galaxy can be detected only by the motion of objects closer to it. One would assume that the task of identifying compact objects in the night sky is rather tedious and long-winded one. Fortunately, most of the stars seem to be formed in pairs or systems, rather than in isolation. In fact, multiple companions have been proposed for our own sun, with the latest one being HD186302 (Adibekyan, V. et al., 2018). So now, instead of sifting through data related to millions of stars, one could just study the interaction in the star system, either binaries or multiple-star systems, to arrive at the nature of the object. These interactions are more pronounced when one of the objects involved in the system is a compact object. Such systems which consist of a normal star and a compact object are called X-ray binaries (XRBs) - so named (unimaginatively) as they emit mostly in X-rays. XRBs can be classified into two subclasses based on the mass of the companion star, which is also a deciding factor in determining

---

[1] https://imagine.gsfc.nasa.gov/educators/lifecycles/stars.html

the physical processes in play.

Before diving into the different classes of XRBs, it is necessary to provide a short outline of the physical process which gives rise to X-rays. Consider a binary system formed with two stars of varied masses. The more massive star burns up its hydrogen faster and turns into a compact object, while the less massive one continues to be in the main sequence stage. In such a case, the compact object begins to accrete matter from the companion star. The accreted matter possesses angular momentum, courtesy of the rotation of the companion star, and hence cannot fall into the compact object directly. This infall flattens into a disc in a direction perpendicular to the compact object's rotation axis. This is called an accretion disc. As the accreted material falls or spirals inwards, gravitational potential energy is converted into radiation released as X-rays. For the matter to fall into the accretor, it needs to lose its angular momentum. This is achieved due to viscosity and turbulence. X-rays can be generated by other means as well. However, our primary focus will be the emission of X-rays by accretion process. In the following sections, we define different types of XRBs and their accretion process.

### 1.1.1 High Mass X-ray Binaries

XRBs in which the mass of the companion star is $\geq 10$ M$_\odot$ are typically classified as High Mass XRBs (HMXBs). The companion is generally an O or B type star whose optical/UV luminosity is likely to be dominant (Conti, 1978; Petterson, 1978). Matter is ejected from the OB companion star through stellar winds, which can then be captured by the black hole in a sufficiently closer orbit, enough to power the X-ray source. Figure 1.1 shows the schematic diagram of a HMXB in the left panel. The accretion occurs via capture of the ejected stellar wind material by the compact object. This happens through spherical accretion or Bondi-Hoyle accretion (Bondi and Hoyle, 1944). The critical gravitational potential lobe around the system is also shown. Supplementary mass accretion can also occur by transfer of mass via the inner Lagrangian point. The difference in the mode of energy supply is discernible in the luminosity emitted by the source. A constant X-ray radiation, with luminosity in the range $10^{35} - 10^{37}$ erg s$^{-1}$, is observed when the accretion is through stellar wind, whereas, accretion via Roche Lobe overflow can generate a luminosity $> 10^{38}$ erg s$^{-1}$ (Lewin and Livingston, 1995). HMXBs are mostly clustered in the spiral arms of our Galaxy. Cyg X-1 is a well-known example of a HMXB. The X-ray luminosity of Cyg X-1 is $(2-5.5) \times 10^{37}$ erg s$^{-1}$ (Sunyaev and Truemper, 1979; Meyer-Hofmeister et al., 2020, etc).
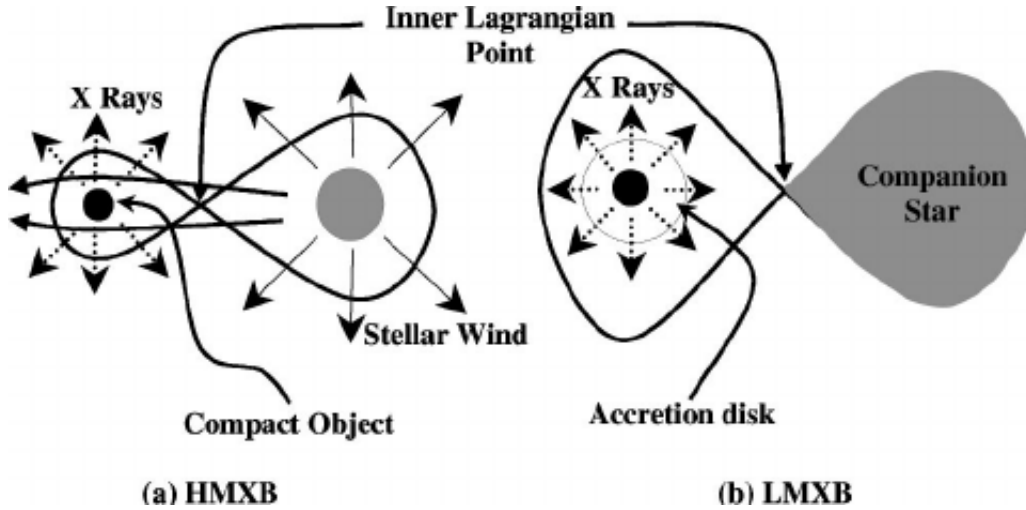
**Figure 1.1:** Schematic diagram of HMXB and LMXB systems is shown in a and b panels of the figure respectively. The inner Lagrangian point is shown in both cases through which mass is transferred. In HMXBs, mass is also transferred through stellar winds. *Image courtesy : Moret et al. (2003).*

### 1.1.2 Low Mass X-ray Binaries

If the mass of the companion star is close to the solar mass, we call it a Low Mass XRB (LMXB). The companion star is type A or later and even white dwarfs in some evolved cases. The X-rays from the system and the companion star dominates the optical light and hence, they appear as faint blue stars (Bradt and McClintock, 1983, and references therein). The stellar wind is not strong enough to power the X-ray radiation. As seen from panel (b) of Figure 1.1, mass transfer occurs only through Roche lobe overflow. The Roche lobe radius is a function of the orbital separation and masses of the two stars. Mass transfer is triggered when the envelope of the companion star expands and fills its Roche lobe or when the binary separation between the two objects shrinks due to angular momentum losses. This matter forms an accretion disc around the compact object, as mentioned earlier, due to conservation of angular momentum. The heating of the accretion disc gives out X-ray radiation. The population of LMXBs is mostly concentrated in the Galactic bulge. LMXBs, specifically those with a black hole as compact object, form the focus of our studies and so their various properties will be discussed in detail later on. GRS 1915+105 is a very well-known member of this class (Castro-Tirado et al., 1996).

### 1.1.3 Intermediate Mass X-ray Binaries

The above classification only accounts for those systems, whose companion stars have masses less than $1.5 M_\odot$ or greater than 10 $M_\odot$. Astronomers have been

puzzled for years about the population of stars lying between these two ranges. These are termed as Intermediate mass XRB (IMXB). However, recent studies have shown that IMXBs are just LMXBs in earlier stages of evolution. It is possible that the companion in the IMXB transferred most of its mass and evolved into an LMXB (King and Ritter, 1999; Podsiadlowski and Rappaport, 2000; Kolb et al., 2000). Hence, they are generally studied together with LMXBs.

In this work, we focus only on a few LMXBs. Specifically, we focus on those which contain a black hole. These are called Black Hole Binaries (BHB). Before moving onto their nature and evolution, it is necessary to brush up on a few fundamentals of radiation processes which occur in space. In the next section, we talk about different types of radiation and the processes which give rise to them. This topic is exceptionally vast and has huge tomes dedicated to it in itself (Rybicki and Lightman, 1986; Knoll, 1989, etc.). Here, we will merely summarize the basics and focus primarily on those which we are likely to encounter in the study of LMXBs.

## 1.2 A brief introduction to Radiation processes

Any discussion on X-ray binaries and accretion is incomplete without the inclusion of terms like thermal and non-thermal radiation, the state of the matter involved, and the effect of the interaction of radiation with matter. Basically, we need to equip ourselves with the knowledge of how a particular interaction between matter and radiation is likely to effect the visible entities i.e, intensity, spectrum and so on. To do so, the starting point is always the radiative transfer equation given by,

$$\frac{\mathrm{d}I_\nu}{\mathrm{d}s} = -\alpha_\nu I_\nu + j_\nu \tag{1.1}$$

where $\frac{\mathrm{d}I_\nu}{\mathrm{d}s}$ gives the variation of specific intensity ($I_\nu$) along a ray, ds is a differential element along the length of the ray, $\alpha_\nu$ and $j_\nu$ are coefficients related to absorption and emission respectively. The intensity in an emitting and absorbing medium can be obtained by solving equation 1.1. As we navigate across different physical processes, we only need to find the physical forms of these coefficients corresponding to each of them.

Another useful way of writing the equation is obtained if we consider $\tau_\nu$ instead of s, where $\tau_\nu$ is the optical depth. This is measured along the path of the travelling ray. It is defined as:

$$\mathrm{d}\tau_\nu = \alpha_\nu \,\mathrm{d}s \tag{1.2}$$

$$\tau_\nu(s) = \int_{s_0}^{s} \alpha_\nu(s') \,\mathrm{d}s' \tag{1.3}$$

A medium is optically thick or opaque when $\tau_\nu > 1$ and optically thin or transparent if $\tau_\nu < 1$. This quantifies the interaction a photon has while traversing a medium. Therefore, the transfer equation can now be written as,

$$\frac{dI_\nu}{d\tau_\nu} = -I_\nu + S_\nu \tag{1.4}$$

where $S_\nu$ is the source function defined as ratio of emission to absorption coefficient.

Below, we discuss a few of the emission processes in detail.

### 1.2.1   Black Body Radiation

Black body radiation is emitted when all the photons are in thermal equilibrium with each other. Photons can be treated as perfect Bose-Einstein gas as the interactions between them are negligible. Also, they travel with the speed of light and therefore have zero rest mass. The law for intensity of radiation emitted at different frequencies $\nu$, was first derived by Planck. This also marks the first appearance of the Planck constant h, in thermal radiation. The intensity of radiation is given by,

$$I_\nu = B_\nu(T) = \frac{2h\nu^3/c^2}{\exp(h\nu/kT) - 1} \tag{1.5}$$

Equation 1.5 expresses the *Planck law*. The derivation for the same is presented in Rybicki and Lightman (1986) (Section 1.5), which we do not reproduce here. At lower frequencies, equation 1.5 reduces to the *Rayleigh-Jeans law* and applies in the radio region in the electromagnetic spectrum. At larger frequencies ($h\nu >> kT$), we obtain the *Wien law*. This states that the brightness of the blackbody decreases rapidly with frequency when the maximum is reached. The peak frequency of the blackbody law shifts linearly with temperature and is represented as,

$$\lambda_{\max}T = 0.290 \text{ cm deg} \tag{1.6}$$

called *Wien displacement law*. Another important result that can be derived from equation 1.5 is the Stefan-Boltzmann law, which gives the energy flux (F) leaving the surface of the body as

$$F = \sigma T^4 \tag{1.7}$$

where F is in units of erg cm$^{-2}$ s$^{-1}$ and $\sigma$ is the Stefan-Boltzmann constant. This implies that the thermal radiation from the surface of an opaque body rises very quickly with temperature. It is clear from the above that all bodies, irrespective of their composition, emit the same continuum, provided that they are at the same temperature. Hence, the continuum radiation of a star can only provide information about the temperature of the surface and not details of the composition. This can be done only by looking at lines in the spectrum.

Another term that needs to be introduced in this context is the *effective temperature ($T_{\text{eff}}$)*. Total amount of flux, integrated over all frequencies, radiated at a source is obtained. This is equated to the flux of the blackbody at temperature $T_{\text{eff}}$.

$$F = \int \cos\theta\, I_\nu\, d\nu\, d\Omega = \sigma T_{\text{eff}}^4 \tag{1.8}$$

In XRBs, and black holes in particular, the source of continuum radiation is the accretion disc. This can effectively be defined as blackbody radiation emitted from different radii of the thermal disc. The flux produced by an accretion disc at a certain inclination is derived in Mitsuda et al. (1984); Makishima et al. (1986) and the local temperature at a radius r is derived as,

$$T(r) = \left(\frac{3GM\dot{M}}{8\pi\sigma r^3}\right)^4 \tag{1.9}$$

where G is the gravitational constant and $\dot{M}$ is the mass accretion rate.

### 1.2.2 Bremsstrahlung

Bremsstrahlung, which originates from the German words *bremsen* and *Strahlung* meaning 'to brake' and 'radiation' respectively, quite literally means 'braking radiation' i.e., radiation emitted due to deceleration of a charged particle in the Coulomb field of another charge. This is also termed as a *free-free* emission as radiation is generated by particles which are free before and after the emission of a photon. Bremsstrahlung due to collision of like particles like electron-electron and proton-proton is not considered, as the dipole moment, proportional to the centre of mass, is simply a constant of motion. Therefore, two different particles need to be considered. In electron-ion bremsstrahlung, electrons are considered as primary radiators since ions are comparatively more massive.

In X-ray astronomy, we deal with temperatures above $10^5$ K, where the plasma is likely to be ionized. In such cases, an electron travelling through plasma is accelerated. As the acceleration is non-uniform, it emits photons with a range of wavelengths i.e., continuum spectra.

We assume that the electron moves rapidly such that the deviation from its path in a straight line is negligible. This is called the small-angle scattering regime. In this regime, we first obtain the emission from a single collision. This can be extended to find the total spectrum for a medium with ion density $n_i$, electron density $n_e$ and for a fixed electron speed v. The total emission per unit time per unit volume per unit frequency range is then,

$$\frac{dW}{d\omega\, dV\, dt} = n_e n_i 2\pi v \int_{b_{\text{min}}}^{\infty} \frac{dW(b)}{d\omega}\, b\, db \tag{1.10}$$

where $b_{min}$ is some minimum value of impact parameter. The value of $b_{min}$ can be estimated in two cases. The first is when the straight line approximation becomes invalid and the second is when the quantum nature is considered and uncertainty principle plays an important role. In either case, equation 1.10 can be written as,

$$\frac{dW}{d\omega \, dV \, dt} = \frac{16\pi e^6}{3\sqrt{3} \, c^3 m^2 v} n_e n_i Z^2 g_{ff}(v, \omega) \tag{1.11}$$

where $g_{ff}$ is the Gaunt factor which is a function of energy of electron and frequency of emission.

When matter in thermal equilibrium is considered, one needs to apply the above equation to the thermal bremsstrahlung case. This is obtained by averaging the single-speed expression obtained in equation 1.11 over a thermal distribution of speeds. This gives,

$$\frac{dW}{dV dt d\nu} = \frac{2^5 \pi e^6}{3mc^3} \left( \frac{2\pi}{3km} \right)^{1/2} T^{-1/2} Z^2 n_e n_i e^{-h\nu/kT} \bar{g}_{ff} \tag{1.12}$$

Therefore, in CGS units, the emission is obtained as,

$$\epsilon_\nu^{ff} \equiv \frac{dW}{dV dt d\nu} = \text{constant} \times Z^2 n_e n_i T^{-1/2} e^{-h\nu/kT} \bar{g}_{ff} \tag{1.13}$$

$\bar{g}_{ff}$ is the velocity averaged Gaunt factor. The factor $e^{-h\nu/kT}$ comes from the lower-limit cutoff in the velocity integration due to photon discreteness (i.e., photon cannot be created below a certain value of velocity) and Maxwellian shape of velocity distribution. The equations 1.12 and 1.13 also show that bremsstrahlung gives a flat spectrum in a log-log plot upto the cutoff of $h\nu \sim kT$ only for optically thin sources. Similar to the above process, to obtain formulae for non-thermal bremsstrahlung, the actual distribution of velocities needs to be known and equation 1.11 must be averaged over that distribution. In optically thick medium, the spectrum is constrained to be not more effective than a black body spectrum. This is thermal bremsstrahlung self-absorption. The spectrum turns over at low frequency with a power-law dependence identical to the drop-off in intensity at low frequency seen in the Rayleigh-Jeans part of the blackbody spectrum. Galaxy clusters are a prominent source of X-ray Bremsstrahlung radiation.

### 1.2.3 Synchrotron radiation

Synchrotron radiation, also known as *magneto-bremsstrahlung* radiation, is the emission of relativistic electrons gyrating in a magnetic field. Radio emission from the Galaxy, supernova remnants and extragalactic radio sources can be attributed to this process. It is also responsible for non-thermal optical and X-ray emission

from Crab nebula and continuum emission of quasars. The usage of the term 'non-thermal' is one that will be encountered multiple times in the discussion on high energy astrophysics. However, it could be a misnomer, as the origin of all processes is 'thermal' in some sense. It is generally meant to convey that the continuum emission cannot be described by black body radiation or thermal bremsstrahlung i.e., the velocity distribution of the particles involved is not Maxwellian.

For non-relativistic electrons, the radiation is known as *cyclotron radiation* and is at the gyration frequency $\omega = eB/m_e c$. It becomes synchrotron radiation, when relativistic particles are considered, as mentioned above.

Consider a particle of charge q and mass m, moving in a magnetic field $\bar{B}$. Larmor's formula can be extended to relativistic particles to obtain the total power in rest frame. We then find the components of acceleration in direction parallel and perpendicular to the velocity and obtain the following formula,

$$P = \frac{4}{3}\sigma_T c \beta^2 \gamma^2 U_B \tag{1.14}$$

where $\sigma_T = 8\pi_0^2/3$ is Thomson cross section and $U_B$ is the magnetic energy density $B^2/8\pi$. In case of relativistic particles, radiation is beamed in the direction of motion of the particle. Therefore, before calculating the synchrotron spectrum, we need to consider the beaming effects. The observer sees a pulse of radiation emitted in a smaller time interval than the gyration period. The spectrum will thus be spread over a broader region than of the order of $\omega_B/2\pi$. As Longair himself puts it in Longair (2011), "I am not aware of any particularly simple way of deriving [synchrotron spectrum]", we will not go into the details of the derivation. The derivations are available in Longair (2011); Rybicki and Lightman (1986). Here we just summarize the steps as done in Longair (2011). First, we obtain the energy emitted per unit bandwidth for an arbitrarily moving electron, then select a suitable set of coordinates to compute the field components radiated by the electron spiralling in a magnetic field and finally work out the algebra to obtain the spectral distribution of field components. The power per unit frequency emitted by each electron is given by,

$$P(\omega) = \frac{\sqrt{3}}{2\pi}\frac{q^3 B \sin\alpha}{mc^2}F\left(\frac{\omega}{\omega_c}\right) \tag{1.15}$$

where $\alpha$ is the angle between the field and the velocity called *pitch angle*, F is a dimensionless function and $\omega_c$ is the critical frequency $\omega = \frac{3}{2}\gamma^3\omega_B\sin\alpha$ to which the spectrum extends before falling away.

Often the electrons emitting the synchrotron radiation have a power-law distribution of energies, i.e., $N(E)dE \propto E^{-p}\,dE$ or $N(\gamma)d\gamma \propto \gamma^{-p}\,d\gamma$. Then the spectrum is given by an integral over the electron energy distribution,

$$P(\omega) \propto \int d\gamma\,\gamma^{-p}F\left(\frac{\omega}{\omega_c}\right) \tag{1.16}$$

Changing the variable from $\gamma$ to $x \equiv \frac{\omega}{\omega_c}$, the integral becomes a dimensionless integral over x. We find,

$$P(\omega) \propto \omega^{-(p-1)/2} \tag{1.17}$$

One of the distinguishing features of synchrotron radiation is that it is strongly polarized. For particles with powerlaw distribution of energies, the degree of polarization is given by,

$$\Pi = \frac{p+1}{p+\frac{7}{3}} \tag{1.18}$$

This is used to map out the the magnetic fields of spiral galaxies. Synchrotron emission has also been used to explain the spectra from X-ray binaries like Cygnus X-1 and GX 339-4 (Wardziński et al., 2002; Malzac, 2012).

### 1.2.4 Compton and Inverse Compton scattering

Scattering is a common emission process which depends entirely on the amount of radiation falling on the medium. *Electron scattering* is the most important mechanism of this type. Compton scattering causes the exchange of momentum between a photon and a charged particle. For low energy photons, $h\nu << mc^2$, scattering of radiation from free charged particles reduces to Thomson scattering. However, here as we deal with high energy photons, Compton and inverse Compton scattering play an extremely important role. For Thomson scattering, the energy of the incident and scattered photon are equal and the Thomson cross-section is given by $\sigma_T = \frac{8\pi}{3}r_0^2$, where $r_0$ is the classical electron radius. This is when the scattering is elastic or coherent.

When quantum effects are taken into consideration, kinematic effects also should be taken into account, as the photon now possesses a momentum of $h\nu/c$ along with energy $h\nu$. The scattering cannot be considered elastic due to the recoil of the charge. Using the expressions for conservation of momentum and energy, we obtain the energy of the scattered photon ($\varepsilon_l$) as,

$$\varepsilon_l = \frac{\varepsilon}{1 + \frac{\varepsilon}{mc^2}(1 - \cos\theta)} \tag{1.19}$$

which in terms of wavelength is given by,

$$\lambda_l - \lambda = \lambda_c(1 - \cos\theta) \tag{1.20}$$

where $\lambda_c$, the Compton wavelength, is defined as $\lambda_c = h/mc$. For $\lambda >> \lambda_c$, the scattering is approximately elastic and there is no change in photon energy.

The differential cross-section for unpolarized radiation is given by Klein-Nishina formula as,

$$\frac{d\sigma}{d\Omega} = \frac{r_0^2}{2}\frac{\varepsilon_l^2}{\varepsilon}\left(\frac{\varepsilon}{\varepsilon_l} + \frac{\varepsilon_l}{\varepsilon} - \sin^2\theta\right) \tag{1.21}$$

Therefore, the cross-section reduces from the classical value as the photon energy becomes large. The total cross-section can be given as,

$$\sigma = \sigma_{\mathrm{T}}\frac{3}{4}\left[\frac{1+x}{x^3}\left(\frac{2x(1+x)}{1+2x} - \ln(1+2x)\right) + \frac{1}{2x}\ln(1+2x) - \frac{1+3x}{(1+2x)^2}\right] \quad (1.22)$$

where $x \equiv h\nu/mc^2$. In the non-relativistic regime, it reduces to

$$\sigma \approx \sigma_{\mathrm{T}}\left(1 - 2x + ...\right), \quad x << 1 \quad \text{(Thomson)} \quad (1.23a)$$

$$\sigma = \frac{3}{8}\sigma_{\mathrm{T}}x^{-1}\left(\ln 2x + \frac{1}{2}\right), \quad x >> 1 \quad \text{(Extreme KN)} \quad (1.23b)$$

When the moving electron has sufficient kinetic energy compared to the photon, the net energy may be transferred from the electron to the photon. This is called *inverse Compton scattering.* Before moving on to the mathematical aspects of the process, let us first place it in an astrophysical context. If a plasma is embedded in a radiation field of temperature $T_{\mathrm{rad}}$, the energy between photons and electrons is continuously transferred via scattering. If the temperature of the electrons, $T_e$, is greater than $T_{\mathrm{rad}}$, the electrons cool by transferring energy to the photons through inverse Compton scattering. In the alternate scenario, wherein $T_e << T_{\mathrm{rad}}$, the photons cool down by Compton scattering. In astrophysical phenomena, we mainly deal with inverse Compton scattering, which is the mechanism for the origin of high energy photons. We also encounter a term called *Comptonisation* in this context, which will be used frequently throughout this work. Comptonisation refers to multiple Compton scatterings by thermal electrons which results in the distortion of the energy spectrum.

The complete mathematical treatment for obtaining the spectrum for Comptonisation is detailed in Rybicki and Lightman (1986). One needs to first obtain the evolution of the photon phase space density due to scattering from multiple electrons using Boltzmann equation. For simplicity, we consider the case where electrons are non-relativistic, wherein the Boltzmann equation can be approximated to the Fokker-Planck equation. The Fokker-Planck equation for photons scattering off a non-relativistic, thermal distribution of electrons was first derived by Kompaneets (1957) and is known as Kompaneets equation. This is given by,

$$\frac{\partial n}{\partial t_c} = \left(\frac{kT}{mc^2}\right)\frac{1}{x^2}\frac{\partial}{\partial x}[x^4(n' + n + n^2)] \quad (1.24)$$

where $t_c \equiv (n_e\sigma_{\mathrm{T}}c)t$ is the time measured in units of mean time between scatterings and n is the photon phase space density. Detailed analysis of the Compton spectra requires a solution of equation 1.24.The condition at which the scattering

process affects the total photon energy is obtained using the Compton y parameter, which is defined as,

$$y \equiv \left(\text{average fractional energy change per scattering}\right) \times \left(\text{mean number of scatterings}\right) \tag{1.25}$$

In general, when $y \geq 1$, the total photon energy and spectrum will be altered, whereas the total energy remains almost same when $y << 1$. Approximate analysis for both cases i.e., modified black body ($y << 1$) and saturated Comptonisation ($y >> 1$) are sufficient. However, a detailed treatment with equation 1.24 is required for intermediate cases (i.e., unsaturated Comptonisation). In the present studies, we have used Comptonisation models where a soft photon input is considered. This particular case corresponds to the media where inverse Comptonisation is important, but not saturated to the Wien spectrum for most photons ($y \sim 1$). Considering a steady-state solution, equation 1.24 can be modified as,

$$0 = \left(\frac{kT}{mc^2}\right) \frac{1}{x^2} \frac{\partial}{\partial x}[x^4(n' + n)] + Q(x) - \frac{n}{\text{Max}(\tau_{es}, \tau_{es}^2)} \tag{1.26}$$

Here, $Q(x)$ is the photon source. Also, since photons scatter multiple times, it can be approximated that the the probability for a photon to escape per Compton scattering time is equal to the inverse of the mean number of scatterings, $\text{Max}(\tau_{es}, \tau_{es}^2)$. Assume that $Q(x)$ is non zero only for $x < x_s$, where $x_s << 1$ as the source seed photons are 'soft'. For $x >> 1$, an approximate solution is $n \propto e^{-x}$, that is, the spectrum falls off exponentially at photon energies much above the electron temperature. On the other hand for $x_s << x << 1$, we get the power-law solution $n \propto x^m$, where,

$$m = -\frac{3}{2} \pm \sqrt{\frac{9}{4} + \frac{4}{y}} \tag{1.27}$$

Here, $y$ is the Compton y-parameter, given by $y = \frac{4kT}{mc^2}\text{Max}(\tau_{es}, \tau_{es}^2)$ for non-relativistic thermal distribution of electrons. A high-energy cutoff is incorporated in the models of Comptonisation used for the present analysis related to the temperature of the thermal electrons in an optically thin medium close to the compact object (see for eg., Belloni et al., 2006). Current models incorporate the presence of a 'hybrid' plasma, which contains both thermal and non-thermal components. The optical depth of thermal electrons is 1, while those of non-thermal electrons is $<< 1$ (Ghisellini et al., 1993).

### 1.2.5 Fluorescence

Another phenomenon that needs to be introduced is *fluorescence*. Originally coined by Sir George Stokes to explain the observation of anomalous colours under

different illuminations, fluorescence means the emission of light by a substance that has absorbed electromagnetic radiation. When an X-ray photon interacts with matter, the energy is transferred completely to a bound electron in the inner shell. The electron is knocked out, creating a vacancy. This results in an electron jumping from a higher orbit to fill its place, giving out an X-ray with energy corresponding to the difference in energy between the two bound shells. On an X-ray spectrum, these emission lines appear as sharp peaks. However, the line shape is also determined by multiple physical effects like Doppler broadening and Natural broadening.

In dealing with X-ray binaries, we observe that the line profile mostly observed is the Fe $K_\alpha$ line, which forms when an electron in the L shell (n = 2) drops into the vacancy in the K-shell (n = 1). This line is observed at 6.4 keV. The line emission observed, apart from being a signature of reflection from the disc, can also be used to comment on the spin of the compact object, based on its broadening and skewness (Reynolds, 2014). Most of the time, the profile observed is a combination of both Doppler and Lorentz profiles. The centre is dominated by the Doppler profile, while the 'wings' are dominated by Lorentz profile.

## 1.3 Accretion - tapping into the power source

Accretion, as a power source, made sense only after it was realized that gravity is the only source strong enough to power many luminous objects. For a body of mass M and radius R, the gravitational potential energy released by the accretion of mass m onto its surface is,

$$\Delta E_{acc} = GMm/R \tag{1.28}$$

where G is the gravitation constant. The more compact the object, the greater is the energy generated. The efficiency depends on the parameter called *compactness* defined as M/R. Therefore, accretion as a mechanism, is more efficient for neutron stars (R $\sim$ 10 km) and black holes (R = $2GM/c^2$). At constant compactness, luminosity of an accreting object system depends on the accretion rate ($\dot{M}$). The maximum luminosity an object can emit is called its *Eddington luminosity*. This happens when the outward pressure of radiation just about balances the gravitational attraction when the accretion flow is steady and spherically symmetric. The expression for *Eddington Luminosity* is given by,

$$L = 4\pi GMm_p c/\sigma_T = 1.3 \times 10^{38} \text{ erg s}^{-1} \tag{1.29}$$

and accretion luminosity is given by L = $GM\dot{M}/R$. In case of a black hole, the radius does not refer to a surface, but only to a region close to the horizon of no

escape. The uncertainty is parametrized by a dimensionless quantity η, which is the efficiency.

$$L_{acc} = 2\eta GM\dot{M}/R = \eta\dot{M}c^2 \tag{1.30}$$

where $R = 2GM/c^2$ is called the *Schwarzschild radius*. η can lie between 0 and 1. We have already mentioned in Section 1.1 that accreted material cannot fall directly on the compact object due to angular momentum conservation. This leads to the formation of accretion discs, where gravitational potential energy is extracted and converted into radiation. We have also briefly touched upon the two mechanisms of accretion i.e. Roche lobe overflow and wind accretion, seen mostly in LMXBs and HMXBs respectively. A schematic representation of the same is presented in Figure 1.1. We discuss these processes in detail in the following sections.

### 1.3.1 Stellar Wind Accretion

In binary systems where the companion stars are O or B type stars (i.e., HMXBs), it so happens, that the star ejects material out during a certain stage in its evolution. This matter is accreted onto the compact object through the stellar winds. Wind accretion is one of the most popular applications of the *Bondi-Hoyle-Lyttleton* analysis. The stellar winds have mass loss rates ($\dot{M}$) of $10^{-6}-10^{-5}$ $M_\odot$ yr$^{-1}$ and they are highly supersonic. The wind particles that flow close to the compact object, such that their kinetic energy is less than the gravitational potential energy, are accreted in a cylindrical region with radius,

$$r_{acc} \sim 2GM/v_{rel}^2 \tag{1.31}$$

where $v_{rel}$ is the relative velocity of the wind. The fraction of stellar wind captured by the compact object is given by comparing the mass flux into the accretion cylinder of radius $r_{acc}$ with the total mass loss rate $-\dot{M}_w$ of the star as,

$$\frac{\dot{M}}{-\dot{M}_w} = \frac{1}{4}\left(\frac{M}{M_c}\right)^2\left(\frac{R_c}{a}\right)^2 \tag{1.32}$$

where $M_c$ and $R_c$ are mass and radius of the normal companion star. For typical parameters of X-ray binaries, the accretion rate comes out to be $10^{-4} - 10^{-3}$ of the mass-loss rate $-\dot{M}_w$. This seems to be too small for the accreting system to be luminous enough to be detected. However, the mass loss rates of the stars are themselves high enough to make the sources observable. There is still some difficulty in reconciling the theory with the observations when it comes to stellar winds. For instance, the flow pattern assumed by Bondi-Hoyle-Lyttleton significantly differs when the orbital velocity is comparable to the wind speed (Theuns and Jorissen, 1993). In the present studies, we focus only on LMXBs, which follow the more efficient and significantly well-studied accretion process of Roche Lobe Overflow.

### 1.3.2  Roche Lobe Overflow

In the Roche approach, we consider the orbit of a test particle in the gravitational potential of two massive bodies orbiting each other. Two primary assumptions considered in astronomy are that

1. the test particle does not perturb the orbits of these bodies as they are massive and

2. the orbits are circular and the masses can be considered as point masses.

The stars then execute Kepler orbits about each other in a plane. A schematic representation is shown the right panel of Figure 1.1. We consider a binary system with masses $M_1 = m_1 M_\odot$ and $M_2 = m_2 M_\odot$. Then, following Keplers laws, we have,

$$4\pi^2 a^3 = GMP^2 \tag{1.33}$$

where a is the binary separation and is a function of the mass ratio $q = M_2/M_1$ and $P^{2/3}$. The angular velocity of the binary $\omega$ is given as,

$$\omega = \left[\frac{GM}{a^3}\right]^{1/2} \tag{1.34}$$

Using Euler equation and accounting for the centrifugal and coriolis force, the Roche potential is obtained as,

$$\phi_R(r) = -\frac{GM_1}{|\mathbf{r} - \mathbf{r_1}|} - \frac{GM_2}{|\mathbf{r} - \mathbf{r_2}|} - \frac{1}{2}(\omega \times \mathbf{r})^2 \tag{1.35}$$

where $\mathbf{r_1}$ and $\mathbf{r_2}$ are position vectors of the centres of the two stars and $\phi_R$ is the set of equipotential surfaces. A particular equipotential surface intersects itself at the inner Lagrangian point $L_1$, which acts as a saddle between the two valleys representing the two bodies. The region bound by this surface is called a Roche Lobe. Mass transfer is therefore easier through this pass $L_1$. Initially, we consider the stars in the binary to be smaller than their respective Roche lobes. Suppose that one of the stars swells up during its evolutionary track such that the surface of the star lies on its Roche lobe and matter is close to $L_1$. A small perturbation of the material will then push matter through $L_1$ to the other star. The star from which matter is transferred is referred to as *secondary* and the one onto which matter is accreted is called *primary*. This is the accretion process followed mostly in LMXBs.

### 1.4 Outbursts - Where and How?

So far we have

- familiarized ourselves with different radiation processes likely to occur in systems containing black holes

- studied accretion as a source of power generated in BHBs through stellar wind and Roche lobe Overflow.

In the following sections, we use the above concepts and try to interweave them neatly into the story of outbursts. However, any introductory chapter on study of X-ray sources would be incomplete without the mention of Sco X-1, the first extra-solar X-ray source to be discovered (Giacconi et al., 1962). On 18 June 1962, Riccardo Giacconi and team, launched a small X-ray detector aboard an Aerobee rocket. Sco X-1 owns the distinction of being the only point source to be detected in X-rays in the mere 350 seconds that the rocket remained above Earth's atmosphere. This event, almost as significant as the discovery of moons around Jupiter by Galileo, encouraged astronomers to launch a flurry of X-ray detectors aboard balloons, rockets and satellites. Thanks to this much needed shot in the arm for X-ray astronomy, extra-solar X-ray observations increased significantly, which in turn facilitated the discovery of X-ray outbursts. Outbursts, as the name suggests, is a sudden flare-up in intensity. Some sources show an increase in brightness for a short duration and then fade into the darkness, only to repeat the cycle after some time. These sources are called **Transients**. This phenomena was observed only when rocket flights could be used on a regular basis to view the X-ray sky. A source was detected at a location in May 1967, which wasn't seen earlier in 1965. When it disappeared again in September 1967, the first transient X-ray source - Cen X-2, had been identified (Harries et al., 1967; Chodil et al., 1968). Cen X-4 was discovered soon afterwards in 1969 (Evans et al., 1970). Within a span of 5 years, many such sources were reported, prompting the emergence of a new class called *X-ray transients*. Hundreds of such X-ray transients are now known belonging to different categories. In Figure 1.2, we show lightcurves of three transient sources GRS 1915+105, GX 339-4 and 4U 1630-472 obtained using *Monitor of All-Sky X-ray Imaging (MAXI)* in the $2-20$ keV range. These three lightcurves are just an example to show the range of the variability seen in XRBs. GRS 1915+105 was referred to as a quasi-persistent source for more than 2 decades as it was always in outburst, until it went inexplicably quiet in mid-2018 (see Belloni et al., 2000; Klein-Wolt et al., 2002; Negoro et al., 2019; Athulya et al., 2022). GX 339-4 is a BHB that goes into regular outbursts once in approximately $2-3$ years (Tetarenko et al., 2016). 4U 1630-472 is a unique source that shows two different types of outbursts - one lasting for almost two years and the other for around 100-150 days (Abe et al., 2005; Capitanio et al., 2015; Baby et al.,
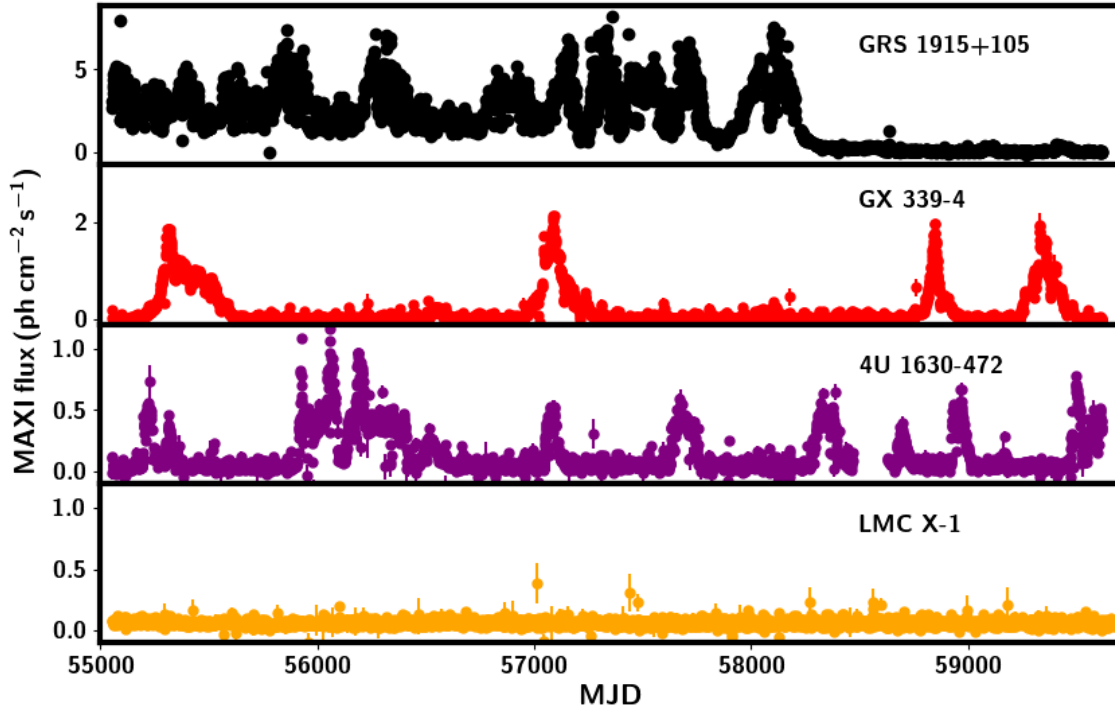
**Figure 1.2:** *MAXI* lightcurves of three transient sources from MJD 55000 to 59710. Its spans a duration of 13 years, from mid 2009 to 2022. The lightcurves of GRS 1915+105, GX 339-4 and 4U 1630-472 are shown in the top, middle and bottom panels respectively in the energy range $2 - 20$ keV. GRS 1915+105 remained active till around MJD 58300 and then went into quiescence. GX 339-4 is known to undergo outbursts approximately once every few years. These outbursts last from anywhere between 200 and 400 days. The third panel shows the lightcurve of 4U 1630-472. It undergoes two different types of outbursts spaced approximately 600 days and 2 years respectively. Details will be discussed in Chapter 3. The last panel shows the lightcurve of the persistent source LMC X-1 for comparison. The lightcurve remains more or less stable although variations in intensity are occasionally reported.

2020). We will be introduced to this source in much more detail in Chapter 3. The lightcurve of the persistent source LMC X-1 (Mark et al., 1969) is also shown in the fourth panel for comparison. An interesting point about the sources is not just the duration of the outbursts or their periodicity, but also their brightness. It is clear from Figure 1.2 that of the 3 sources shown here, GRS 1915+105 is the brightest at the peak of the outbursts, followed by GX 339-4 and 4U 1630-472, in that order. Different sources exhibit multiple outbursts varying in intensity, recurrence time and duration. In spite of all these differences, it is important to note that the physical mechanisms underlying these outbursts can be encompassed by a

few simple theories. In the following sections, we look at the standard accretion disc and the instabilities which could trigger these outbursts. We then proceed to follow the outburst as it passes through various states, introducing other alternate theories and modifications to the standard disc theory, incorporated to explain the observations in each case.

### 1.4.1 Steady state Accretion disc

The structure of accretion flow is basically governed by the heating or cooling processes assumed to be important while balancing against gravitational heating. Shakura and Sunyaev, in 1973, assumed that viscous stresses convert gravitational potential energy to heat, which is then radiated locally at a given radius (Shakura and Sunyaev, 1973). At a given radius of $r = R/R_g$ ($R_g$ is gravitational radius $GM/c^2$), the disc emits at the temperature of $T(r) \propto r^{-3/4}$. The resulting spectrum is given by a combination of blackbody spectra. This implies that more luminosity is generated at smaller radii as the gravity is stronger. So the temperature increases inwards. This solution is consistent with a geometrically thin disc and only breaks down at luminosities close to Eddington luminosity. This implies that the spectrum is more or less independent of the details of the viscosity mechanism. Therefore, disc spectra can be predicted using phenomenological descriptions of stresses like the Shakura-Sunyaev (SS) $\alpha$ prescription, in which shear stresses are directly proportional to total pressure i.e., $t_{r\phi} = \alpha P_{tot}$. Magneto-rotational instability has been proposed as one of the candidates for the physical origin of the stress (see Balbus, 2005). However, the details related to it need not be delved into for our current discussion. What needs to be addressed however, is that the SS solution assumes that mass accretion rate is constant with radius, which may not be true in some cases. There are two major instabilities which are seen in SS discs - one related to hydrogen ionization, seen at lower luminosities and the other due to radiation pressure which occurs at higher luminosities.

### 1.4.2 Hydrogen Ionization instability

Ionization instability was first used to explain the lightcurve profiles in dwarf novae in Meyer and Meyer-Hofmeister (1984). This same mechanism could be linked to X-ray novae (Lasota, 2001). Initially, the accretion disc is cool and faint and the hydrogen is mostly neutral. At low accretion rates, the standard SS disc is thermally and viscously unstable for a narrow range of temperature ($10^{4-5}$ K) associated with hydrogen ionization. The instability occurs due to the high sensitivity of opacity to the plasma temperature. As a result, a small increase in temperature produces huge increase in opacity as the high energy photons ionize some of the hydrogen in the disc. The energy of these photons stays in the disc, thus increasing its temperature. This results in more hydrogen

atoms being ionized, subsequently trapping larger amount of energy in the disc and further increasing the temperature. This cycle continues till H is completely ionized. The thermal instability then results in viscous instability, as the increased temperature implies an increased mass accretion rate. This is more than the input mass accretion rate and so the material in the disc is eaten away at the radius. This results in a decrease of pressure and by extension, a decrease in temperature, until the hydrogen can recombine. The thermal instability is triggered again, albeit, with the cooling running away this time, till it reaches below $10^4$ K. The output mass accretion is relatively lower and the disc begins to build up again. This local instability is transferred to the next annulus in the disc, eventually resulting in a limit cycle behaviour between the standard disc with larger mass transfer rate from the companion, so the whole disc is being eaten away on the viscous timescale, to a quiescent disc where hydrogen is neutral. However, in NS and BHB systems, one also needs to take the luminous inner disc into account, which means that irradiation is also important (van Paradijs, 1996), keeping the temperature of the outer disc high enough to prevent recombination of H. This results in the exponential decay as seen in lightcurves of BHBs, if the whole disc is irradiated. Ionization instability leads to eruptions that last for months in XRBs and long-term activity cycles in AGN lasting for millions of years (Siemiginowska et al., 1996).

### 1.4.3 Radiation pressure instability

Radiation pressure instability occurs at higher mass accretion rates at small radii, as the disc goes from gas pressure dominated to radiation pressure dominated. Here, a small increase in temperature causes a large increase in pressure, which in turn increases heating, as stresses are proportional to total pressure. This large increase in temperature is not balanced by a corresponding decrease in opacity and hence leads to runaway heating. The SS disc equations do not allow for a stable solution at high temperature and predict complete disruption of the disc. However, inclusion of radial advection gives an additional cooling process along with the energy losses through radiation (Abramowicz et al., 1988). This allows for a thermal-viscous limit cycle as the one described above for H ionization instability.

SS stress prescription becomes radiation pressure unstable at luminosity $\geq 0.06$ $L_{Edd}$ to produce limit cycles. Most of the gravitational energy is released in the inner disc and hence should significantly affect the lightcurve. However, observational evidence suggests that the BHBs show a stable disc spectra upto 0.7 $L_{Edd}$. This may suggest that the classic SS prescription is incorrect. Only stress prescriptions with heating proportional to gas pressure are stable everywhere (Stella and Rosner, 1984). However, lightcurve of GRS 1915+105 (a sample of which is shown in Figure 1.2) exhibits some signatures of limit cycle in its lightcurve. Thus

it seems that the effective stress scales slower with temperature than predicted by radiation pressure, but faster than predicted by gas pressure alone. Therefore, the heating may be proportional to geometric mean of gas and total pressure (Merloni, 2003). This, coupled with effects of advection from neighbouring annuli mean that this stress prescription can be stable upto $0.4\,L/L_{\mathrm{Edd}}$ (Merloni and Nayakshin, 2006).

## 1.5 Photons as storytellers

The theories discussed above and those yet to be mentioned in this chapter can only be confirmed using observations. The data obtained from the observations are photons of different energies from different sources. These little packets of energy, traversing across space and time, are the key to unlocking the mysteries of the universe. The method of collection of data, and the instruments used are presented in detail in Chapter 2. Two final products are obtained by analysing data from the instruments. The first is the number of photons collected over time, called a *lightcurve* and the second is the photons collected across individual energy channels, called *energy spectrum*.

### 1.5.1 Light curves and Power Density Spectra

Light curves of four different sources are shown in Figure 1.2. As seen from the figure, a lightcurve shows the variation of intensity (or flux) of the source with time. A rise in intensity of the source relative to the base level, marks the beginning of an outburst. The changes in the intensity and the patterns formed in the lightcurve are generally studied under the heading of temporal properties. These variations and patterns are clearly visible when the change occurs over timescales of hours or days. However, rapid variations are seen in some sources, along with the emergence of periodic or quasi-periodic features. To study these features, we obtain the Fourier transformation of the lightcurves. This is called a Power Density Spectrum (PDS). A PDS is essentially the modulus squared of the Fourier transform of the light curve (van Paradijs, 1996). The characterization of flux in the frequency domain is useful while studying fast fluctuations in accreting sources and to clearly identify periodic and aperiodic variabilities in the source. Figure 1.3 shows a sample PDS from the X-ray transient GX 339-4 (Motta et al., 2011). The sharp, narrow features seen in the PDS are called Quasi-periodic Oscillations (QPOs), which is an example for an aperiodic variability. QPOs are seen at both low ($< 40$ Hz) and high frequencies ($> 60$ Hz) called Low Frequency QPOs (LFQPO) and High Frequency QPOs (HFQPO) respectively (Belloni, 2010). QPOs are studied by fitting the Poisson noise subtracted PDS with different models. This is usually a combination of powerlaw (if necessary)

and Lorentzian functions. The Lorentzian function is given by,

$$L(\nu) = \frac{a_0^2}{\pi/2 + \arctan(\nu_0/\Delta)} \frac{\Delta}{\Delta^2 + (\nu - \nu_0)^2} \qquad (1.36)$$

where $\nu$ is Fourier frequency, $\nu_0$ is Lorentzian peak frequency (QPO centroid frequency), $\Delta$ is the half width at half maximum (HWHM) and $a_0^2$ is the integral of $L(\nu)$ from $\nu = 0$ to $\nu = \infty$. The power spectrum can be normalized such that the integral over all positive frequencies gives the fractional root mean square (rms) deviation of the corresponding time series (Belloni and Hasinger, 1990). The rms qualifies the variability of a time series in a given Fourier frequency range. To quantify a particular feature as prominent, the *quality factor* is used, which is defined as $Q = \nu_0/2\Delta$. Generally, a Q value greater than 3 suggests that the peaked feature in the PDS can be classified as a genuine QPO.

Initially, LFQPOs were considered to be one single phenomenon with varying frequencies. However, it was found that LFQPOs display varying properties, based on which they are again divided into types (Wijnands and van der Klis, 1999; Remillard et al., 2002; Casella et al., 2005; Remillard and McClintock, 2006). Three types of QPOs are reported in BHBs called Type A, B and C respectively as shown in the panels from top to bottom in Figure 1.3. Type-C QPOs are characterized by high amplitudes reaching upto 20% and narrow peaks in the PDS with $Q \geq 8$. A number of harmonics are also detected along with the fundamental peak. Sometimes, the presence of a sub-harmonic is also observed. Type-B QPOs are observed to have moderately high amplitudes with rms upto 5% and manifest as narrow peaks of $Q \geq 6$. A weak second harmonic is seen sometimes along with a sub-harmonic. In cases where sub-harmonic and fundamental QPO have comparable amplitudes, we observe the so-called 'cathedral' QPOs (Casella et al., 2004). Type-A QPOs are the weakest of the three with rms lying within a few percent. Also, this QPO feature is broader with $Q \leq 3$. Therefore, there are only a total of $\sim 10$ significant detections of the same in the entire *RXTE* archive. Sub-harmonics and harmonics are not detected in this case. Different types of QPOs are unique to different states of the source during an outburst (this will be discussed in Section 1.6). HFQPOs are also seen in the PDS along with LFQPOs, which allows for some interesting results. HFQPOs are very rarely detected in the PDS of BH systems. The first detection was in 1997, when a $\sim 67$ Hz QPO was observed from GRS 1915+105 (Morgan et al., 1997; Sreehari et al., 2020). Since then, HFQPOs have been detected only in a handful of other sources (Belloni et al., 2012). HFQPOs are observed as single or double peaks, although simultaneous detection of double peaks (called lower and upper HFQPOs) is seen only in a few sources like GRO J1655-40 and H1743-322 (Strohmayer, 2001; Remillard et al., 2002; Remillard and McClintock, 2006). The frequencies of the simultaneous QPOs in both these cases is close to 3:2. This resulted in a few models being
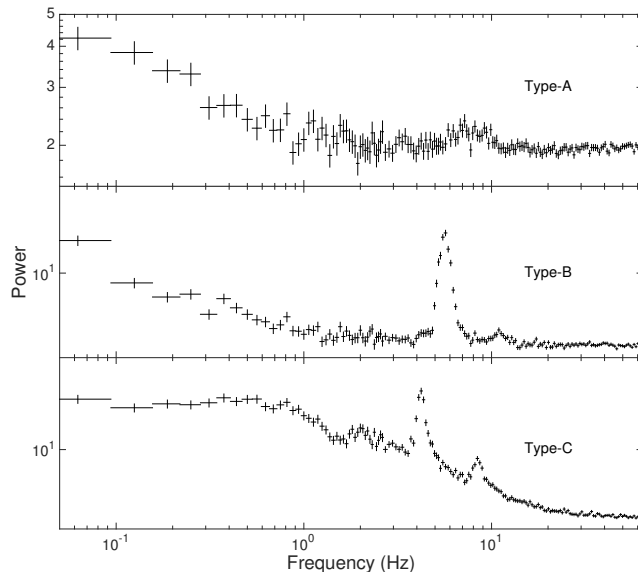
**Figure 1.3:** PDS of BHB GX 339-4 exhibiting different types of QPOs is shown (Motta, 2016). The PDS exhibit harmonics and subharmonics in type B and C QPOs along with the fundamental frequency. These features are clearly seen in type B and C QPOs shown in second and third panels respectively.

proposed which attributed the origin of these QPOs to resonance (Abramowicz and Kluźniak, 2001). HFQPOs are mostly seen in high flux states.

### 1.5.2 Energy Spectra

The distribution of photons over different energy channels gives the energy spectra. Energy spectra from BHBs can extend from 0.1 keV to hundreds of keV in X-ray energy range. Spectra are fitted with multiple models in XSPEC (Arnaud, 1996), to determine the physical origin of the spectral features. Based on the varying levels of contribution from different components, we determine the state of the source. While dealing with energy spectra, we also need to consider the absorption by interstellar medium in the line of sight of the source. Also, one should select data from particular instrument based on our energy range of interest, as different instruments are built to have better responses at certain energy ranges. This can be evaluated using the response matrix and other related files provided by the corresponding instrument team. Details of instruments used are mentioned in Chapter 2.

## 1.6   Spectral and temporal evolution

Armed with the above information, we now proceed to track the changes in the spectrum from the beginning to the end of the outburst and link it to the physical changes in the accretion disc in this section. We now know that an outburst entails changes in the accretion rate and the geometry of the disc. These changes take place in stages called 'states'. The periods where the source is not in outburst is called **quiescence**. During an outburst, the source undergoes four states - each associated with its own unique spectral and temporal properties. The evolution of the spectra holds clues as to the physical evolution of the source throughout its outburst. The spectra obtained from the source consists of two main components - a soft component below $\sim 10$ KeV and a non-thermal tail extending to 500 keV and beyond as revealed by extensive studies of the spectra of Cyg X-1 (Gierliński et al., 1999; McConnell et al., 2000). The soft component is attributed to an optically thick accretion disc which is approximated using a multi-colour disc blackbody model (Mitsuda et al., 1984), which is a representation of the standard SS disc. However, the tail of the spectrum cannot be explained using only this model. The higher energy emission suggests that at least some part of the accretion power is dissipated in an optically thin material, so that the energy does not thermalize to the disc temperature. This is referred to as 'corona'. The physical properties of the corona and the theories associated with it will be summarized in later sections. However, the notable point here is that the contribution from these two components (disc and corona) waxes and wanes as the outburst progresses, affecting the overall luminosity from the source. The division into states is primarily based on the varying contributions to the spectra from these two components.

For a clearer understanding, we follow the pattern followed by the source in the Hardness-Intensity Diagram (HID). A HID is the plot between the ratio of flux in harder to softer energy band and the total flux. The source generally traces out a distinct 'q'- shaped pattern in the HID (Deviations will be discussed in Section 1.8). A typical HID for a BHB is shown in Figure 1.4. The different states are marked on the HID along with the jet line. In the following subsections we look at the spectral and temporal features of the source in each of these states while traversing from A to E in the HID shown in Figure 1.4.

### 1.6.1   Low/Hard State (LHS)

Starting from the bottom right corner of the plot in Figure 1.4, the region between the points A and B is the hard state. The source is said to be in the hard state when the spectrum peaks in the higher energy range ($\sim 100$ keV). The source is generally less luminous in the state, hence prompting the name Low/Hard
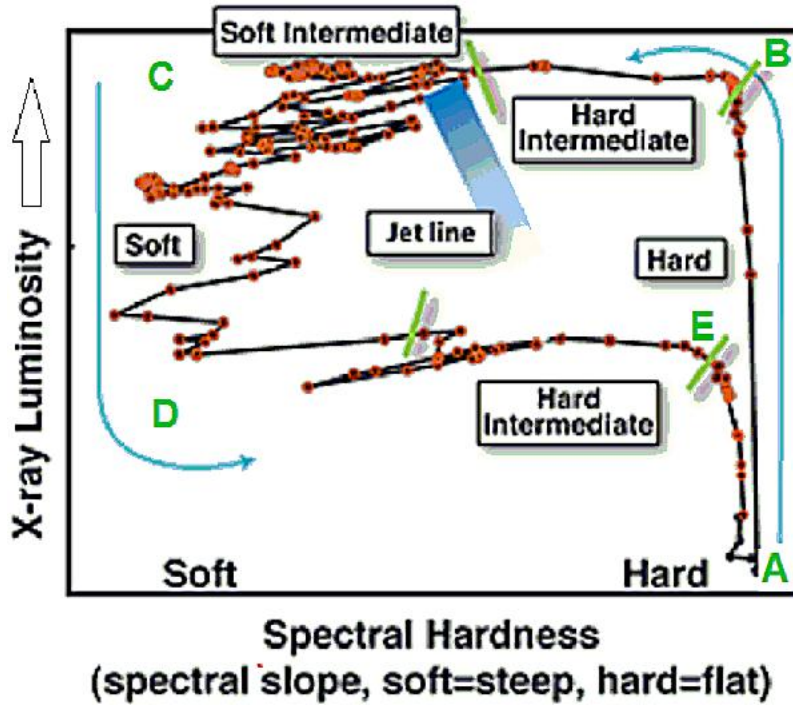
**Figure 1.4:** A typical HID of a BHB tracing out a 'q'-shaped pattern. The different states are also marked. Intermediate states are associated by appearance of jets as represented by the jet lines (Kylafis et al., 2012)

.

State. However, this naming is more conventional rather than accurate, as some sources are found to be bright even in the LHS (see Miller et al., 2015; Xu et al., 2018a,b, etc.). The spectra are broadly fit with the phenomenological power law model characterized by a photon index $\Gamma$, where photon spectrum is given by $N(E) \propto E^{-\Gamma}$. This powerlaw may have a break or cut-off at higher energies and extends upto hundreds of keV. This component is the primary contributor to the total flux. The powerlaw model is replaced by Comptonisation models, which also provide good fits to the spectra. This implies that the hard component in the spectra could be due to the Compton upscattering of soft photons by the hot electrons in the corona. In the 'pure' or canonical hard state, one does not need to include a disc component. However, it is seen that in some cases, addition of a non-dominant thermal disc component is required for best fits. The spectrum is hard with $\Gamma < 2$. Strong Band Limited Noise (BLN) components are seen in the PDS, with typical rms values of $\sim 30\%$. Type C LFQPOs are also observed in this state.

Figure 1.5 shows the schematic representation of the possible accretion geometry in the hard and soft state in the top and bottom panels respectively. The dark
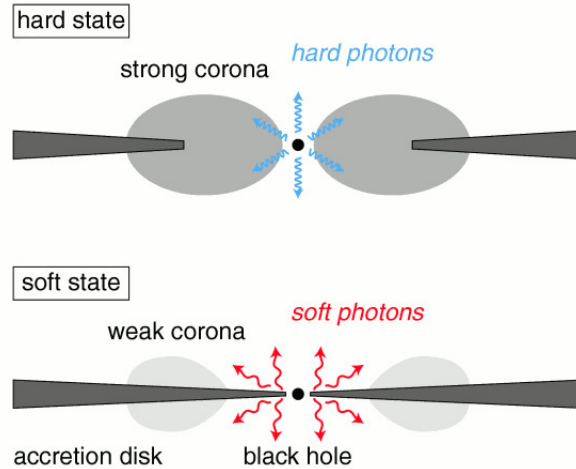
**Figure 1.5:** Schematic view of accretion in hard (top) and soft (bottom) state (Liu and Taam, 2009). In the hard state, the inner disc is evaporated and replaced by a corona, which is a source for the hard photons. The disc moves closer to the compact object in the soft state and the corona becomes weaker. Soft photons from the disc are clearly detected at this stage.

grey slab in the figure is the disc while the corona is the puffed up region shown in lighter grey. Different coronal models will be discussed later. Hard photons originate close to the compact object. Spectral properties in the hard state suggest that contribution from the disc is minimum as the soft photons detected are very less. This leads to an increase in the hardness ratio. The truncated disc model, where the disc is far away from the compact object, is shown in the top panel of Figure 1.5. The corona is strong and there is little overlap between corona and the disc. So, there are very few disc photons illuminating the coronal flow. This is further confirmed by multi-wavelength observations (IR-optical-UV-X-ray), which show that the disc has a very low maximum temperature, of the order of a few tens of eV, and a truncation radius of $100 - 300$ $R_g$ (see Esin et al., 2001, for eg.). However, exceptions exist, where the spectra can only be explained by the existence of a disc extending close to the ISCO (Ramadevi and Seetha, 2007; Miller et al., 2015; Baby and Ramadevi, 2022). Various other explanations are also put forward to explain the soft component seen in the LHS. These will be discussed later in Section 1.8 and subsequent chapters.

## 1.6.2   Hard Intermediate State (HIMS)

The source then moves from the right (B) to the top horizontal branch of the HID in Figure 1.4. This is called the HIMS. Here, the thermal disc component appears

or becomes more prominent. The powerlaw index increases from 2 to $2.5 - 3.0$. Signature of the Fe K$\alpha$ line, along with other reflection features also appear in the spectra in a few cases. The PDS shows band limited noise and strong Type-C QPOs. The fractional rms is lower than LHS ($10 - 20\%$). The characteristic frequencies of the QPOs are higher than in the LHS. The source spends less time in the HIMS ranging for just a few days.

**Jet Line**

Sometimes, the transition from the HIMS to the next state is marked by the appearance of X-ray jets (Fender et al., 2004; Belloni et al., 2005). This is marked as a *jet line* in Figure 1.4. This transition period is associated mostly with changes in PDS and a slight softening of the spectrum. However, there are some cases where the time of transition does not match with the crossing of the jets (Fender et al., 2009).

### 1.6.3 Soft Intermediate State (SIMS)

As the source reaches the Soft Intermediate State (SIMS), the spectral properties remain largely similar, although there are drastic changes seen in the temporal properties. The most striking feature is the low level of variability where the fractional rms can be as low as a few percent. QPOs of Type A or B are seen in the PDS.

### 1.6.4 High/Soft State (HSS)

The source then moves from the horizontal branch to the left of the plot towards the soft state, which is the most thermal dominant state. Here, the disc contribution accounts for the maximum flux from the source. The coronal component is weak or non-existent. The disc moves inwards towards the black hole as shown in the bottom panel of the figure 1.5. The disc component is fit simply with the *diskbb* model (Mitsuda et al., 1984; Makishima et al., 1986). The local temperature is defined as $T(r) = T_{in}.(r/r_{in})^{-3/4}$. The bolometric luminosity $L_{disc}$ is related to the maximum disc temperature $T_{in}$ and apparent inner disc radius $r_{in}$ as $L_{disc} = 4\pi r_{in}^2 \sigma T_{in}^4$. Obtaining the true radius from the apparent radius requires several corrections to be taken into account. They are

- Stress-free inner boundary condition :- The inner boundary condition is ignored in this model. The temperature drops to zero at the Innermost Stable Circular Orbit (ISCO). ISCO is the last marginally stable circular orbit, at which a test particle can orbit about the compact object. Therefore, the peak temperature is lower than the one obtained by this model as it comes from larger radii (Gierliński et al., 1999; Kubota et al., 2001).

- Colour temperature correction :- Spectral hardening due to incomplete thermalization of escaping radiation is not taken into account (Shimura and Takahara, 1995).

- Relativistic corrections :- Inclination dependence is ignored (Cunningham, 1975).

The standard disc theory is still found applicable as the $r_{in}$ remains constant in the soft state even as $L_{disc}$ changes significantly. A simple manifestation of this fact is that the sources follow the relation $L \propto T^4$ over factors of $10 - 50$ change in luminosity. This confirms that gravity is consistent with the implications of General Relativity (GR). Assuming the correctness of GR theory, this also gives a way of obtaining the spin of the black hole, provided, we place some conditional restrictions on the values of distance, mass and inclination.

After HSS, the source continues to decrease in luminosity as it goes from SIMS to HIMS and back to LHS (from D $\rightarrow$ E $\rightarrow$ A), thus completing the 'q' shaped profile seen in Figure 1.4. To summarize, it can be said that primary contribution to the radiation from the black hole binary comes from an optically thick, geometrically thin disc and the Compton upscattering of photons by a geometrically thick corona. Reflection features are obtained by the upscattered photons reflecting off the disc. As the source moves from one state to the next, the contribution from these components varies.

Until now, we have only described the spectral and temporal markers for different states, without delving deeply into the underlying physical processes. We have also brushed upon the rudimentary concept of the standard disc theory in Section 1.4.1. However, many other solutions and models are proposed to explain both spectral and temporal properties seen in different states. In the following sections, we present a brief overview of some of the models proposed to explain the evolution of the source during an outburst.

## 1.7   Accretion models - a brief overview

We have already studied the states of a BHB in outburst in the context of the standard accretion disc theory. Here, we summarize the available accretion models used to explain the observational characteristics of BHBs. The generally accepted theory is that the radiation power from the BHBs comes from accretion of gas onto the compact object, enabled by viscosity, converting gravitational potential energy to heat. So far, we have only discussed the evolution of state exclusively in the context of the standard thin disc solution of the accretion flow (Shakura and Sunyaev, 1973). The existence of an optically thin corona was briefly mentioned. However, apart from the standard thin disc solution, three other solutions exist, which are applied to BHBs. The optically thin two-temperature

disc (Shapiro et al., 1976), slim disc (Begelman, 1978; Abramowicz et al., 1988) and the advection dominated accretion flow (ADAF) (Rees et al., 1982; Narayan and Yi, 1995). Apart from these, ADIOS (Adiabatic Inflow-Outflow Solution), CDAF (Convection-dominated accretion flow) and LHAF (Luminous Hot Accretion Flow) are other solutions of accretion flows, which are different variants of ADAF. The application of these accretion models depends on the luminosity and spectra of the source. Luminosity is related to the accretion rate $\dot{M}$ as $\dot{M} = L/\eta c^2$, where $\eta$ is the radiation efficiency mentioned earlier. We know, $L/L_{Edd} = (\eta/0.1)\dot{m}$ where $\dot{m} = \dot{M}/\dot{M}_{Edd}$ and $\dot{M}_{Edd} = L_{Edd}/0.1c^2$. Broadly, the various accretion models can be applied at different limits of the Eddington-scaled accretion rate $\dot{m}$.

If

$$\dot{m} \begin{cases} \leq 0.3 & \text{thin disc model} \\ > 0.3 & \text{slim disc model} \\ \sim (0.1-0.3)\alpha^2 & \text{ADAF} \end{cases}$$

(Abramowicz et al., 1988; Narayan and Yi, 1995).

It is clear that a complete understanding of the accretion geometry requires a combination of all three models at different accretion rates. However, in our studies, we have not found evidence for the existence of a slim disc and opt for a standard disc assumption. Therefore, in the following sections, we focus on different coronal models available. The coronal models can be categorized into three different types. The first is where the corona is considered to be a hot flow between the inner edge of the disc and the BH. The second is when one assumes a 'lamp-post' geometry and the third is the 'sandwich' model, where the corona is the atmosphere flanking the inner parts of the accretion disc. Here we present examples of the three models along with a few models proposed for the origin of QPOs corresponding to two of them.

### 1.7.1 Truncated disc/hot inner flow

There is a significant difference between the spectra seen in the LHS and HSS, which cannot be explained by the application of a single accretion flow solution. As described in Section 1.6, the presence of two different stable flows can be inferred. One is the hot, optically thin, geometrically thick flow which exists at low accretion rates or luminosities called a corona, and the other is the cool, optically thick, geometrically thin disc. These are put together as the truncated disc/corona model, which can explain the observed spectra in different states. The optically thick disc is replaced by the corona at low luminosities, probably through disc evaporation (Meyer and Meyer-Hofmeister, 1994; Mayer and Pringle, 2007). A schematic representation of the same is presented in Figure 1.6. The brown slab represents the disc while the blue matter shows the corona. The evolution of the
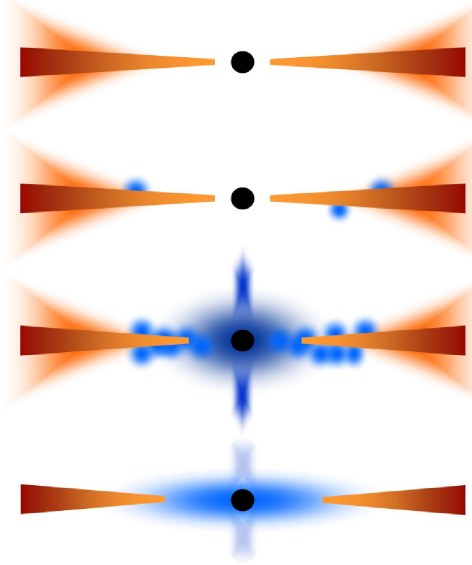
**Figure 1.6:** The changes in the accretion flow with the evolution of state is shown in the figure. Contributions from the disc and the hot inner flow vary as the source moves from LHS to HSS or from low accretion rate to high accretion rate from the bottom to top panel (Done et al., 2007).

disc from LHS to HSS is seen from the bottom to the top panel. The luminosity and accretion rate increase in the upward direction. At low luminosities, the photons available to for Compton cooling of the hot electrons in the corona are very few. Hence, it is not very efficient compared to heating from collisions of protons. This produces a hard thermal Comptonised spectra with parameters similar to those seen in the spectra during LHS. As the mass accretion rate increases, the optically thin flow becomes optically thick and evolves into an SS disc. Therefore, the efficiency of Compton cooling increases due to the availability of photons and results in a softer Comptonised spectra, which gives the soft tail in the observed spectra. The disc moves inwards as the source moves from LHS to HSS.

The inner flow is popularly identified as ADAF (Esin et al., 1997; Narayan and McClintock, 2008). It was first predicted by Ichimaru (1977), although the astrophysical applications were explained by Narayan and collaborators. ADAF is formed when most of the energy gained by the gas is advected into the black hole. This happens at low accretion rates where particle collisions are few to trigger photon generation. This unradiated heat puffs up the disc and forms an optically thin, geometrically thick structure. Therefore, ADAF is geometrically extended and radiatively inefficient. As the accretion rate increases, the disc truncation radius moves inwards. When the gas supply rate is more than the evaporation rate, Compton cooling rate increases and the disc extends to ISCO.

**Relativistic Precession Model**

Within the framework of the disc and a hot inner flow geometry, multiple models are again proposed to explain the origin of different types of QPOs. The Relativistic Precession Model (RPM) (Stella and Vietri, 1998; Stella et al., 1999) is one such model. This assumes the disc/inner hot flow geometry. The LFQPO fundamental frequency is associated with the Lense-Thirring precession frequency at a particular radius, most likely to be the disc truncation radius. The lower and upper HFQPOs correspond to the periastron precession and orbital motion. It is postulated that bright clumps of matter are spread all along a particular radius of the elliptical orbits that are slightly tilted with respect to the Black hole equatorial plane, allowing for both periastron precession and Lense-Thirring effect. Relativistic Doppler boosting can then modulate the flux (Bakala et al., 2014). As the disc moves inwards, the frequencies associated with it increase, resulting in the observed QPO evolution. Multiple modifications have been applied to these models to explain the evolution of QPOs in different states and sources like the precessing inner flow model (Ingram et al., 2009). The origin of type-B QPOs is associated with the relativistic precession of the jet (Kylafis et al., 2020) while type-C QPOs seem to originate from the precessing inner flow (Ingram et al., 2009; Axelsson et al., 2014).

### 1.7.2 Disc/lamp-post corona

In some cases, a jet ejection is observed during the transition from HIMS to SIMS (Figure 1.4). It is postulated that a steady jet exists during the hard state, which is later ejected and gets quenched in the soft state (Fender et al., 2004). The second type of coronal model assumes that the corona actually forms the base of the jet (Markoff et al., 2001, 2005) or an aborted jet (Ghisellini et al., 2004). It is also referred to as the light-bending model (Miniutti and Fabian, 2004). This corresponds to the lamp-post geometry, where, the corona, either compact or extended, is at a certain height from the accretion disc. Models currently in use assume a point like source above the black hole spin axis. The disc is illuminated by the corona. The photon trajectories close to the black hole are strongly affected by gravity. In the standard picture, the disc emissivity varies as $r^{-3}$, where r is the disc radius (Shakura and Sunyaev, 1973; Novikov and Thorne, 1973). However, steeper emissivity profiles have been observed (Miniutti and Fabian, 2004; Miller, 2007), which can be explained using a lamp-post model as light bending effects will focus light on the inner regions of the accretion disc. Thus for small r, emissivity profile falls off steeply, and conforms to the $r^{-3}$ dependence at larger radii (Miniutti and Fabian, 2004). Recent studies with reverberation lags also suggest a corona which contracts in the hard state and expands vertically in the intermediate state (Kara et al., 2019; Wang et al., 2021). This disc-corona-jet geometry is presented

in Wang et al. (2021), where the steady jet is observed when the source emits at luminosity more than 4% of $L_{Edd}$. This is shown in Figure 1.7.
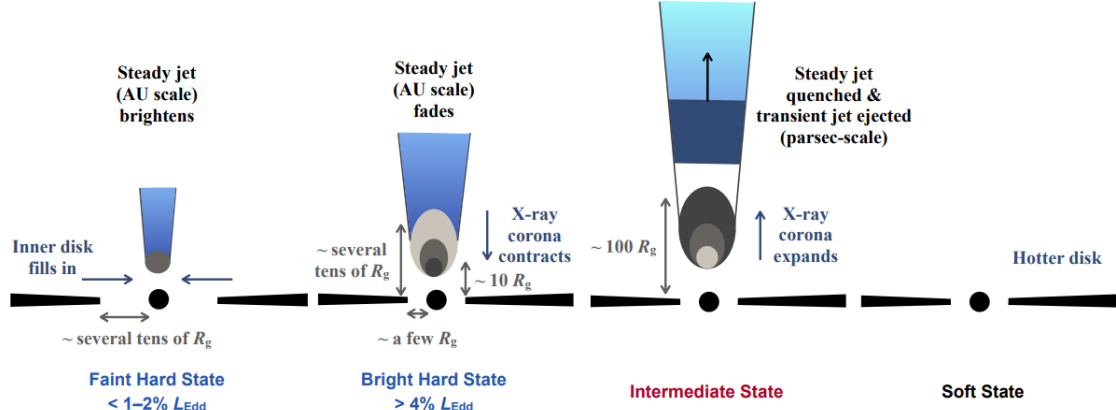


**Figure 1.7:** The disc-corona-jet system evolution is shown in the hard to soft state. The steady makes an appearance in the bright hard state along with a contracting corona. The bright hard state corresponds to the top right part of the plot in the HID shown in Figure 1.4. The corona expands in the intermediate state along with the ejection of the jet. Only a hot disc is left in the HSS. (Wang et al., 2021)

### 1.7.3 Two Component Advective Flow Model

The Two Component Advective Flow Model (TCAF) was proposed by Chakrabarti and Titarchuk (1995a). It consists of an optically thick, Keplerian disc flanked by optically thin, sub-Keplerian halo. Matter flows through the disc, towards the standing shock, which is close to the centrifugal barrier. The post-shock region puffs up and forms a torus close to the black hole. A schematic representation of the model is presented in Figure 1.8. The inner, puffed up post-shock region is referred to as Centrifugal Pressure Supported Boundary Layer (CENBOL). The contribution from the sub-Keplerian component increases during the hard state, along with an increase in the size of CENBOL. During the soft state, Keplerian component is dominant, with minimal contribution from the sub-Keplerian flow and a decrease in CENBOL size. This provides an explanation for the observed state transitions.

**Propagating oscillatory shock**

Propagating Oscilltory Shock model follows the TCAF geometry described above. There is a sharp change of density from the sub-Keplerian halo flanking the disc and the inner halo close to the black hole. The pre-shock and post-shock halo or corona are separated by a shock location at a particular radius. The shock
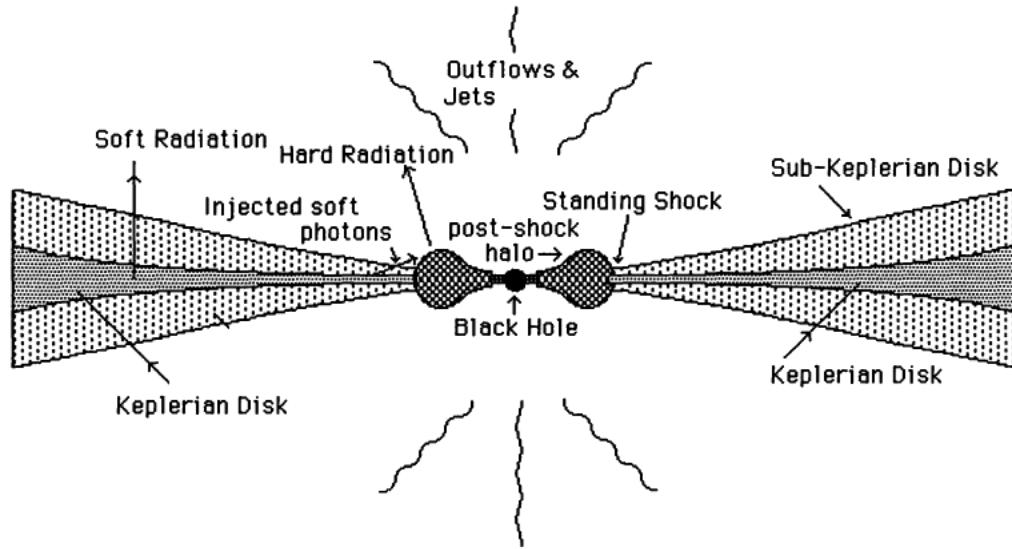
**Figure 1.8:** Schematic diagram of accretion flow around a black hole following the two component advective flow model. The Keplerian, optically thick is sandwiched between a sub-Keplerian halo. The post-shock halo is the source of hot electrons that Comptonize the soft photons from the Keplerian disc (Chakrabarti and Titarchuk, 1995a).

location can oscillate about the mean radius if either the cooling timescale of the halo matches the infall timescale (Molteni et al., 1996) or the Rankine-Hugoniot condition for a stable shock is not satisfied (Ryu et al., 1997). This accounts for the variation in the centroid frequency of the QPOs.

## 1.8 Deviations from the norm

The above definitions and categorizations are based on the generally observed characteristics of BHBs. Sometimes, it so happens, that a few sources stray completely off the established path and exhibit some peculiar characteristics. These exceptions are not few and far between, but are rather prevalent across multiple sources and states. Here, we expand on several of them, relevant to this work.

### 1.8.1 Relation between luminosity and temperature in soft state

As mentioned earlier, simple models of constant radius and constant colour temperature correction disc predict the relation $L \propto T^4$, which is seemingly followed by most of the BHBs in the disc dominated states. However, some deviations are seen at higher luminosities, where the spectra seem to follow the relation $L \propto T^2$ rather than $L \propto T^4$ (Kubota and Makishima, 2004). This could possibly be due

to the following reasons; either the assumption that the colour temperature correction is constant and/or inner disc radius is constant is false, and/or the disc temperature structure is different than the one considered in the standard disc structure, i.e., it does not follow $T(r) \propto r^{-3/4}$.

At higher luminosities and higher temperatures close to 1 keV, metals become completely ionized and the opacity is very low. This can give an increase in the colour correction factor ($f_{col}$) (Davis et al., 2006). This depends on the optical depth of the disc and therefore on $\alpha$. The models with $\alpha \sim 0.01$ seem to match the bend seen in one such source, XTE J1550-564 (Davis et al., 2006). However, the rapid rise requires $\alpha \sim 0.1$ (Lasota, 2001), which does not match with the observed bend. Also, several other sources with the same temperature-luminosity range seem to have a different bend than the one seen for the source XTE J1550-564 and a few do not seem to show the bend at all.

Another possible cause for deviation from the standard relation is the optically thick advection. At larger luminosities, the energy released close to the disc is swept along with the flow to smaller radii and does not have time to escape to the photosphere. Therefore the luminosity of the hottest parts of the disc, close to the compact object, is suppressed. For a disc temperature distribution which follows $T(r) \propto r^{-p}$, p goes from 3/4 in the standard regime to 1/2 in this case (Kubota et al., 2001; Kubota and Makishima, 2004; Abe et al., 2005). However, this effect should be global and applicable to all BHBs, which does not seem to be the case for other sources at similar luminosity and temperatures (Gierliński and Done, 2004). Alternatively, it is also possible that the difference here is that the sources in which this effect is observed are at higher inclinations ($\geq 70°$), which is true for GRO J1655-40, XTE J1550-564 and probably 4U 1630-472 (Tomsick et al., 1998). As a result of the high inclination, the geometrically thick part of the disc could start self-shielding its inner regions, or the equatorial disc wind becomes optically thick, so that the luminosity observed is only a fraction of the intrinsic luminosity (Done et al., 2007).

### 1.8.2 Lack of apparent state transitions

The HID presented in Figure 1.4 is a typical example of the HID observed for BHBs. However, there are a few sources, which do not conform to this general picture. That is to say that the sources do not trace out the 'q' shaped pattern in the HID. More often than not, this is also accompanied by lack of state transitions in the source during an outburst. Sources which show lack of state transitions are those which remain either in the soft or the hard state for most of the duration of the outburst i.e., they are mostly disc dominant in some cases, or, the radiation is dominated by the powerlaw component in the rest (Tanaka and Lewin, 1995; Remillard and McClintock, 2006). The data points of the HID remain bunched

up either on the left of the plot (in case of disc-dominant) or right of the plot (for powerlaw dominant), with quick and faintly detectable transitions to hard or soft state respectively. Moreover, it has also been observed that a few sources which were classified as 'Soft X-ray transients (SXTs)' based on the observations of the initial few outbursts, were later found to remain in the LHS in subsequent outbursts (Brocksopp et al., 2004).

The standard truncated disc/hot inner flow model is insufficient to explain this anomaly. In the absence of transition to a hard state, it is difficult to explain the transition to quiescence without the introduction of an advection dominated accretion flow. Additional elements like existence of disc winds and disc irradiation have to be included to explain the high luminosities (see Hameury, 2020, for a review). Similarly, the absence of soft state in the so-called 'Low Hard X-ray Transients' is also difficult to explain in the context of the generally accepted models. One possible explanation is that these sources have low peak luminosities and low orbital periods, resulting in lower mass accreted onto the disc (Meyer and Meyer-Hofmeister, 1984).

## 1.9 Motivation for the present work

In the present work, we look at multiple BHB sources like 4U 1630-47, MAXI J0637-430 and Swift J1753.5-0127. The first two sources are classified as soft sources i.e., the source remains disc-dominant throughout the outburst. The third source was previously classified as a Low Hard X-ray Transient. However, from the time the source was detected in 2007, it was found to remain in outburst for almost $\sim 12$ years, with the source undergoing transitions to intermediate states.

From the discussion on the various models to explain the geometry of BHBs, it is clear that there is no consensus on the model which describes the physics behind the transitions. All these models and their variations are independently applied to different outbursts in different sources in an attempt to understand the accretion geometry. These studies are largely done on sources which undergo the canonical outburst i.e., which show a complete evolution from LHS to HSS and back to LHS, through intermediate states. Here, we perform spectral and temporal analysis of the sources which stray away from the conventional path. We attempt to constrain the accretion geometry in such sources based on the spectral and temporal properties. Also, as detailed in Section 1.8, certain sources show some deviations from the expected trends. We attempt to explain the deviations observed in the selected sources in the context of the existing models. We also attempt to obtain mass estimates of the black hole in 4U 1630-472 and MAXI J0637-430 using different methods. These methods are detailed in the relevant chapters. We use frequency-resolved spectroscopy to study the QPO evolution of Swift J1753.5-0127, which exhibits type-C QPOs, in order to constrain the

accretion geometry.

Chapter 2 contains a description of the instruments and methodology used to perform the analysis. The results of the analysis performed on the data obtained from the 2016 and 2018 outbursts of 4U1630-472, 2019 outburst of MAXI J0637-430 and the decay phase of the $\sim$ 12 year-long outburst of Swift J1753.5-017 are presented in Chapters 3, 4 and 5 respectively. The material presented in Chapters 3, 4 and 5 are already published in Baby et al. (2020, 2021) and Baby and Ramadevi (2022) respectively. Finally, in Chapter 6, we present the summary of the current work and hint at the possible avenues of exploration in the future. In Chapter 7, we list out the recommendations based on this work.

# Chapter 2

# The journey of data - from observatories to end products

When one thinks of data collection in astronomy, the ancient image of an astronomer peering at the night sky through a telescope and jotting down numbers in a dainty little notebook comes to mind. However, modern astronomy has significantly evolved with the advancement in technology. Data is now collected at observatories (ground and space) and uploaded onto public servers, which can then be used by any eager researcher sitting in front of a computer, in the comfort of his/her own home/office. The instruments used to collect the data are uniquely designed based on the complexity of the field. Study of X-ray binaries necessitates the need for specialized equipment in the form of detectors, which can provide good spectral and temporal resolution. Observations from various instruments are used in the present study, based on relevance and data availability. *Rossi X-ray Timing Explorer (RXTE)*[1] (Bradt et al., 1993), with three instruments onboard, provides broadband X-ray energy spectrum, excellent timing resolution in a particular energy band and near-continuous monitoring of different sources. Details regarding the individual instruments are given in Section 2.1. We use *Proportional Counter Array (PCA)* to obtain energy spectrum and lightcurve with good resolution in the $2 - 30$ keV energy band. *High Energy X-ray Timing Experiment (HEXTE)* gives X-ray spectrum in the energy band $20 - 150$ keV, with moderate spectral resolution. The *All Sky Monitor (ASM)* is used to generate lightcurves to track the evolution of the source. In the post *RXTE* era, *AstroSat*[2] (Agrawal, 2006) has emerged as a worthy successor for *RXTE*, providing data with good spectral and temporal resolution in UV and X-rays, using four pointed instruments and a sky monitor. Here we focus on the *Soft X-ray Telescope (SXT)* and *Large Area X-ray Proportional Counter (LAXPC)* onboard *AstroSat* to study the X-ray sources

---

[1] https://heasarc.gsfc.nasa.gov/docs/xte

[2] https://www.issdc.gov.in/astro.html

in the $0.3 - 80$ keV energy range. Data from *Neutron Star Interior Composition Explorer (NICER)*[3] (Gendreau et al., 2016) and *Neil Gehrels Swift Observatory (Swift)*[4] (Burrows et al., 2005; Barthelmy et al., 2005) are also used to study the soft spectra. Lightcurves are generated using *Monitor of All Sky X-ray Imaging (MAXI)*[5] (Matsuoka et al., 2009) to keep track of long-term variations in the source.

In Section 2.1, we provide an overview of all the instruments used. Table 2.1 gives a summary of the specifications of different instruments. The detector type, energy or wavelength range of operation, the Field of View (FOV) and the energy, timing and angular resolution are listed, wherever applicable. Data reduction techniques are detailed in Section 2.2. Sections 2.3 and 2.4 describe the methods used for spectral and temporal analysis. Contamination from nearby sources is a problem which hounds observations from all large area detectors, like those onboard *RXTE* and *AstroSat*. The contamination issue was encountered during the study of the source 4U 1630-472, while it had to be ruled out for the newly discovered source MAXI J0637-430. In Section 2.6, we discuss ways to tackle this issue in *LAXPC* onboard *AstroSat*, using a walk-through example of contamination from the source IGR J16320-4752 in the observation of 4U 1630-472.

## 2.1 Collecting the data

The first step is the collection of data from different sources. A brief summary of different missions serving this particular need is given in Table 2.1. Here, we also elaborate a little more on the specifications and capabilities of these instruments.

We primarily use data from India's first multi-wavelength satellite *AstroSat* (Agrawal, 2006; Singh et al., 2014) for most of this work. *AstroSat* was successfully launched on 28 September 2015 and has been aiding new and exciting discoveries in the field of astronomy ever since. It consists of four co-aligned instruments used for pointed observations of a source of interest. A *Scanning Sky Monitor (SSM)* (Seetha et al., 2006; Ramadevi et al., 2017) is also included, which scans the sky periodically, keeping an eye out for outbursts in known sources or random bright events leading to the discovery of new, hitherto unknown ones. Of the four co-aligned instruments, the *Soft X-ray Telescope (SXT)* (Singh et al., 2014, 2017), *Large Area X-ray Proportional Counter (LAXPC)* (Yadav et al., 2016; Antia et al., 2017) and *Cadmium Zinc Telluride Imager (CZTI)* (Vadawale et al., 2016) observe

---

[3]https://www.nasa.gov/nicer

[4]https://www.swift.psu.edu

[5]http://maxi.riken.jp/top/index.html
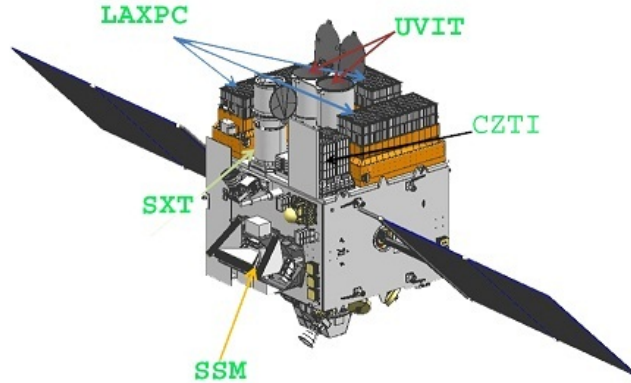
**Figure 2.1:** A schematic representation of *AstroSat*. *AstroSat* has five onboard instruments. *SXT* and *LAXPC*, the pointed X-ray instruments, are primarily used on our studies. *UVIT* and *CZTI* generate images in the UV and X-ray band respectively. *SSM* is a scanning monitor, which operates in the $2-12$ keV energy band.
Image credit : https://www.issdc.gov.in/astro.html

the source purely in X-rays. The *Ultra-Violet Imaging Telescope (UVIT)* (Tandon et al., 2017) looks at the source in UV.

Our analysis pertains to the X-ray band of the electromagnetic spectrum. Therefore, only two of the five instruments - *SXT* and *LAXPC* onboard *AstroSat*, are used primarily in our studies. *SXT* is a focusing telescope with X-ray CCD imaging camera which operates in two modes - Photon Counting (PC) and Fast Windowed (FW) mode. With an energy resolution of 90 eV at 1.5 keV and a total effective area of 90 cm$^2$, *SXT* provides moderate energy resolution to study the soft X-ray spectra in the $0.3-8$ keV range. *LAXPC* consists of 3 proportional counters *LAXPC10, LAXPC20* and *LAXPC30*. *LAXPC30* was switched off on 8 March 2018 due to significant gain changes. A gain adjustment was also made to *LAXPC10* in the last week of March 2018 (Antia et al., 2021). Therefore, we limit our analysis to data from *LAXPC20* for all the sources. *LAXPC* operates in the energy range $3-80$ keV and has an effective area $> 2000$ cm$^2$ at $5-30$ keV. With the timing resolution of 10 μs, *LAXPC* is ideally suited for detailed spectro-temporal studies of BHB sources. However, the large FOV of the *LAXPC* $(1° \times 1°)$ makes the data susceptible to contamination from nearby sources. This will be discussed at length in Section 2.6.

| Mission | Instrument | Detector | FOV | Operational range | Resolution |
|---------|-----------|----------|-----|-------------------|------------|
| *RXTE* | PCA | Proportional Counter | 1° | 2 − 60 keV | Energy : < 18% at 6 keV, Timing : 1μs |
| | HEXTE | Phoswich Scintillation Detectors | 1° | 15 − 150 keV | Energy : 15% at 60 keV |
| | ASM | Position Sensitive Proportional Counter | 6° ×90° (3) | 2 − 10 keV | Angular : 3′ × 15′ |
| *AstroSat* | SXT | X-ray CCD | 40′ | 0.3 − 8 keV | Energy : ∼ 2.3% at 5.9 keV, Timing : 2.4 s (full frame) |
| | LAXPC | Proportional Counter | 1° × 1° | 3 − 80 keV | Energy : 20% at 6.4 keV, Timing : 10 μs |
| | UVIT | Photon Counting CMOS Imagers | 0.5° | ∼ 130 − 530 nm | Angular : 1.8″ (UV) |
| | CZTI | CdZnTe Detector | 6° × 6° | 10 − 150 keV | Energy : 6% at 100 keV |
| | SSM | Position Sensitive Proportional Counter | 10° × 90° (3) | 2 − 10 keV | Angular : 12′ × 2.5° |
| *NICER* | XTI | Silicon Drift Detector (SDD) | ∼ 30 sq. arcmin | 0.2 − 12 keV | Energy : 2.3% at 6 keV, Timing : 300 ns |
| *Swift* | XRT | CCD | ∼ 24′ × 24′ | 0.2 − 10 keV | Energy : 2.3% at 6 keV, Timing : 1.8 ms |
| | UVOT | CCD | 17′ × 17′ | 170 − 650 nm | Angular : 0.9″ |
| | BAT | CdZnTe Detector | 120° × 60° | 15 − 150 keV | Angular : 20′ |
| *MAXI* | GSC | Gas Proportional Counter | 160° × 1.5° | 2 − 30 keV | Angular : 1.0° − 1.5° |
| | SSC | CCD | 1.5° × 90° | 0.5 − 12 keV | Angular : 1.5° |

**Table 2.1:** The specifcations of different missions used in this studies is tabulated above. The Detector type, FOV, Energy/Wavelength range and the resolution are given. Only the instruments operating in the X-ray energy range have been utilized in all cases.

The *Neutron Star Interior Composition Explorer (NICER)* onboard the International Space Station (ISS) is another instrument utilized for its high sensitivity in the soft X-ray region. It was launched aboard a SpaceX Falcon 9 rocket on 3 June 2017. *NICER's X-ray timing (XTI)* instrument consists of an aligned collection of 56 concentrator optics (XRC) and silicon drift detector (SDD) pairs. It operates in the $0.2 - 12$ keV range with spectral resolution of a few percent and an unprecedented timing resolution of 100 ns. Although the primary science motivation of the instrument is to study neutron stars, it can be used to study the BHBs in soft state as well. Moreover, the spectra are found to be free from pile-up effects even for Crab or Crab-like sources, which makes it an ideal instrument to study BHBs in bright, soft states. Hence, we use the data from this instrument to study the soft state of the new BHB MAXI J0637-430.



**Figure 2.2:** A view of *NICER* X-ray timing instrument without the protective blanketing. Image credit : https://www.nasa.gov/content/about-nicer

The *Rossi X-ray timing Explorer (RXTE)* provided X-ray astronomers with a wealth of data for over 16 years of its operational lifetime. The spacecraft carried 2 pointed instruments, named the *Proportional Counter Array (PCA)* and *High Energy X-ray Timing Experiment (HEXTE)*. An *All Sky Monitor (ASM)* was also included, which scanned 80% of the sky in every orbit. *PCA* operated in the 2-60 keV range with an energy resolution $< 18\%$ at 6 keV and a temporal resolution of 1 μs. It consisted of 5 proportional counters with a total effective area of 6500 cm$^2$. Meanwhile, *HEXTE* operated in the $15 - 250$ keV range with the energy resolution of 15% at 60 keV and sampling time of 8 μs. It consisted of 2 clusters (A and B), each with an effective area of 800 cm$^2$. *RXTE* served to fill a vast gulf of knowledge in the field of X-ray binaries with its fast timing and broadband spectroscopy capabilities. FRS studies requires excellent spectral and

temporal resolution, which was possible only with this instrument as it was the lone high-resolution instrument in operation during the peak of the outburst in Swift J1753.5-0127.

*Neil Gehrels Swift Observatory*, launched on 20 November 2004, is primarily commissioned to detect gamma ray bursts (GRBs) using the *Burst Alert Telescope (BAT)*. The position of the GRB is later localized by detecting the afterglow using the *X-ray Telescope (XRT)* and *Ultra-Violet and Optical Telescope (UVOT)*. *XRT* operates in the $0.2 - 10$ keV range. Effective area of *XRT* is 110 cm$^2$ at 1.5 keV and can be operated in Imaging, Timing and Photon Counting mode. Pointed observations of MAXI J0637-430 with *Swift/XRT*, used in this work, help for continuous tracking of the spectral evolution in the source.

Lightcurves from different monitors like *RXTE/ASM* and *MAXI* are used to study the long term outburst evolution of all the sources as and when applicable. In the following sections, we provide a brief overview of the spectral and temporal analysis methods used in general in the work presented here. A detailed description is provided in the subsequent chapters, wherever required.

## 2.2   Data Reduction - Obtaining the end products

Once the necessary data is obtained from the required instruments, further refinements need to be performed on this data, for it to be ready for spectral and temporal analysis, leading to physical interpretations and scientific discoveries. This is achieved by following a series of steps or a 'recipe', specific to each instrument, which is provided by the corresponding instrument team. It corrects the data for instrumental and orbital effects, enabling an error-free study. In the following sub-sections, we briefly outline the data reduction techniques followed for each instrument.

### 2.2.1   *AstroSat-SXT* and *LAXPC*

All the observations obtained with *SXT* for this work are performed in the Photon Counting Mode (PC). Level 1 files are obtained from the *astrobrowse* website maintained by ISSDC[6]. Next, we follow the steps provided in the TIFR website[7] to obtain the end products. Level-1 files are processed using the `sxtpipeline`, which generates Level 2 cleaned event files. Event files are generated separately for all the orbits in a particular ObsID. Since *LAXPC* is the primary instrument in all the observations considered, *SXT* observes the source only for 40% of total observing time. Therefore, it becomes imperative to combine the event files from different orbits in each ObsID for better statistics. For this purpose, we use the

---

[6]http://astrobrowse.issdc.gov.in/astro_archive/archive

[7]www.tifr.res.in/~astrosat_sxt/dataanalysis.html

`julia` code to merge the event files and omit the repeated good time intervals. This merged event file is then analysed using `xselect` to obtain the energy spectrum (.pha file), image file (.img) and the lightcurve (.lc).

Lightcurve is generated with a bin time of 2.3775 s, which is the resolution of the PC mode data. Timing filters are used when necessary to get rid of spurious peaks seen in the lightcurve due to instrumental effects. Image is also generated with the same bin time. According to *AstroSat* handbook[8], the observation is likely to be piled-up if the count rate is greater than 40 counts s$^{-1}$. In such a scenario, an annular source region has to be selected, such that, by excluding the central region, the source count rate comes down to less than 40 counts s$^{-1}$. This source region is then used to extract the spectrum. The response file and blank sky background files are provided by the *SXT* team[9], which can be used directly. The ancillary response files are provided for the case where the source is exactly at the centre of the image and no exclusion of source region is performed. If the source is at an offset from the centre and/or a central region is excluded to avoid pile-up effects, the ancillary response file has to be generated using the `sxtARFModule` provided with the *SXT* analysis software. The spectrum, obtained using `xselect`, is then grouped by a minimum of 30 counts per bin for better statistics. This is then loaded into `XSPEC` for spectral fitting.

Of the three proportional counters onboard *AstroSat*, we primarily use *LAXPC20* for spectral and timing analysis, as it is currently unaffected by gain issues. Event Mode data is obtained from *LAXPC20*, which is used to generate lightcurves and spectra. The software for analysis is provided by the team, along with blank sky observations taken every month, to be used as background. The pipeline codes and response files are periodically updated and hosted at TIFR website[10]. For all the data analysis performed in this work, we used `laxpcsoft` versions ranging from v1.1 to v3.0, based on the time of analysis and the latest software version available. Two executable files, namely `laxpcl1.e` and `backshift_v3.e` are generated, which are used to obtain the source and background files respectively. We only used the top layer and single event data for our analysis to avoid instrumental effects due to other layers and ignore multiple detections of the same event. The total energy is obtained in 1024 energy channels in each detector. However, for better statistics, 2 channels are grouped together in *LAXPC10* and *LAXPC30* and 4 channels are grouped together in *LAXPC20*. The lightcurves are obtained in 1s bin in different energy bands, $3-6$, $6-13$ and $13-60$ keV to study the long term evolution of the source and obtain HIDs. PDS can be generated upto 1000 Hz with the unprecedented temporal resolution of 0.5 ms. Since our studies mostly deal with soft sources where QPOs are undetected, we generate PDS upto

---

[8]https://www.iucaa.in/~astrosat/AstroSat_handbook.pdf

[9]http://astrosat-ssc.iucaa.in

[10]http://www.tifr.res.in/~astrosat_laxpc/LaxpcSoft.html

10 Hz and divide it into 8192 intervals, the average of which gives the final PDS. Dead-time corrections had to be applied in earlier versions of the software (before v2). The PDS are generated in frequency space with rms normalization.

### 2.2.2  NICER

`NICERDAS` version 7.0 is used to obtain the clean event file[11]. We use the latest CALDB files (20200722) available at the time. The event file is screened considering standard criteria i.e., a pointing offset $< 54''$, dark earth limb $> 30°$, bright Earth limb $> 40°$ and excluding the time duration when the instrument passes the South Atlantic Anomaly (SAA) region. Data from detectors 14 and 34 is removed using `fselect` command as they are reported to show episodes of increased electronic noise. Time intervals showing strong background flare-ups, where the average background count rate in the $13 - 15$ keV band is greater than 1 count s$^{-1}$, is excluded to generate the final Good Time Intervals (GTIs). The background is calculated using the 3C50_RGv5 model provided by *NICER* team. The latest version of RMF provided by the team is used. The ARF files for 50 detectors are co-added to generate the final ARF file.

### 2.2.3  RXTE

Standard-2 files are used to generate the time averaged spectra from *PCA* data in the $3 - 25$ keV range. The list of files is generated using the `xdf` command, which is then given as an input to `saextrct` to generate the source pha file[12]. Standard filtering criteria is applied to generate the GTI file i.e. the elevation angle (angle between Earth's limb and target subtended by spacecraft) is greater than $10°$, the offset between the position of the source and the spacecraft pointing is less than 0.02 and the exclusion of data within 30 minutes of peak of South Atlantic Anomaly region. The command `runpcabackest` is then used to create background files and the same procedure as above is followed to obtain the final pha file for the background. Response files are generated using `pcarsp` command. Event files are used to generate the lightcurves with a bin time of 8 ms. We use only PCU2 data for both the spectral and light curve extraction. Standard procedures are used to extract *HEXTE* data to obtain the energy spectrum from $25 - 150$ keV. Only Cluster B is used as Cluster A had stopped rocking at that point.

### 2.2.4  Swift-XRT

The *Swift-XRT* data is used sparingly in this work, only to complement the data using other instruments in specific cases. Although manual data reduction tech-

---

[11]https://heasarc.gsfc.nasa.gov/docs/nicer/nicer_analysis.html
[12]https://heasarc.gsfc.nasa.gov/docs/xte/recipes/cook_book.html

niques exist and are detailed by the *Swift* team, the online reduction tools are recommended to generate the final products to be used for analysis[13]. *Swift-XRT* spectra are obtained in WT mode and the $0.5-10$ keV spectra are generated using the standard online tools provided by the UK *Swift* Science Data Centre (Evans et al., 2009).

## 2.3 Spectral Analysis

The final pha files are loaded into XSPEC to perform the spectral fitting along with the response and background files. As detailed in Chapter 1, spectra from black hole binaries are typically modelled using a multicolour disc blackbody component and a Comptonisation component. As a first approximation, the spectra are fit with *diskbb* (Mitsuda et al., 1984; Makishima et al., 1986) and *powerlaw* models existing in XSPEC. The interstellar absorption is accounted for by using an absorption model *TBabs* (Wilms et al., 2000) where elemental abundances are set according to wilm (Wilms et al., 2000) and cross-section is set to vern (Verner et al., 1996). Further components are added, or existing components replaced, till better fits are obtained. In XSPEC, the criteria for best fit is when the statistic calculated for a particular data and model is minimum[14]. We use the chi-square statistic for our fits. This is obtained by,

$$\chi^2 = \sum (D_i - M_i)^2 / \sigma_i^2 \tag{2.1}$$

where $D_i$ and $M_i$ are the observed and model counts respectively and $\sigma_i^2$ is the variance. The parameters are varied and different model combinations are tried, till the reduced $\chi^2 \sim 1$. The reduced $\chi^2$ is obtained by dividing the $\chi^2$ value with the degrees of freedom. ftest command is used to check if the fits obtained with an additional component are significant enough for the component to be included. For a more physical understanding of the source, the *powerlaw* model is replaced by *nthComp* (Życki et al., 1999) model which considers the Comptonisation of seed disc photons by the hot electrons in the plasma. The *thcomp* model (Zdziarski et al., 2020) is a more accurate version of *nthComp*, which is used in the analysis of the source MAXI J0637-430. In some cases, we also consider the *kerrbb* (Li et al., 2005) model, where a rotating black hole is assumed. This was used to obtain a rough estimate of mass or spin of the black hole, when the disc flux contributes to more than 70% of the total flux. Flux is obtained in different energy bands and for each individual component using cflux command, by fixing the norm of the required component to a non-zero value. The errors on individual parameters are obtained using the error command. This gives the parameter values for which

---

[13]https://www.swift.ac.uk/user_objects/
[14]https://asd.gsfc.nasa.gov/XSPECwiki/statistical_methods_in_XSPEC

the statistic is greater than 2.706 of its best-fit value (90% confidence interval). In this work, errors are quoted with 90% confidence, unless stated otherwise.

## 2.4 Temporal Analysis

The PDS is generated using *powspec* command available with `XRONOS` in `FTOOLS` with rms normalization in units of $(\text{rms/mean})^2 \text{ Hz}^{-1}$. The fitting is performed in Quick and Dandy Plotter (QDP) with simple powerlaw or Lorentzian models. The formula for Lorentzian is already given in equation 1.36. In soft states, which is a focus of most of our studies, the spectra can be fit by a weak powerlaw component. In the hard states, marked by rapid variability, multiple Lorentzians are required to account for the band limited noise, the QPOs, their harmonics and sub-harmonics. The rms of the total PDS or individual components is obtained by integrating the power in the frequency range of interest (Remillard and McClintock, 2006). The `fit err` command is used to obtain the error on each parameter. The error on these parameters is then propagated to obtain the error on rms.

## 2.5 Frequency Resolved Spectroscopy

In Chapter 5, we have used Frequency Resolved Spectroscopy (FRS) (Revnivtsev et al., 1999; Sobolewska and Życki, 2006) to comment on the accretion geometry of the source. This is done only using *RXTE/PCA* data. To generate the FRS of the QPOs, we chose the event files with a timing resolution > 8 ms. The observations are chosen where the channels are not binned together for different energy ranges, thereby allowing us to perform an energy dependent analysis. We then use `stingray` (Huppenkothen et al., 2019), a module available in `python`, to generate the PDS for each energy channel in rms normalization Belloni and Hasinger (1990); Miyamoto et al. (1992). We obtain the power in the frequency range of the QPO. These rms values are then used to obtain counts using the relation,

$$S = R \times \sqrt{P\delta f} \tag{2.2}$$

where R is the count rate, P is the summed power and $\delta f = 1/T$ where T is the length of the segment. This is converted to a pha file using `ascii2pha` command. It is then loaded into `XSPEC` with the response files generated for Std2f files and fit with available models.

## 2.6 Contamination from other sources in the LAXPC FOV Walk through example : 4U 1630-472

*LAXPC* has a collimated FOV of $0.9° \times 0.9°$ at FWHM (Antia et al., 2017). This makes it likely that the data obtained from the source could be contaminated by other sources in a crowded FOV. In our analysis, we had to account for this effect in the study of 4U 1630-472. Extreme caution has to be exercised in such cases to avoid errors in the spectral analysis. The methods used to counter the contamination from nearby sources is explained using the case of contamination of data of 4U 1630-472 by IGR J16320-4751. Details of both sources will be given in Chapter 3. Here we will only outline the method to estimate the level of contamination and criteria to choose the energy range in which the spectral modelling can be performed. This involves the following steps:

- List out all possible sources in the FOV of interest.

- Categorize the sources into transient and persistent sources.

- If a source is transient, identify if an outburst is reported for the period of interest using any other pointed or monitoring instrument.

- In case of persistent sources, verify if any pointed observation of the source exists for the particular duration of interest. Ideally, one would consider an instrument which has an overlap in operational energy range with the instrument in consideration. For example, since *SXT+LAXPC* operates in the energy range of $0.3 - 80$ keV, *INTEGRAL, NuSTAR* etc., can be viable candidates. Let X be one such source possibly present in the same FOV as the source of interest.

- If observations with other instruments around the same time do not exist, deduce the average flux, spectral and temporal properties of X from existing literature.

- If X exhibits any periodic signature, test for the same in the lightcurve obtained. Estimate the percentage of contribution from this signal to the source. As an approximation, if the contribution is more than 20% (an arbitrary limit based on the source flux and energy band in which it emits), the data is contaminated and cannot be used.

- In cases where contamination is less than 20%, generate the simulated spectrum of X. Subtract the spectrum of X along with the background from the total spectrum obtained. This subtracted spectrum can be considered free from contamination. The subtracted spectrum can be used for analysis or

for comparison with the original spectrum (source + X) on which spectral modelling is performed.

- As a final test, also check for variation of spectral parameters at different energy ranges. This is subject to the condition that imaging data exists, which is absolutely free from contamination. This is used as reference to determine the energy range to be used for spectral modelling.

The above gives a generalized summary of the steps performed to account for contamination. We now present the procedure followed for the specific case of 4U 1630-472 as detailed in Baby et al. (2020). 4U 1630-472 lies in a crowded region of the Galaxy (Rodriguez et al., 2003). The *SXT* image of the source for a single orbit from an observation on 4 August 2018 is shown in Figure 2.3. The persistent sources IGR J16320-4751 and IGR 16393-4643 are also marked in the figure. Multiple transient sources like MAXI J1631-479, IGR J16328-4726 etc., also exist in the FOV considered. However, no outbursts or flares were reported from any of those sources. Based on the flux levels determined earlier in those sources, it can be safely assumed that the transient sources in the FOV were in quiescence and did not contribute to the total flux. We then proceed to check for the contribution from persistent sources. As *SXT* onboard *AstroSat* is an imaging instrument, we first check visually for contribution from sources close to 4U 1630-472 in the energy range 0.3–8 keV. There are two persistent sources close to 4U 1630-472, namely, IGR J16320-4751 (=AX J1631.9-4752) and IGR J16393-4643, which could contaminate the *LAXPC* spectrum. IGR J16393-4643 lies at an angular separation of more than $1°$ from 4U 1630-472 and hence is excluded as a possible candidate for contamination. However, as IGR J16320-4751 lies $0.58°$ away from 4U 1630-472 (Rodriguez et al., 2006), it lies close to the edge of the *LAXPC* FOV at FWHM. The contribution could be more significant in the higher energy band as the FOV is quoted to be $1° \times 1°$ at E > 50 keV (Antia et al., 2017). Therefore, we adopt a two-way approach to deal with this issue. The first is using pulsation studies to confirm the detection of IGR J16320-4751 source, along with its relative strength. The second approach is to quantify the contribution from this source to the total source spectrum by generating simulated spectrum of IGR J16320-4751 using an off-axis response based on the previous studies of the source. IGR J16320-4751 is a hard, persistent pulsar source, emitting at a pulse period of $\sim 1310$ s (Rodriguez et al., 2006). We checked for existence of simultaneous observations of the source from various instruments. Although *INTEGRAL* observations exist during August 2016 for both sources, they could not be used for detailed spectral analysis as the observations were in slew mode.

*AstroSat* observations were performed for 5 days during the 2016 outburst and 10 days during the 2018 outburst. Details of the observations are presented in Chapter 3. These observations were divided into a total of 18 segments to study
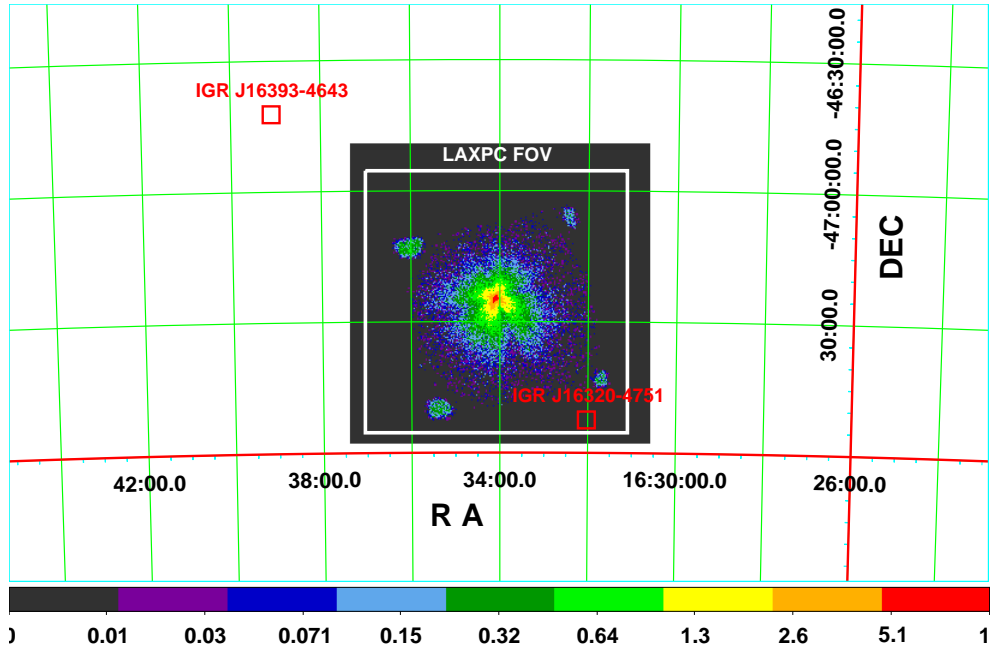
**Figure 2.3:** *SXT* image of the source 4U 1630-472 from Orbit 15415 (ObsID 2274). The persistent sources IGR J16320-4751 and IGR J16393-4643 are marked as red boxes. LAXPC FOV of $1° \times 1°$ is also marked as a white box for reference. 4U 1630-472 is seen at the centre of the FOV. The colour bar at the bottom shows the magnitude of intensity.

the spectral and temporal evolution during the outbursts. We check for the reported $\sim 1300$ s pulsation in the $3-80$ keV $LAXPC$ lightcurve for all the available observations of the source. This is used to obtain the pulse fraction from which the probable contribution of IGR J16320-4751 source is estimated. The $LAXPC$ lightcurves in $3-80$ keV energy band with a bin time of 1 s were used to generate the $\chi^2$ plot with respect to the period. `efsearch` tool of `Xronos` was used to find the pulsation of the source. The default epoch of the observation was set for searching the period of 1310 s (Rodriguez et al., 2006). The default phase bin per period was set to 10. Thus, it creates the bin time to 131 s. The resolution for period search was set to 1.5 s and the number of the search frequency was set to 32. These default parameters were used for searching the pulse period. We find the pulsation varying from $1293 \pm 1$ s for ObsID 0626 to $1327 \pm 5$ s for ObsID 2354. The period could not be constrained in ObsID 2372. Summary of the pulse period detected in all ObsIDs is presented in Table 2.2.

In order to estimate the contribution of IGR J16320-4751 in each observation of 4U 1630-472, we calculated the pulse profile for the period around 1300 s. A sample calculation is described here. The amplitude of pulsation in ObsID 2318 is 4 counts s$^{-1}$ and the detected period is around 1314.5 s, which is close to the

48

**Table 2.2:** Summary of detected pulse period along with typical contribution of IGR J16320-4751 for each observation of 2016 and 2018 outburst. The pulse fraction considered nominal value of 20% (Rodriguez et al., 2006) to estimate the contribution of IGR.

| Obs | ObsID | Exp. (ks) | Pulse Period (s) | Pulse Amplitude (c/s) | Typical contribution from IGR source (c/s) | IGR cts/Total cts (Contamination %) | Energy band used (keV) |
|---|---|---|---|---|---|---|---|
| | | | | 2016 | | | |
| 3 | 0626 | 10.4 | $1293 \pm 1$ | 6 | 15 | 15/144 (10.4) | $3 - 10$ |
| 4,5 | 0686 | 51 | $1299 \pm 5$ | 6 | 15 | 15/715 (2.1) | $3 - 13$ |
| 6,7 | 0698 | 41 | $1314 \pm 2$ | 8 | 20 | 20/715 (2.8) | $3 - 13$ |
| | | | | 2018 | | | |
| 8,9 | 2274 | 24 | $1316 \pm 4$ | 20 | 50 | 50/900 (5.6) | $3 - 13$ |
| 10 | 2282 | 10 | $1323 \pm 5$ | 40 | 100 | 100/880 (11.4) | $3 - 10$ |
| 11 | 2294 | 10 | $1299 \pm 3$ | 30 | 75 | 75/785 (9.6) | $3 - 10$ |
| 12 | 2298 | 9 | $1342 \pm 5$ | 30 | 75 | 75/770 (9.7) | $3 - 10$ |
| 13 | 2304 | 10 | $1316 \pm 4$ | 20 | 50 | 50/768 (6.8) | $3 - 13$ |
| 14,15 | 2318 | 80 | $1320 \pm 1$ | 4 | 10 | 10/704 (1.4) | $3 - 13$ |
| 16 | 2340 | 11 | $1316 \pm 5$ | 30 | 75 | 75/731 (10.3) | $3 - 10$ |
| 17 | 2354 | 11 | $1327 \pm 5$ | 20 | 125 | 125/954 (13.1) | $3 - 20$ |
| 18[e] | 2372 | 10 | - | - | - | - | $3 - 20$ |

[e] Unable to constrain period

**Table 2.3:** Results of spectral fits using phenomenological model to source spectrum after subtraction of IGR spectrum is presented here. Spectral parameters are close to those in Table 3.1 for corresponding observations. Similar variation in parameters is observed for all the observations.

| Obs (ObsID) | $N_H$ ($\times 10^{22}$ at/cm$^2$) | $\Gamma$ | $E_{line}$ (keV) | $T_{in}$ (keV) | Norm$_{disk}$ | $\chi^2_{red}$ $\chi^2$/dof |
|---|---|---|---|---|---|---|
| 14 2318 | $8.1^{+0.1}_{-0.1}$ | $2.9^{+0.1}_{-0.2}$ | - | $1.27^{+0.01}_{-0.01}$ | $273^{+13}_{-13}$ | 1.24 (575/462) |
| 17 2354 | $8.03^{+0.05}_{-0.09}$ | $2.14^{+0.01}_{-0.01}$ | 6.8[l] | $1.27^{+0.01}_{-0.01}$ | $339^{+13}_{-13}$ | 1.04 (452/431) |

[l] Upper limit
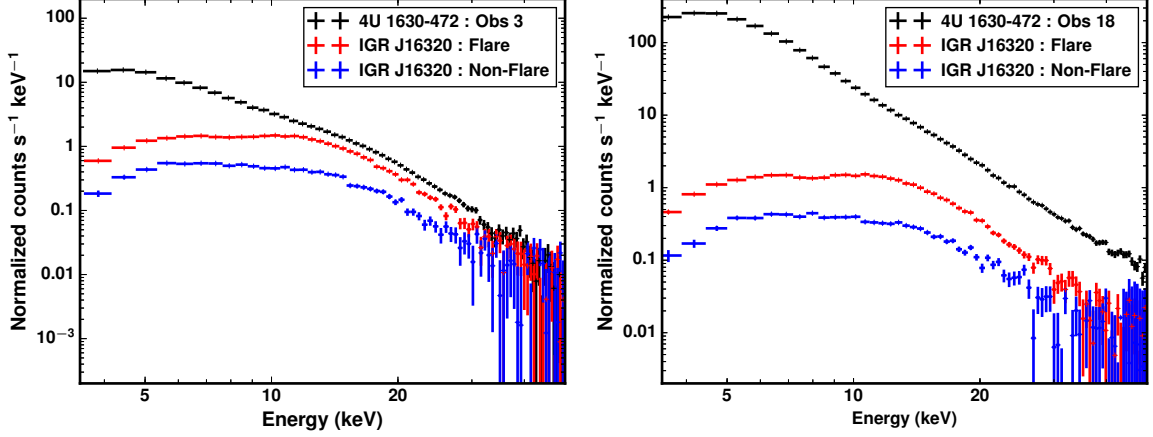
**Figure 2.4:** Simulated *LAXPC* spectra for IGR J16320-4751 source at an offset of 0.58° from the center using the off-axis response plotted for flaring and non-flaring cases (Rodriguez et al., 2006) along with the source spectrum obtained for 2016 August 27 and 2018 September 17. The model considered for obtaining the simulated spectrum is *wabs\*edge\*(highecut\*powerlaw)*. See text for details.

value found in the literature. The pulse fraction of this source is reported in the range of $18 – 26\%$ (Rodriguez et al., 2006). We adopt a nominal value of 20% to get the total expected counts. Considering the offset for this pulse amplitude and assuming a pulse fraction of 20%, this translates to about 10 counts $s^{-1}$, while the total count rate is about 700 counts $s^{-1}$ (see Table 2.2). This gives the contamination of 1/70, which is very small and can possibly be neglected. Table 2.2 gives the pulse period, pulse amplitude and typical contribution from IGR J16320-4751 source in each ObsID. The pulse amplitude is then used to obtain the relative contribution from IGR J16320-4751 source as a fraction of the total counts observed for that particular ObsID, which is represented as the contamination percentage. Following similar approach, we estimate the contribution of IGR 16320-4751 source for each observation which is presented in Table 2.2. Except for two observations at the beginning, pulsation studies proved beyond doubt that the spectrum was contaminated by IGR J16320-4751 source at varying levels in different observations.

The next step is to obtain the simulated spectrum for subtraction. Simulated spectrum of IGR J16320-4751 is generated using the *LAXPC* response for an offset of 0.5°, considering the unlikely flaring case with a 2–10 keV flux of $2.4 \times 10^{-10}$ ergs cm$^{-2}$ s$^{-1}$ (Rodriguez et al., 2006). The model used to generate the simulated spectrum is *wabs\*edge\*(highecut\*powerlaw)*. The count rates are compared and spectra, with contribution from the contaminating source less than 5%, is considered without further checks. We discard those observations where the contribution

from IGR J16320-4751 is more than 20%. For the rest of the observations, we subtract the simulated spectrum and the background to check for variation in spectral parameters with different energy bands. It was found that the spectral parameters remain unchanged upto 13 keV for cases where IGR J16320-4751 contribution is $\leq 10\%$ in comparison with the constant background subtracted spectra. We could consider energy spectra upto only 10 keV for cases where the contribution is more than 10%. For the last two ObsIDs, we could obtain good spectra upto 20 keV, considering the brightness of the source in the hard energy band (see Tables 2.2, 2.3). Table 2.2 gives a summary of contribution from the source and the energy bands considered. The parameters obtained for two sample cases in ObsID 2318 and 2354 are given in Table 2.3. Comparing with the parameters in Table 3.1, it can be seen that the spectral fits, with and without the subtraction of IGR J16320-4751 spectrum, are comparable. Based on these studies, the energy band considered for each ObsID is given in the last column of Table 2.2. Although 4U 1630-472 emitted mostly in the soft energy band, there was one instance in 2018, where a sudden rise in counts was seen in the $15 - 50$ keV energy range. This is seen in the *Swift/BAT* lightcurve (see Figure 3.1 in Chapter 3). In Figure 2.4, we present spectra of Obs 3 and Obs 18 in the left and right panels respectively. Obs 3 is a sample spectrum for when the source is in a relatively softer state. Higher contribution in the hard energy band is seen during Obs 18. We also plot the simulated spectra of IGR J16320-4751 in the flaring (red) and non-flaring (blue) case alongside the source spectra (black) for comparison. However, we consider the unfavourable flaring case in order to exclude any possibility of contamination from the IGR J16320-4751 source. It is clearly seen from Figure 2.4, that IGR J16320-4751 dominates above 13 keV when the source is softer (for e.g., Obs 3, left panel) and above 25 keV, when it is brighter in the hard energy band (for e.g., Obs 18, right panel). This further confirms that the energy band chosen for analysis using the previous method (pulsation studies) can be considered absolutely contamination free in the worst case scenario. It is also evident from *SXT* image, that $0.3 - 8$ keV energy range was free from contamination. Therefore, temporal analysis is performed only in $3 - 10$ keV energy range in all cases. A similar approach was used to account for contamination of IGR J17091-3624 data by the source GX 3-1. The details are presented in (Katoch et al., 2021).

# Chapter 3

# 4U 1630-472 : A 'mini' look at the 2016 and 2018 outbursts with *AstroSat*

From a general description of X-ray sources and BHBs in Chapter 1, we now move on to our specific sources of interest. After the first detection of Cyg X-1 (Bowyer et al., 1965), which was later reported as the first black hole candidate, a string of discoveries followed, some in a torrential flow, others in gentle trickles, of many more black hole candidates. Meanwhile, the presence of a black hole in Cyg X-1 was not definitively proven yet, which was even the subject of a friendly wager between Stephen Hawking and Kip Thorne in 1975, mentioned by Hawking himself in his book, *A Brief History of Time.* However, overwhelming scientific evidence resulted in Hawking losing the bet in 1990, and Cyg X-1 became the poster-source (?!) of BHBs. The addition of every new source in this category, resulted in further revelations on the nature and geometry of these systems. Classification of these sources into LMXBs, HMXBs, persistent, transient and so on followed, which are detailed in Chapter 1. A brief overview of various models that explain the observations are also outlined in Chapter 1. More than 50 years since the discovery of the first black hole candidate, these exotic objects still possess the ability to surprise and intrigue us, with seemingly unpredictable outburst patterns and non-conformity to the generally accepted picture. One such source, that has astronomers stumped with its outbursts of varying intensity and periods, and absence of certain states during its outburst evolution, is 4U 1630-472.

## 3.1   4U 1630-472 : A brief profile

The first mention of 4U 1630-472 (then 3U 1630-47) is found in Forman et al. (1976) as a newly discovered source, observed between 1970 and 1972. The $2-$

6 keV lightcurve from the *Uhuru* satellite between December 1970 and March 1972 revealed that the source is of transient nature and lies within 5° of the Galactic plane. Jones et al. (1976) analysed data from *Uhuru* and *Ariel V* between December 1970 and May 1976. Four transient outbursts were observed during this period, giving it the distinctive status of being the first source undergoing repeated outbursts. The regularly spaced outburst duration ($\sim 615$ days) was initially associated with the orbital period of the source and hence was postulated to be a binary system with a compact object in long-period, highly eccentric orbit. Each outburst lasted approximately for $100 - 150$ days. A fifth outburst was reported by Kaluzienski and Holt (1977); Share et al. (1978), which lasted for almost two years (Holt et al., 1978) and was the first reported 'super-outburst'.

The first attempt at spectral analysis was done by White and Marshall (1983), in which the spectra of 4U 1630-472, along with five other sources, was reported to be similar to that of Cyg X-1. Hence, it was categorized as a black hole candidate. After the declassification of the atmospheric data from *Vela 5B*, shortly after the Cold War, the lightcurve from the source showed that it was first captured in an outburst in 1969 (Priedhorsky, 1986). This source was previously classified as a quasi-persistent source as it was found to undergo an outburst once every two years (Kuulkers et al., 1997). The shorter outbursts were characterized by softer spectra and apparent lack of state transitions (see Parmar et al., 1986; Abe et al., 2005; Capitanio et al., 2015, and so on). Over the years, multiple studies have been done on this source, taking advantage of the recurrence times. Nevertheless, dynamical properties are difficult to estimate, as the source lies towards a crowded region of the Galaxy (Tomsick et al., 2005). It doesn't help that the interstellar absorption in the direction of the source is on the higher side with numbers ranging from $4 - 12 \times 10^{22}$ cm$^{-2}$ (Kuulkers et al., 1998; Tomsick et al., 1998). More recent high resolution X-ray grating spectroscopy with *Chandra* places this value at $10^{23}$ cm$^{-2}$ (Gatuzz et al., 2019). The generally accepted values of mass, inclination and distance are 10 M$_\odot$, 64° and $10 - 11$ kpc respectively (Tomsick et al., 1998; Augusteijn et al., 2001; Seifina et al., 2014; King et al., 2014, etc.). However, these are indirect estimates, heavily dependent on the physical interpretation of the models chosen. This leaves the actual numbers still enshrouded in mystery, only deepened by the unusual behaviour of the source. Newer and better instruments continue to point at this source as it appears religiously, once in $\sim 600$ days, as we continue to search for new clues about its nature.

In this chapter, we summarize one such study made of the 2016 and 2018 outbursts of 4U 1630-472 observed with *AstroSat*. We faced an additional hurdle in the form of contamination from IGR J16320-4751, a hard energy X-ray pulsar, lying 0.5° away from our unsuspecting quarry. It was necessary to quantify and isolate the contribution from the said source, so that our analysis could be error-free. This involved tracking down all the available information on the source IGR

J16320-4751 in the literature, looking for pulsation signatures in the obtained lightcurve, and quantifying the contribution from the pulsar in each observation. All this is detailed in Section 2.6 and will not be repeated here. However, mentions of this particular antagonist will crop up multiple times in this chapter while justifying the energy limits considered for spectral analysis. Here, we will focus on the estimation of the physical properties of 4U 1630-472 and attempt at untangling the origin of different types of outbursts. We refer to the long ($\sim$ 2 years) and short ($\sim$ 150 days) outbursts as 'super' and 'mini' outbursts respectively, for ease in discussion.

## 3.2   Data assimilation - Obtaining the final products

Before September 2015, when *AstroSat* was launched, the last outburst of the source 4U 1630-472, as seen by *MAXI*, started in January 2015. That placed the next outburst roughly towards the end of August 2016. Right on cue, the source went into outburst on 27 August 2016. *AstroSat* was already scheduled to look at the source under Guaranteed Time (GT) observations on the very same day. The next observation of the source was on 28 September 2016, also under GT. Later, Target of Opportunity (ToO) observations were conducted on 1 & 2 October. The source underwent an outburst again in 2018, which was first reported by Mao et al. (2018) in June 2018. This time, it was observed for a period of 9 days from 4 August – 17 September 2018, as part of *AstroSat's* ToO campaign. Continuous monitoring was only available with *MAXI*, while *Swift/BAT* observed the source for almost the entire duration of the outburst, except for a few days when observations were not possible due to a technical complication.

### 3.2.1   *MAXI* and *Swift/BAT*

Since continuous observations with pointed instruments are unavailable for the source during the 2016 and 2018 outbursts, we rely heavily on the lightcurves and HID obtained using *MAXI* and *Swift/BAT*, to track the evolution of the source.

*MAXI* one-day averaged lightcurves are obtained in the $2-4$, $4-10$, $10-20$ and $2-20$ keV energy bands to obtain the lightcurves and hardness ratios from MJD 57572 and MJD 58450. Light curves in the energy range $2-6$ keV and $6-20$ keV are used to obtain the hardness ratio to plot the HID, to facilitate comparison with other sources. There is one instance where a significant rise in the flux in the hard energy band ($10-20$ keV) is seen during the 2018 outbursts. Therefore, we also obtain the one-day averaged lightcurve with *Swift/BAT* in $15-50$ keV energy band. Also, keeping in mind that the sources close to 4U 1630-472 in the crowded FOV were mostly known to be emitters in the hard energy band, lightcurves from *Swift/BAT*, prove vital in quantifying the contribution from nearby sources, if
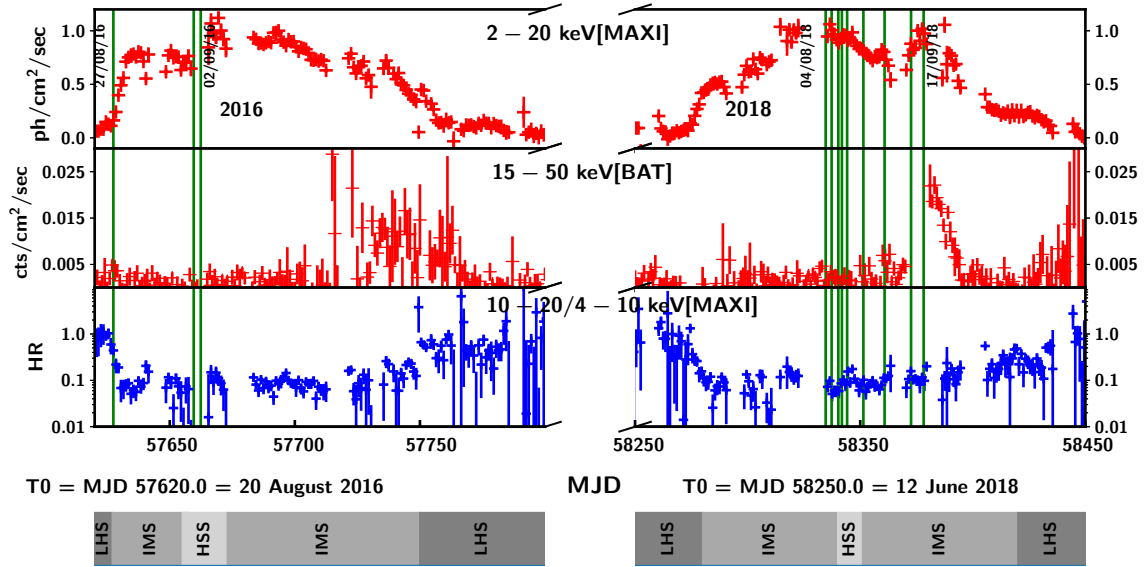
**Figure 3.1:** Lightcurve from *MAXI* in the $2-20$ keV band is plotted in the top panel along with the *Swift/BAT* lightcurve in the $15-50$ keV range in the second panel. *AstroSat* observations are marked as vertical green lines. The colour bar at the bottom indicates different spectral states. This is elaborated in Section 3.5.

any. Figure 3.1 shows the *MAXI* lightcurve of the source in the $2-20$ keV energy band, *Swift/BAT* lightcurve in the $15-50$ keV energy band and the hardness ratio obtained using *MAXI* lightcurves in the $10-20$ keV and $4-10$ keV energy band in panels 1, 2 and 3 respectively. The hardness ratio (HR) is defined as the ratio of flux in $10-20$ keV band to the flux in $4-10$ keV band. The green vertical lines represent the dates of *AstroSat* observations.

### 3.2.2 *AstroSat*

A description of India's first multi-wavelength observatory *AstroSat* is provided in Chapter 2. While there are five instruments onboard *AstroSat*, *SXT* and *LAXPC* are used to observe the source in the X-ray energy band $0.3-80$ keV. In the following sections, we briefly describe the data obtained and the reduction process followed.

### *SXT*

PC mode data was used for all the observations except for $1-2$ October 2016, where FW mode data was used to avoid pile-up issue in anticipation of higher count rate in the soft energy band, as the source was expected to be in the soft state. Details of data reduction are provided in Chapter 2. The Level-1 imaging

data is processed off-line through a pipeline software to obtain Level-2 cleaned event files for each individual orbit.
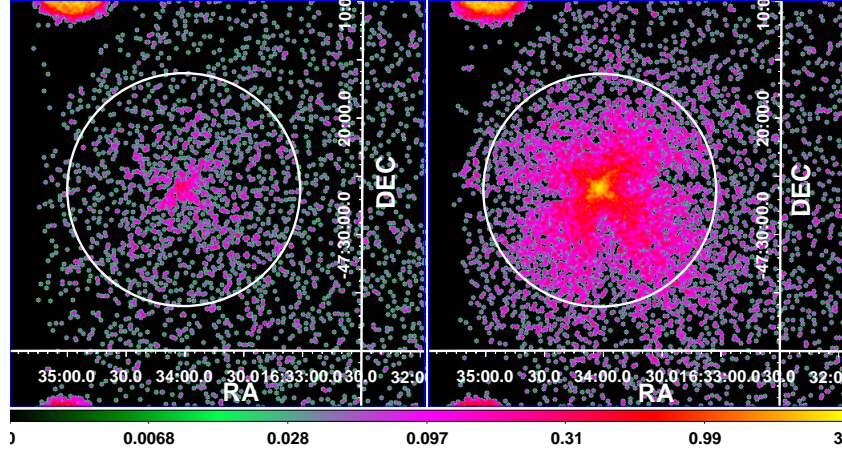


**Figure 3.2:** Source region within radius of 10 arcmin is considered for extraction of spectrum for *SXT*. The left image corresponds to Obs 1, where the source is very faint at the beginning of the 2016 outburst. The right image corresponds to Obs 3, which is taken $\sim$ 11 hours apart. It is clear that the source has considerably brightened in this duration. As no pile-up effects were observed, the exclusion of central 1 arcmin region was not performed (see text for details). The colour map at the bottom shows the source intensity for *SXT* in counts pixel$^{-1}$.

XSELECT V2.4d was used in HEASOFT 6.21 to extract light curve and spectra using the cleaned event files. We first considered a 16 arc min source region as suggested for PC mode data[1]. As the count rate was < 40 c/s, pile up effects were not observed and hence exclusion of 1 arcmin central source region was unnecessary. We merged the data from a few orbits in which the count rate and hardness ratios did not vary appreciably, to generate the event file using the sxtevtmerger script. As considerable variation in flux and hardness ratios was observed on the first day of observation (27 August 2016), three data groups are obtained from a single observation, separated from the first group by $\sim$ 6 hrs and $\sim$ 11 hrs respectively. We refer to these three data sets as Obs 1 (MJD 57627.05), Obs 2 (MJD 57627.47) and Obs 3 (MJD 57627.69) (see Table 3.1). The criteria for data selection was a minimum exposure time of 1 ks in $SXT$ and the source count rate to be at least a factor of 2 greater than the blank sky background. Only observations which are strictly simultaneous with $LAXPC$ observations are chosen. We obtain a total count rate of $\sim$ 0.3 c/s considering a 16 arcmin source radius for Obs 1. As the source contribution beyond the 10 arcmin radius was < 30%, we use a 10 arcmin region centred around the source as the optimum case with count rate of $\sim$ 0.23 c/s. The count rate increased to 1.6 c/s for Obs 3.

---

[1] www.tifr.res.in/~astrosat_sxt/dataanalysis.html

The *SXT* image for Obs 1 and 3 are shown in Figure 3.2 along with the chosen source region. It clearly shows that the source brightened by a factor $> 10$ within this duration. For $1-2$ October 2016 FW mode data, 3 arcmin source region is considered, encompassing more than 70% contribution from the source. A circular source region with 10 arcmin radius was considered for all other observations. The response file provided by the *SXT* team for PC mode and FW modes are used[2], wherever applicable. Appropriate *arf* files provided by the *SXT* team are used, where the source was at the centre of the Field of View (FOV). In cases where an offset was observed, `sxtmkarf` script is used to generate the ancillary response file. Blank Sky observations are used to generate the background spectrum. *SXT* spectra are binned with a grouping of 20 counts per bin for better statistics.

### *LAXPC*

*LAXPC* data is obtained in Event Analysis mode, which is analysed using *LAXPC* software[3]. We use only *LAXPC20* for the timing and spectral analysis, as *LAXPC30* was off and *LAXPC10* was operating at a low gain during the time of the 2018 observations. Individual orbits are merged together to satisfy the selection criteria of time $> 4$ ks for *LAXPC* data, where the count rates and hardness ratios remain stable. From the 2016 and 2018 outburst data, 7 and 11 data sets are chosen respectively (see Table 3.1). As mentioned earlier, 4U 1630-47 lies in a crowded FOV and contamination in the *LAXPC* data could not be ruled out. This is described in detail in Section 2.6. Therefore, *LAXPC* data could not be used in some cases or had to be restricted to certain energy range, based on the level of contamination. We use `laxpcsoftv2.5` released on 6 August 2018, to obtain the lightcurve and energy spectra. We follow Misra et al. (2017); Sreehari et al. (2018) and the instructions provided with the *LAXPC* data reduction software. We consider only the top layer of the detector and discard multiple detections of a single event to obtain the spectrum. Details of the response and background generation are found in Antia et al. (2017). Background is generated with the gain shift applied to align the background spectra with the source spectra using the `backshiftv2.e` code. Background model closest to the observation dates are chosen. However, four different backgrounds are provided for the month of August 2018 due to variation in background rate, corresponding to August 2, 8, 12 and 15. The background from 15 August 2018 is chosen for all the observations. The details of the observation IDs and exposure times of the observations are presented in Table 3.1. The observations are divided into a total of 18 segments to study the spectral and temporal evolution during the outbursts. Analysis and modelling procedure of *SXT* and *LAXPC* spectra is elaborated in Section 3.3.

---

[2] http://astrosat-ssc.iucaa.in

[3] http://www.tifr.res.in/~astrosat_laxpc/LaxpcSoft.html

### 3.3 Attempting a physical interpretation of the data

#### 3.3.1 Spectral Analysis

Evolution of spectral parameters with time during both outbursts can take us closer to understanding the physical properties of the source. Following general convention, we first attempt to model the spectra using phenomenological models and then, if possible, graduate to more physical models. However, as detailed in Section 2.6, we had to limit our spectral analysis to different energy ranges based on the level of contamination from IGR J16320-4751. The spectral analysis was performed using XSPEC version 12.9.1.

The combined spectra of *SXT* and *LAXPC* are modelled in three different energy bands for different ObsIDs i.e., $0.7 - 10$ keV, $0.7 - 13$ keV and $0.7 - 20$, keV based on the pulsation studies and estimates of relative contribution from IGR J16320-4751 source (see Table 2.2 and Table 3.1). The *gain* command is used to modify the *SXT* response file linearly. The slope is fixed to 1 and the offset is allowed to vary. Unfortunately for Obs 1 & 2, only *SXT* spectra could be used, as the source is very faint and the contribution from IGR J16320-4751 is more than 50% in *LAXPC* spectra. The spectra are modelled using *phabs* × *powerlaw* model. No additional disc component is required, implying that the source is in hard state. The unfolded spectra for four observations, two each from 2016 and 2018 outbursts, are shown in Figure 3.3. The black and red crosses denote *SXT* and *LAXPC* spectra respectively.

The $N_H$ value is obtained at $7.5 \times 10^{22}$ atoms cm$^{-2}$ with a photon index of 1.82 and $\chi^2_{\mathrm{red}}$ of $32.1/27 = 1.2$. The photon index increased to 1.91 for Obs 2. A disc component is required for Obs 3 with photon index increasing to 2.03. For the rest of the 2016 observations and all observations of 2018, we use an absorbed multicolour disc component (*diskbb*) (Mitsuda et al., 1984; Makishima et al., 1986), a powerlaw component (*powerlaw*) and a *gaussian* to fit the spectra. Powerlaw component is not required in the observations where spectrum was considered only upto 10 keV, due to prominence of disc. The $N_H$ is obtained at $(7.3 - 8.13)$ $\times 10^{22}$ atoms cm$^{-2}$. An edge is required at 2.44 keV for Sulphur[4] in addition to the gain applied for *SXT* data. A systematic error of 1.5% is applied to each bin in the combined fit. A normalization constant is added to account for the difference in calibration of the instruments. The centroid energy of the *gaussian* is restricted to be in the range $6.2 - 6.9$ keV, wherever the component is required. The fit values obtained from this model are given in Table 3.1. All the errors are quoted at 68% confidence, unless stated otherwise.

---

[4]http://www.iucaa.in/~astrosat/kps_a01_sxt.pdf
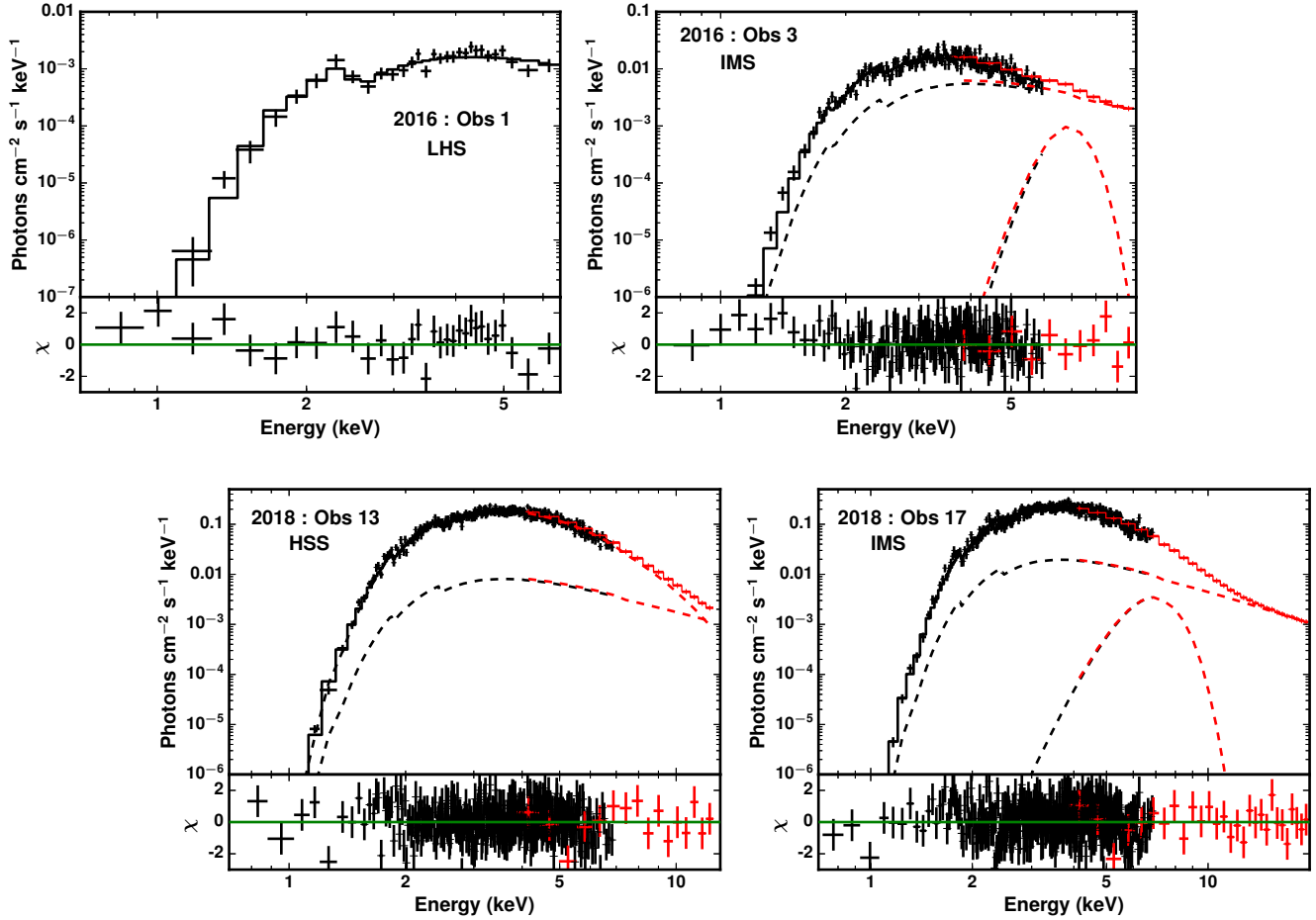
**Figure 3.3:** The top panel shows fit with phenomenological model to *AstroSat* data of 2016 outburst. The left panel is a fit only to the *SXT* data as there was contamination in the *LAXPC* data. The bottom panels show fits to the 2018 outburst data.

### 3.3.2 Timing Analysis

Lightcurves of 1 s bin are obtained in the $3-10$ keV range using *LAXPC20* initially, for all observations considered in Table 3.1. For these combined orbits, we generate 0.005 s resolution lightcurves and corresponding backgrounds. The background varies between $\sim 6-10$ counts s$^{-1}$ during the observations. This background is subtracted from the lightcurve to generate the final lightcurve. We divide the lightcurve into 16384 time bins and create power spectra for each of the intervals. Then the power spectra are averaged to generate the final PDS. We rebin the power spectra geometrically by a factor of 1.05 in the frequency space. Dead time corrected Poisson noise level was obtained following the procedure in

Agrawal et al. (2018); Sreehari et al. (2019) using the relation and values given in Zhang et al. (1995) and Yadav et al. (2016). This dead time corrected Poisson noise subtraction is applied to all the PDS, which are normalized to give fractional rms spectra (in units of $(\text{rms/mean})^2/\text{Hz}$)). No contribution was seen in the PDS beyond 10 Hz in all the observations.
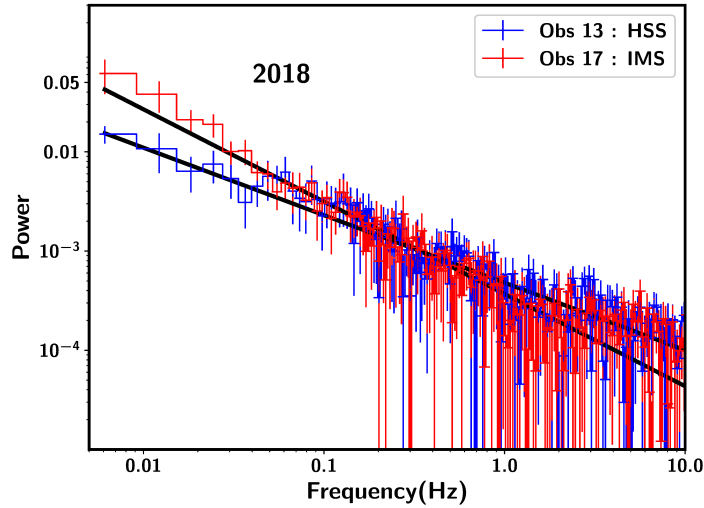


**Figure 3.4:** PDS in the energy range $3 - 10$ keV from 2 different days of 2018 outburst from frequency $0.005 - 10$ Hz is plotted in the figure on the left. Both are fit with a powerlaw model with Obs 17 PDS having a higher index.

All the PDS are modelled with a power law in the range 0.005 to 10 Hz (see Figure 3.4). Red noise is dominant in the PDS with no significant power above $\sim$ 1 Hz. No QPOs are observed. During the 2016 observations, the source count is too low in the initial observations, resulting in noisy PDS, making it difficult to check for the presence of QPOs. Total rms values are obtained in the frequency range $0.005 - 10$ Hz. The outburst profile and HID of the outbursts, along with spectral and temporal properties of the source, are presented in following sections.

## 3.4 Evolution of spectral and temporal properties

### 3.4.1 Spectral Properties

As discussed in Section 3.3, we fit the broadband spectra with phenomenological models. This is where we first try to identify different states using the spectral parameters. Figure 3.3 shows broadband spectra from two different observations each, from 2016 and 2018 outbursts. The top left spectrum shows the fit to Obs

1. No disc component is required, indicating that the source is in a 'canonical' hard state. The rise in HR values at the beginning of 2016 outburst, seen in panel 3 of Figure 3.1, also implies that the source was possibly in a hard state at the time of Obs 1. For Obs 3, separated by 11 hrs, the disc component is required to obtain a good fit ($\chi^2_{red}$ = 1.09) with a disc temperature of 0.79 keV and a normalization of $\sim$ 179 (see Table 3.1 and top right spectrum in Figure 3.3). Photon index ($\Gamma$) increases from 1.8 to 2.0 during the first 3 observations of 2016, after which the disc becomes more prominent. The disc temperature increases from 0.79 keV to 1.36 keV, accompanied by rise in photon index, signalling the transition from hard to soft state. For the 2018 outburst, the disc temperature is in the range 1.25 – 1.38 keV with powerlaw index reducing from 2.8 to 2.09 in the last three observations. Here, the source seems to have transitioned to a brighter Intermediate State (IMS), corresponding to the rise seen in $BAT$ lightcurve (see panel 2 of Figure 3.1 and bottom spectra in Figure 3.3). All the $N_H$ values lie in the accepted range (7–8.5)$\times 10^{22}$ atoms cm$^{-2}$.

**Table 3.1:** Fit parameters using the model *phabs* × *(diskbb+gaussian+powerlaw)*. The errors are quoted with 68% confidence.

| Date (ObsID) | Obs | MJD | Eff. Exp. (ks) SXT | LAXPC | $N_H$ ($\times 10^{22}$ at./cm$^2$) | $\Gamma$ | $E_{line}$ (keV) | $T_{in}$ (keV) | Norm$_{disk}$ | Flux$_{0.7-20.0}$ ($\times 10^{-8}$ ergs cm$^{-2}$ s$^{-1}$) | $\chi^2_{red}$ ($\chi^2$/dof) |
|---|---|---|---|---|---|---|---|---|---|---|---|
| | | | | | **2016** | | | | | | |
| Aug 27 (0626) | 1 | 57627.05 | 3.8 | - | $7^{+2}_{-1}$ | $1.8^{+0.7}_{-0.6}$ | - | - | - | $0.030 \pm 0.003$ | 1.2 (32.1/27) |
| | 2 | 57627.47 | 5.3 | - | $7.3^{+0.5}_{-0.6}$ | $1.9^{+0.1}_{-0.2}$ | - | - | - | $0.081 \pm 0.001$ | 1.24 (145/116) |
| | 3 | 57627.69 | 3.8 | 10.4 | $8.5^{+0.2}_{-0.2}$ | $2.0^{+0.1}_{-0.2}$ | $6.8^l$ | $0.79^{+0.03}_{-0.01}$ | $179^{+39}_{-16}$ | $0.27 \pm 0.01$ | 1.07 (192/179) |
| Sep 28 (0686) | 4 | 57659.04 | 5.1 | 9.6 | $7.2^{+0.1}_{-0.1}$ | $2.25^{+0.02}_{-0.03}$ | $6.3^l$ | $1.36^{+0.01}_{-0.01}$ | $222^{+10}_{-9}$ | $1.79 \pm 0.01$ | 1.20 (447/372) |
| Sep 29 (0686) | 5 | 57660.14 | 1.0 | 9.1 | $7.5^{+0.2}_{-0.2}$ | $2.65^{+0.02}_{-0.02}$ | $6.8^l$ | $1.32^{+0.01}_{-0.01}$ | $206^{+16}_{-14}$ | $1.55 \pm 0.02$ | 1.16 (392/338) |
| Oct 1 (0698) | 6 | 57662.40 | 2.5 | 5.6 | $7.9^{+0.2}_{-0.1}$ | $2.44^{+0.01}_{-0.01}$ | $6.2^l$ | $1.35^{+0.01}_{-0.01}$ | $227^{+16}_{-12}$ | $1.54 \pm 0.02$ | 1.32 (519/391) |
| Oct 2 (0698) | 7 | 57663.03 | 1.9 | 9.8 | $7.8^{+0.1}_{-0.2}$ | $2.38^{+0.03}_{-0.03}$ | $6.2^l$ | $1.36^{+0.01}_{-0.01}$ | $235^{+16}_{-17}$ | $1.62 \pm 0.01$ | 1.20 (401/335) |
| | | | | | **2018** | | | | | | |
| Aug 4 (2274) | 8 | 58334.55 | 1.9 | 4.2 | $7.9^{+0.1}_{-0.2}$ | $2.19^{+0.01}_{-0.01}$ | - | $1.29^{+0.01}_{-0.01}$ | $296^{+6}_{-18}$ | $1.74 \pm 0.01$ | 1.2 (541/444) |
| | 9 | 58334.75 | 2.6 | 9.4 | $7.9^{+0.1}_{-0.1}$ | $2.25^{+0.01}_{-0.01}$ | - | $1.30^{+0.004}_{-0.003}$ | $291^{+7}_{-8}$ | $1.79 \pm 0.02$ | 1.2 (549/467) |
| Aug 7 (2282) | 10 | 58337.29 | 1.5 | 6.1 | $7.5^{+0.1}_{-0.1}$ | - | - | $1.38^{+0.01}_{-0.01}$ | $224^{+8}_{-7}$ | $1.58 \pm 0.02$ | 1.2 (509/422) |
| Aug 10 (2294) | 11 | 58340.27 | 1.3 | 6.5 | $7.8^{+0.1}_{-0.2}$ | - | - | $1.33^{+0.01}_{-0.003}$ | $256^{+6}_{-12}$ | $1.56 \pm 0.02$ | 1.1 (446/391) |
| Aug 11 (2298) | 12 | 58341.86 | 2.8 | 8.1 | $7.7^{+0.1}_{-0.1}$ | - | - | $1.34^{+0.0}_{-0.0}$ | $244^{+4}_{-8}$ | $1.48 \pm 0.01$ | 1.2 (597/473) |
| Aug 14 (2304) | 13 | 58344.18 | 1.2 | 9.5 | $7.8^{+0.1}_{-0.2}$ | $2.22^{+0.02}_{-0.01}$ | - | $1.26^{+0.01}_{-0.01}$ | $306^{+13}_{-18}$ | $1.58 \pm 0.02$ | 0.98 (370/376) |
| Aug 20 (2318) | 14 | 58350.86 | 2.5 | 7.5 | $8.08^{+0.02}_{-0.05}$ | $2.79^{+0.01}_{-0.01}$ | - | $1.26^{+0.01}_{-0.01}$ | $282^{+6}_{-3}$ | $1.49 \pm 0.02$ | 1.2 (567/462) |
| Aug 21 (2318) | 15 | 58351.94 | 1.3 | 7.2 | $7.7^{+0.1}_{-0.1}$ | $2.11^{+0.02}_{-0.01}$ | - | $1.25^{+0.01}_{-0.01}$ | $300^{+8}_{-8}$ | $1.54 \pm 0.01$ | 1.05 (405/384) |
| Aug 30 (2340) | 16 | 58360.81 | 2.4 | 7.3 | $7.5^{+0.1}_{-0.1}$ | - | - | $1.35^{+0.01}_{-0.01}$ | $217^{+7}_{-9}$ | $1.37 \pm 0.02$ | 1.3 (623/451) |
| Sep 11 (2354) | 17 | 58372.57 | 1.0 | 6.6 | $8.1^{+0.1}_{-0.1}$ | $2.16^{+0.04}_{-0.02}$ | $6.8^l$ | $1.26^{+0.01}_{-0.01}$ | $355^{+22}_{-13}$ | $2.11 \pm 0.02$ | 1.04 (448/431) |
| Sep 17 (2372) | 18 | 58378.16 | 1.2 | 6.4 | $7.7^{+0.1}_{-0.1}$ | $2.09^{+0.01}_{-0.01}$ | $6.8^l$ | $1.28^{+0.01}_{-0.02}$ | $314^{+40}_{-13}$ | $2.28 \pm 0.03$ | 1.26 (523/414) |

[l] Parameter pegged at bounds

### 3.4.2 Temporal Properties

All the PDS are well modelled by a powerlaw ($AE^{-\beta}$), where A is the normalization and $\beta$ is the index of the power law. No additional component is required. No QPOs are observed during the *AstroSat* campaign of both outbursts. Figure 3.4 shows the PDS in the rms space obtained for HSS and IMS of 2018 outburst, modelled with a powerlaw, for representation. Evolution of the PDS is clearly seen with rms increasing from HSS to intermediate states (Figure 3.4). Variation of rms with flux is plotted in Figure 3.5. Although the *LAXPC* data for Obs 2 is discarded due to possible contamination by the nearby IGR J13620-4751 source (see Section 2.6), the rms value for this particular observation is presented for the sake of continuity. However, the number quoted is only for reference and should be treated as such. This is denoted by the unfilled blue star in Figure 3.5. The rest of the observations of 2016 are marked as filled blue stars. The rms
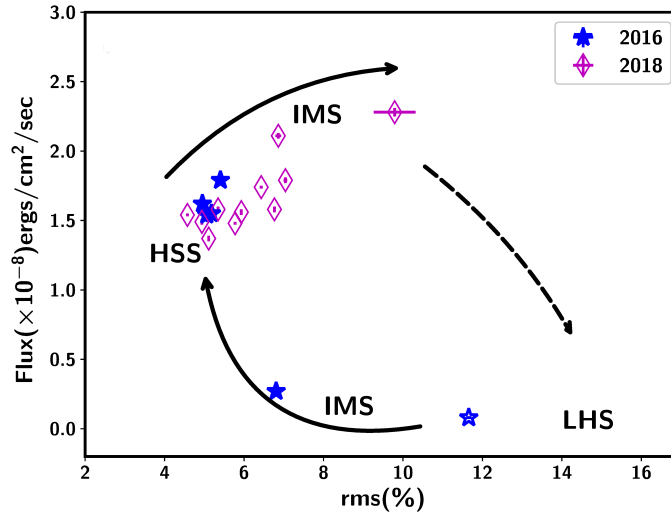


**Figure 3.5:** The variation in rms with flux is shown above. The filled blue stars and open magenta diamonds represent 2016 and 2018 outburst data respectively. The open blue star represents Obs 2, for which spectral analysis is not performed using *LAXPC* (see text). The evolution of the source with time is marked with arrows. The final probable transition from IMS to LHS is marked using a dashed arrow.

decreases from 11.6% in Obs 2 and 7% in Obs 3 of 2016 outburst to 4.9% in the later observations, as the source moves to HSS. Total rms decreases from 7% to 4.9% as the source moves from IMS to HSS during the 2018 outburst, shown as open magenta diamonds. An increase in rms is again observed during the decay, from 5.1% to 9.8%. In Figure 3.5, we mark the probable transition of the source between states during the outbursts. The evolution of rms across different states is

discussed in detail in later sections. Solid arrows show the evolution of the source during outburst. Wherever observations are not available, we extrapolate the rms values based on the observed trend and previously obtained values for other outbursts (Dieters et al., 2000; Trudolyubov et al., 2001). This is represented by the dotted arrow in Figure 3.5.

## 3.5 Super outbursts and 'mini' outbursts - finding the common ground

To get a comprehensive picture of the 'mini'-outbursts of 4U 1630-472, we analyse its lightcurve in different energy bands using *MAXI* and *Swift/BAT*. The *MAXI* lightcurve $(2-20$ keV$)$ of the 2016 and 2018 outbursts of the source is shown in the top panel of Figure 3.1. The 2016 outburst was first detected on 27 August 2016 and the source was active for $\sim 100$ days before going into quiescence. After $\sim 600$ days of inactivity, the source again went into outburst on 4 June 2018 which lasted for $\sim 150$ days. Both 2016 and 2018 outbursts show similar profiles.

The flux variation observed with *Swift/BAT* during both outbursts is shown in panel 2 of Figure 3.1. The source was very faint at the beginning of the outburst, but the indication of a sudden rise in *Swift/BAT* counts is seen in the decay phase of the outburst. This increase is more pronounced in the 2018 outburst than the 2016 outburst, which also precedes the secondary peak observed during the 2018 outburst. The flux increased $\sim 4$ times in one day from MJD 58360 to MJD 58361. Observations are not available for the 2018 outburst between MJD 58370 and MJD 58381 due to some technical snag in *Swift/BAT* (private communication with *Swift/BAT* team). Panel 3 of Figure 3.1 shows the hardness ratio variation with time. At the beginning of the 2016 outburst, the HR values are closer to $\sim 1.0$, and reduce in a short time to $\sim 0.2$, showing a quick transition from hard to an intermediate state. Then the source goes into the HSS as shown in the colour bar at the bottom of Figure 3.1. The source then gradually decays to the LHS with an increase in HR values, through a relatively longer intermediate state. Similar trend is followed in the 2018 outburst, with a longer rise time than in the 2016 outburst. The source seems to evolve from hard to soft state through an intermediate state during the rise. The source stays in the HSS for a few days. There is a rise in hardness ratios from $\sim 0.06$ to $\sim 0.1$, accompanied by the onset of a secondary outburst, where the source is in the intermediate state. Finally, the source goes into the LHS with a decrease in flux and increase in hardness ratios.

The HID of both outbursts is studied further to confirm the state transitions as inferred from Figure 3.1. In Figure 3.6, HID obtained with *MAXI* for 2016 and 2018 outbursts is shown. Note that a different definition of hardness ratio is used to generate the HID from the one used in Figure 3.1. While the third panel in Figure 3.1 was used as a marker for state transition, the HID obtained here is solely used to track the evolution of the source during the outburst. Due to
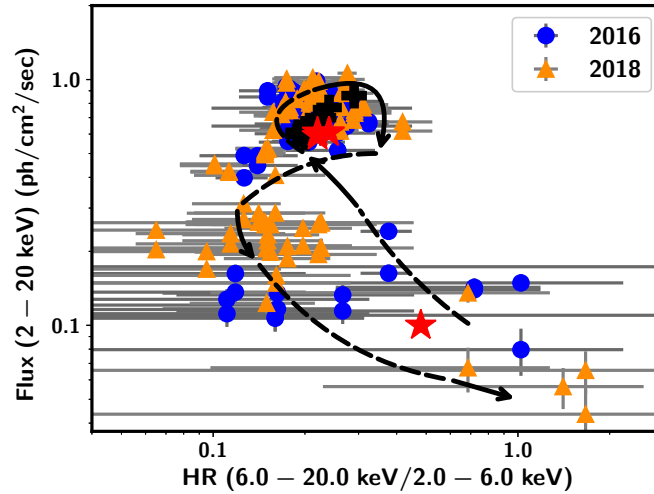
**Figure 3.6:** HID obtained using *MAXI* is plotted above. The blue circles and orange triangles correspond to the 2016 and 2018 outbursts respectively. The error bars are represented in grey. The red stars and black filled crosses are *AstroSat* data obtained during the 2016 and 2018 outbursts respectively obtained using model flux. Red star at the bottom corresponds to Obs 3. The direction of evolution is shown using the arrows.

larger uncertainties in the flux in $2 - 4$ keV band in *MAXI* data for 2016, negative flux is reported in some cases, resulting in loss of data points during the initial phase of the 2016 outburst. Therefore, harder energy bands are used for better representation in panel 3 of Figure 3.1. To track the evolution of the source in the HID, we include lower energy bands at the cost of loss of some data points. The observations where negative fluxes are reported in either of the energy bands ($2 - 6$ keV and $6 - 20$ keV) are discarded. The blue circles and orange triangles represent the *MAXI* data during the 2016 and 2018 outbursts respectively. The uncertainties are represented in grey. Data points obtained using *AstroSat* are superimposed on it as the red stars and black filled crosses for the 2016 and 2018 outbursts respectively. The hardness ratio decreases from $\sim 0.6$ to $\sim 0.2$ during the rise of the 2016 outburst along with an increase in luminosity. The red star is the first day of *AstroSat* observation of the source on 27 August 2016 corresponding to Obs 3, when it is in a harder state. As the outburst progresses, there is a quick transition to the HSS, accompanied by an increase in luminosity. This quick change in the HR values can also be seen in panel 3 of Figure 3.1 for the 2016 outburst. There is a hint of further increase in luminosity along with an increase in hardness ratios, suggesting a sudden transition into an intermediate state. The source then reaches the LHS through the path indicated by the arrows ending at a lower flux than that at the beginning of the outburst. Similar trend

65

is seen for the 2018 outburst represented by orange triangles.

The HIDs do not follow the typical 'q'-profile observed for Low mass BH XRBs as is already observed in previous outbursts of this source (Abe et al., 2005; Capitanio et al., 2015), rather, a distorted 'c'-shaped profile as traced out in Figure 3.6. The source exists in the LHS at the bottom of the 'c', while the HSS is almost exclusively found at the top end. However, IMS seems to exist everywhere except the lower end of the HIDs. Both outbursts seem to follow a similar profile, except for a smaller secondary peak seen in the 2018 outburst, before the source decays into quiescence (see Figure 3.1). During 2016 outburst, the source undergoes a quick transition from hard to soft state through an intermediate state. The IMS of decay phase is longer than that in the rising phase. The source begins at the lower right of the HID in the LHS and moves to the upper left towards HSS. Slight variation in flux and hardness ratio is seen, hinting at a transition to an intermediate state. This is represented by the circular head in Figure 3.6. Then it moves back to the lower part of the plot completing an elongated 'c'. The source follows the path traced out by the dotted lines in Figure 3.6 during the 2018 outburst too. However, the soft state in the 2018 outburst has slightly higher HR values in comparison with the 2016 outburst. Similar trend was seen during the 2010 outburst where a secondary peak was observed during the decay phase at similar flux (Capitanio et al., 2015). However, due to the large error bars seen in the HID, the path traced out in the upper right of the HID is difficult to discern clearly.

The data that we have is insufficient to decipher a clear picture of the evolution of the HID. Hence, the validity of the conclusions drawn may be questionable. One way to circumvent this problem, is to dig through the archives and obtain data from other instruments, which happened to observe the source continuously (with good spectral resolution) throughout one or more outbursts. The most obvious candidate is *RXTE*, which covered almost 8 outbursts from the source from 1996 to 2010. Hence, we use *RXTE/PCA* data obtained during the 1998 and 1999 outburst (see Figure 3.7, left panels) to further confirm the profile observed in the HID of both outbursts. We consider these two outbursts as an example for classical 'mini'-outburst (1999) and a short duration outburst with radio detection (1998).

The hardness ratio is defined as ratio of counts in $9-20$ keV band to the counts in $3-9$ keV band. This is plotted against the total counts in $3-20$ keV band in the left panels of Figure 3.7. The variation of the HR from 0.6 to $< 0.1$ takes place in a few days during the 1999 outburst, while the transition is more gradual in the 1998 outburst. This is also seen in the 2016 and 2018 outbursts where the transition from hard to soft state takes place very fast (see Figure 3.1). A circular head is seen in both HIDs (Figure 3.7), which could correspond to the intermediate region observed in 2016 and 2018 outbursts. Finally, the source goes

to the hard state through an intermediate state during the decay (see Figure 3.7). This is similar to what is observed by Capitanio et al. (2015) for the 2006, 2008 and 2010 outbursts. They reported that there is no evidence of an initial transition from a hard state to a soft state in the 2006 and 2008 outbursts. They suggest that the transition happened very quickly or has not occurred at all. However, the first *RXTE/PCA* observations of the source in 2006 and 2008 were carried out after $\sim 15$ days and 6 days respectively, after an increase in *ASM* flux was reported. We show here for the first time, that the hard to soft state transition occurs in a short time (within a few hours) and was probably not picked up for previous 'mini'-outbursts. *AstroSat* observed the source on the first day of the 2016 outburst itself, during which, a transition from hard to soft state occurred within a few hours (see Figure 3.1). It is clear from Figures 3.1 and 3.6, that transition between different states has taken place in both outbursts. Although the HID for 1998 outburst is harder and the circular head is much smaller in the HID, we propose that the evolution of the source during the outbursts of shorter duration follows the 'c'-shaped pattern as traced out in Figure 3.6.

Also, the transition from soft to hard state during the decay phase was seen to occur at slightly lower luminosities than the rising phase hard to soft state transition. Lower values of luminosity during soft to hard state transition was also observed during the decay of the 2010 outburst (Tomsick et al., 2014). This is further corroborated by the HID obtained using *RXTE/PCA* data for the 1998 and 1999 outbursts of this source (Figure 3.7).

**2002-2004 superoutburst**

1999

1998

I   II   III

1998
1999

MJD

HR (9-20/3-9 keV)

Counts/s (3-20 keV)

Counts/s (3-20 keV)
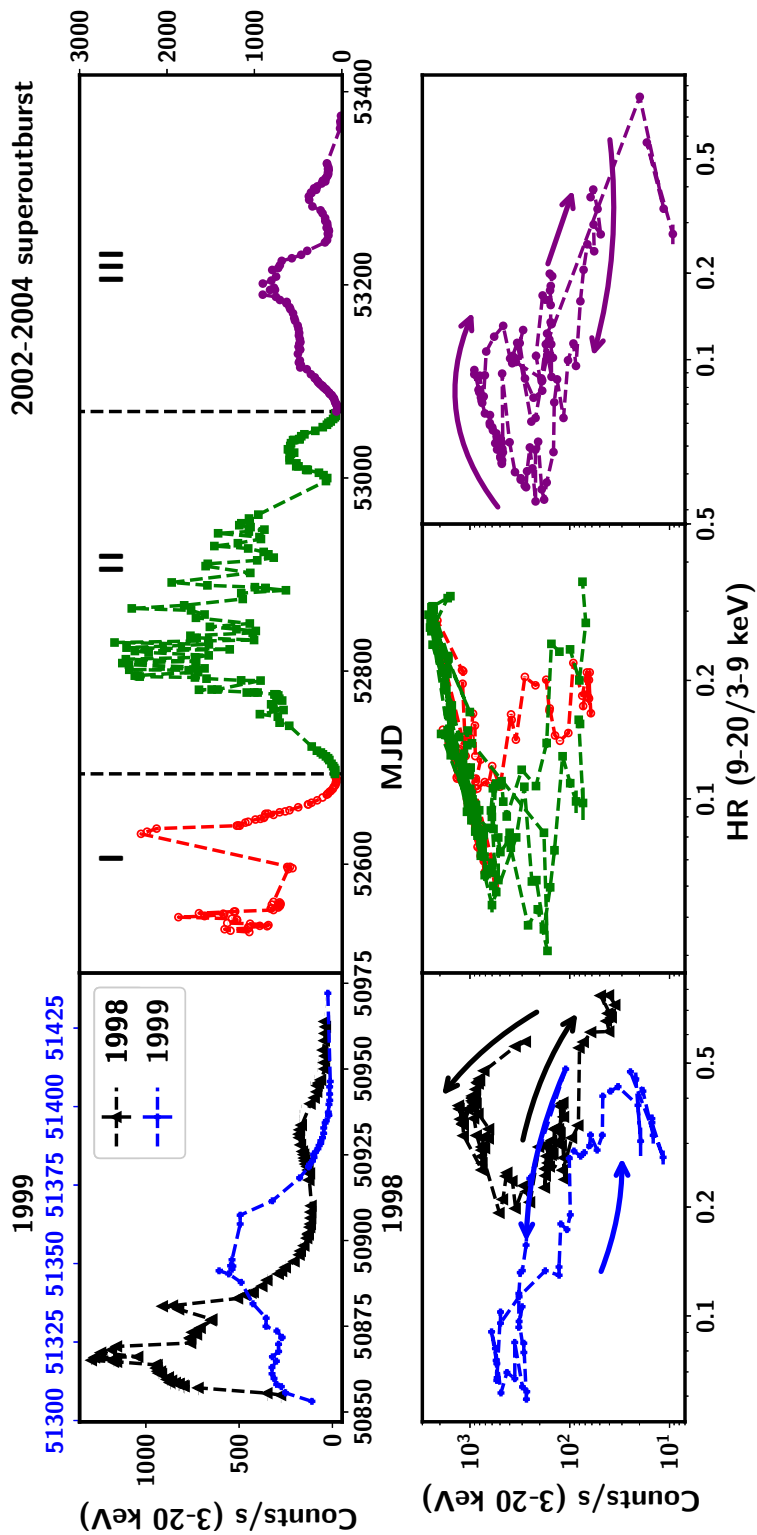
**Figure 3.7:** The top panels show the outburst profiles for 1998, 1999 and 2002-2004 outbursts. Corresponding HID with *RXTE/PCA* data is plotted in the bottom panels (obtained on request, for details see Tomsick et al. (2005)). The super-outburst is divided into 3 regions based on variation in flux and HR values. The circular head is present in the HID for 1998, 1999 outbursts and region III of 2002-2004 outburst although it is more defined in the 1999 outburst. The direction of evolution is is shown with arrows in each case. Regions I and II do not show any discernible pattern.

We also look into the outburst profile and HID of the 2002-2004 'super'-outburst to compare it with that of the 'mini'-outburst. We divide the 2002-2004 lightcurve into 3 regions with each region comprising a rise, peak and decay to lower flux. This is shown in the top right panel of Figure 3.7. It is found that the flux peaks in regions I and III occur with a time interval of $\sim 600$ days between them, which is close to the recurrence period of the 'mini'-outbursts (Capitanio et al., 2015). Encouraged by this, we plot the HIDs corresponding to these regions in the middle (region I and II) and right panels (region III) at the bottom. There does not seem to be any significant pattern in the HID for regions I and II, with variation noticed in the HR only at higher flux. The outburst profile and HID of region III appear to be similar to that of the 'mini'-outbursts with a well-defined pattern seen in the HID (rightmost panels of Figure 3.7). The duration of this 'mini'-outburst embedded within the 'super'-outburst is almost twice the regular duration of $150-200$ days, extending to 311 days. Also, the small circular head in the HID of 'mini'-outbursts is greatly elongated and more defined in this segment of the 'super'-outburst. Similar outburst profile is also seen for the 2012-2014 'super'-outburst observed with *MAXI* although the duration of this 'mini'-outburst is $\sim 200$ days. Unfortunately, lack of complete coverage of the outburst by better resolution instruments prevents us from commenting on the HID for this duration. The variation in flux of a BHB is generally attributed to the variation of mass accretion rate. The 2002-2004 outburst was considered a standard outburst for 4U 1630-472, where clear state transitions were seen, driven by change in mass accretion rate (Tomsick et al., 2005). It was proposed by Capitanio et al. (2015) that the recurrent 'mini'-outbursts could be due to periodic perturbations in the system, which trigger this variation and force the disc temperature to increase independent of the disc accretion rate. These periodic perturbations can be attributed to limit cycle of accretion disc ionization instability (Cannizzo, 1993; Janiuk and Czerny, 2011), a third body orbiting around the binary system in a hierarchical configuration (Parmar et al., 1995) or the constant refilling from a companion star (Trudolyubov et al., 2001), all of which have been reviewed by Capitanio et al. (2015). In this case, the presence of a complete 'mini'-outburst towards the end of the 'super'-outburst could suggest that the underlying mechanism of the origin of 'super' and 'mini'-outbursts could be the same with varying contributions from some external perturbation which is consistently present for all outbursts. Detailed spectro-temporal analysis of these two different types of outbursts for its entire duration could hold the key to further understanding of their physical origins.

## 3.6 Revelations with the two-component flow approach

The unusual profile of the HID calls for further exploration of the source using more advanced physical models. In this case, we zeroed in on the two-component flow model as a viable option. This model has been implemented as a table model in XSPEC (Iyer et al., 2015) and applied in several previous works (Nandi et al., 2018; Radhika et al., 2018; Sreehari et al., 2019). The two component accretion flow model assumes a geometrically thin accretion disc comprising a Keplerian flow of matter at the equatorial plane, flanked by sub-Keplerian flow of matter on either sides (Chakrabarti and Titarchuk, 1995b; Chakrabarti and Mandal, 2006). The radial flow in the Keplerian disc is always subsonic whereas the sub-Keplerian flow is subsonic at the outer edge and becomes supersonic close to the black hole horizon. The supersonic sub-Keplerian flow encounters a centrifugal barrier on its inward journey towards the black hole that causes a shock transition. Here the flow becomes subsonic, with the bulk kinetic energy of the flow getting converted to thermal energy (Das et al., 2001). This region beyond the shock is called a post-shock corona (hereafter PSC) which is generally hot and dense. A more detailed explanation of the basic model from which it is built is given in Section 1.7.3.

The two-component flow model has two spectral components, namely the Keplerian disc which supplies the multi-colour blackbody photons, of which, a small fraction are inverse-Comptonised by the hot electrons in the PSC, producing the high energy X-ray power law photons (Chakrabarti and Titarchuk, 1995b; Chakrabarti and Mandal, 2006). Unlike the free normalization in the power-law component used in phenomenological spectral modelling, the normalization of the high energy component in the two-component model is decided by the geometry of the PSC. This model has five parameters, namely, mass of the BH (M), accretion rates of the Keplerian flow ($\dot{m}_d$) and sub-Keplerian flow ($\dot{m}_h$), size of the PSC ($x_s$) and a free normalization. We have expressed M in terms of solar mass ($M_\odot$), accretion rates in terms of Eddington rate ($\dot{m}_{Edd} = 1.4 \times 10^{18}$ M gm s$^{-1}$ with 10% efficiency) and radial distance in units of $r_g = 2GM/c^2$, where G is gravitational constant and c is speed of light in vacuum. We apply the two component flow model to the *SXT* spectrum in the energy range $0.7 - 6$ keV for Obs 1 and broadband energy spectra obtained using *SXT* and *LAXPC* for the rest of the observations in the energy range as specified in Table 2.2.

**Table 3.2:** Spectral fit parameters obtained using the two component flow model. 3 observations are chosen from 2016 and 2 from 2018 respectively, as a representative case for each state to fit the model.

| Year | 2016 | | | 2018 | |
|---|---|---|---|---|---|
| | LHS | IMS | HSS | HSS | IMS[c] |
| MJD | 57627.05 | 57627.69 | 57663.03 | 58344.18 | 58372.16 |
| $N_H$ ($\times 10^{22}$ at./cm$^2$) | $5.1 \pm 0.5$ | $7.8 \pm 0.2$ | $6.8 \pm 0.2$ | $7.1 \pm 0.1$ | $7.3 \pm 0.1$ |
| Mass ($M_\odot$) | $7 \pm 1$ | $8.5 \pm 0.2$ | $7.2 \pm 0.2$ | $7.3 \pm 0.2$ | $7.7 \pm 0.2$ |
| Shock Location ($r_g$) | 27[p] | $27 \pm 1$ | $6.0 \pm 0.3$ | $8.1 \pm 0.1$ | $8.9 \pm 0.1$ |
| Halo rate ($\dot{m}_{Edd}$) | $0.03 \pm 0.01$ | $0.04 \pm 0.01$ | 0.11[g] | 0.12[g] | 0.2[g] |
| Disc rate ($\dot{m}_{Edd}$) | $0.06 \pm 0.03$ | $0.55 \pm 0.04$ | $5.24 \pm 0.09$ | $4.7 \pm 0.1$ | $5.8 \pm 0.1$ |
| $\chi^2$/dof | 1.44 (36./25) | 1.39 (193/152) | 1.27 (416/328) | 1.05(388/370) | 1.11 (479/431) |

[c] IMS observed during the secondary peak

[p] parameter frozen to the next observation

[g] Unable to constrain errors as $\dot{m}_h$ plays minimal role in shaping the spectra

We have done the spectral modelling of 4U 1630-472 using two component accretion flow model for a few selected observations taken during the 2016 and 2018 outbursts. The source evolved from hard to soft state during the rise of the 2016 outburst, of which *AstroSat* observations exist for the 'canonical' hard and soft states, whereas observations from the soft state and the intermediate state are considered for the 2018 outburst (see Table 3.1, Figures 3.1 and 3.5). In the XSPEC implemented table model, the blackbody spectrum is calculated using the effective temperature ($T_{eff}$) of the Keplerian disc. In this work, we have done a custom implementation of the two-component model. Here, we have calculated the multi-colour blackbody spectrum using a colour temperature instead of effective temperature (Shimura and Takahara, 1995) as,

$$F_\nu = \pi B_\nu (fT_{eff})/f^4,$$

where $F_\nu$ is the local flux of radiation, $B_\nu$ is the Planck function and f is called the hardening factor. This modification is required, particularly for high accretion rates due to the electron scattering at the inner part of the disc. We find that f varies from 1.88 – 1.92 for the spectral fitting during HSS, whereas in the LHS, the effect of spectral hardening is less obvious.

We have used interstellar absorption model *phabs* along with two component accretion flow model for spectral modelling. An occasional requirement of Fe line represented by *gaussian* is also used. In Figure 3.8, we have presented the broadband spectral modelling of combined *SXT* and *LAXPC* data using two component model for 2016 and 2018 outbursts in the left and right panels separately. As *LAXPC* data could not be used, only the *SXT* spectrum is modelled for the LHS of 2016 outburst. The shock location could not be constrained and hence it was frozen to the value obtained in the next observation which was only a
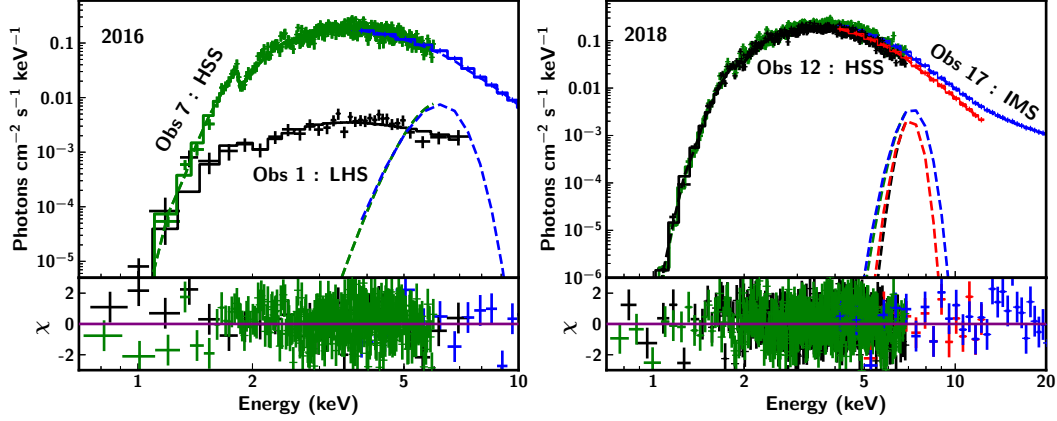
**Figure 3.8:** Broadband spectra from 2016 outburst in LHS and HSS state are shown in the left panel and HSS and IMS from 2018 are plotted in the right panel. Residuals are plotted in the bottom. Black and green denote *SXT* data and blue and red correspond to *LAXPC* data.

few hours away. For the other observations, we see that the model could fit the spectral data well with reasonably good statistics. The residual variation of each fit is well within $2\sigma$ as shown in bottom panels of Figure 3.8. The model fitted parameters along with the fitting statistics are presented in Table 3.2. We observe a high absorption column density as the source is located towards Galactic centre. The column density is particularly high in HSS, possibly indicating the existence of disc wind (King et al., 2012). As seen from Table 3.1, the absorption column density values obtained using phenomenological model lie in a similar range. The model fitted parameters for HSS states in both 2016 and 2018 outbursts are consistent as summarized in Table 3.2. In general, the Keplerian disc accretion rate is high in the HSS and the inner edge of the disc is closer to the BH whereas in the LHS the size of the PSC is larger, with a smaller value of disc accretion rate ($\dot{m}_d$). Thus, the relative balance between these two parameters (accretion rates) explain the state transition observed in 2016 outburst. However, spectral data of 2018 outburst does not show significant spectral evolution (see Table 3.1), and also the same is observed in the two component model parameters as mentioned in Table 3.2. The errors are estimated using the *migrad* method from the *minuit* library (James and Winkler, 2004). All the errors are quoted at 68% confidence level unless stated otherwise.

The larger value of the shock location during LHS and IMS of 2016 outburst relative to the other observations is consistent with the fact that the disc resides away from the black hole. Disc accretion rates are higher in all observations of 2018 outburst where the disc component is prominent. However, there is also a

slight increase in the halo accretion rate, accompanied by an increase in the shock location, suggesting an impending transition to a harder state. Although, it is to be noted that the errors on the halo accretion rates could not be constrained as the role of halo contribution is minimal ($\dot{m}_h << \dot{m}_d$) for the softer states. We find that the disc accretion rate is very high ($\sim 5\ \dot{m}_{Edd}$) for the soft states in both outbursts where the luminosity is close to Eddington luminosity, for a given distance and inclination of the source. This is because the Keplerian disc terminates at $6-9\ r_g$ (see Table 3.2), where the accretion efficiency is $\sim 2.5\%$ for a Schwarzschild black hole. We expect this accretion rate to be reduced by a factor of 5 for an extremely rotating black hole. Theoretical studies of the two-component flow on a spinning BH (Mandal and Mondal, 2018; Dihingia et al., 2020) show that the spectrum becomes relatively harder and is consistent with the reduction of accretion rate. However, inclusion of spin of the BH may alter the mass of the BH slightly as the accretion efficiency is weakly dependent on mass. It should also be stated that the contribution from jet/outflow is not taken into consideration for this application of the model. This could also affect the model normalisation as the current version of the model only considers the X-ray contribution from the accretion disc, as mentioned earlier. Also, an independent inclusion of *gaussian* is required along with the two component flow model because the associated physical process is not self-consistently included in the model currently. These could slightly affect the fit parameters. Following the inclusion of spin of the BH and these modifications, the model will be applied on previous outbursts of the source in future.

Using our model formalism, we can estimate the distance to the source from the model normalization ($N = \frac{\cos i}{d^2}$, where d is the distance in 10 kpc) of spectral fitting, provided, the inclination of the system is known. The model normalization may also be affected due to X-ray contribution from the jet/outflow in the LHS and the current version of the model considers the contribution only from the accretion disc. Hence, we particularly consider the HSS observations, where the contribution from the jet/outflow is minimum, to constrain the distance to the source. The model normalization provides a distance between $12-14$ kpc for $i = 60-70°$. Also, in our spectral modelling, mass of the source is a free parameter and estimates are consistent for both outbursts. As summarized in Table 3.2, the mass of the source lies between $6-8.7\ M_\odot$.

## 3.7  Mass estimates of the compact object - phenomenological and physical connotations

It is evident that the disc component is prominent during most of the *AstroSat* campaign. Using the apparent inner disc radius ($r_{in}$) obtained from the disc normalization (see Table 3.1), we can find the actual disc radius ($R_{in}$) using the relation $R_{in} = \xi.\kappa^2.r_{in}$ (Kubota et al., 1998; Makishima et al., 2000). The inner

disc radius is found to vary between 22 and 49 km for inclination varying from $60 - 70°$ (Tomsick et al., 1998; Seifina et al., 2014; King et al., 2014) and distance in the range $10 - 12$ kpc (Seifina et al., 2014; Kalemci et al., 2018). Assuming the disc to be at innermost stable circular orbit (ISCO), the mass of the compact object varies between 2.5 and 5.5 $M_\odot$. Since the generally accepted lower mass limit of a black hole is 3 $M_\odot$, the mass range can be quoted as $3 - 5.5$ $M_\odot$.
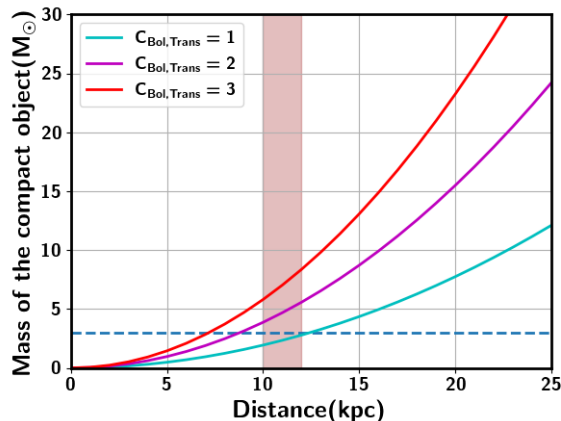


**Figure 3.9:** Mass is plotted as a function of distance using peak flux in the $2 - 50$ keV range during the 2018 outburst, considering flux transition factors as 1, 2 and 3. The source is assumed to be emitting at Eddington luminosity. The horizontal dashed line shows the lower limit of mass at 3 $M_\odot$. The shaded rectangle shows the possible mass in the distance range $10 - 12$ kpc.

Secondly, we attempt to constrain the mass of the compact object following the method adopted for IGR J17091-3624 by Altamirano et al. (2011). They assumed that the source was emitting at Eddington luminosity at the peak of the $2011 - 2013$ outburst, where bolometric flux is obtained as $F_{Bol} = C_{Bol,Peak}$ $F_{2–50 \text{ keV}}$ where $C_{Bol,Peak}$ is a bolometric correction factor $\leq 3$, which is the upper limit as suggested by Altamirano et al. (2011). *AstroSat* observed 4U 1630-472 while it underwent a transition from hard to soft state during the rising phase of 2016 outburst and soft to intermediate state during the decay phase of 2018 outburst, as a secondary outburst was triggered. We fit the combined spectrum with the phenomenological model and extrapolate in the harder energy range to find the unabsorbed flux from $2 - 50$ keV. During the soft to intermediate state transition in 2018, the maximum flux of $2.1 \times 10^{-8}$ ergs cm$^{-2}$ s$^{-1}$ was obtained. Considering a representative case where the source emits at Eddington luminosity, we obtain the mass of the black hole as a function of distance for different values of $C_{Bol,Peak}$ (1, 2 & 3) as the relation between $2 - 50$ keV flux and bolometric flux is unknown. Figure 3.9 shows the plot between distance in kpc and mass in solar mass units.

The probable values of the mass of the black hole as a function of distance is shown for three different values of $C_{\mathrm{Bol,Peak}}$.

With $C_{\mathrm{Bol,Peak}} = 1$, the mass of the compact object lies below 3 $M_\odot$ for a distance range of $10-12$ kpc, which is unlikely. Therefore, defining a lower limit of mass as 3 $M_\odot$ and $C_{\mathrm{Bol,Peak}} > 1$ and $\leq 3$, mass range is obtained as $3-9$ $M_\odot$ for a distance range of $10-12$ kpc. This is shown as the shaded vertical patch in Figure 3.9. The dashed horizontal line shows the lower mass limit of 3 $M_\odot$. However, the mass range so obtained, is based on the assumption that the source emits at Eddington luminosity. In the previous section, we obtained the mass estimates by modelling the broadband spectra using two component flow model. The mass parameter is obtained directly from the fits as lying between $6.8-7$ $M_\odot$. This is more constrained that the value obtained with the disc normalization. Therefore, the mass of the compact object lies in the range $3-9$ $M_\odot$, combining all three methods.

## 3.8   In a nutshell

In this chapter, we study the 2016 and 2018 outbursts of 4U 1630-472 using *AstroSat* and *MAXI*. Based on the HID and spectral parameters, we attempt to classify the outburst into different states. We also try to obtain a mass estimate using different methods. The results are summarized as follows:

- We attempt a global picture of the outburst and evolution of the source 4U 1630-472 for the 'mini'-outbursts which last from $150-200$ days based on the 2016, 2018 outbursts as shown in Figures 3.1 & 3.6. We also cross-verify it with the evolution of the 1998 and 1999 outbursts. The HID seems to follow a 'c'-shaped profile with a circular head at the upper end. A similar profile is seen towards the end of the 'super'-outburst of 2002-2004 with an elongated head.

- The source is captured in LHS for the first time using *AstroSat* at the beginning of the 2016 'mini'-outburst. The source moves from LHS to IMS within a few hours.

- The spectral and temporal characteristics of the source during the course of the two outbursts are studied. Although no QPOs are observed during any of the observations, we are able to categorize them into LHS, HSS and IMS states, based on the spectral parameters. However, further classification into HIMS and SIMS is not possible due to non-detection of QPOs and absence of high energy spectra from *LAXPC* due to possible contamination from the nearby source IGR J16320-4751.

- Mass of the compact object in the source 4U 1630-472 is estimated by three different methods, i.e., from the inner disc radius as $3-5.5$ M$_\odot$, from the bolometric luminosity as $3-9$ M$_\odot$ and and from spectral modelling using the two component flow model as $6-8.7$ M$_\odot$. Combining these results, we find the BH mass to lie within a range of $3-9$ M$_\odot$.

- The two component flow model seems to satisfactorily explain the spectral state transitions while retaining the preferred geometry for hard and soft states.

# Chapter 4

# Probing into the nature of the source MAXI J0637-430

The field of X-ray astronomy is as exciting as it is dynamic, partly due to the new discoveries made about supposedly well-known and studied sources, and partly due to the new sources being discovered from time to time. With the addition of an array of X-ray sky monitors and improved instruments, new sources are being discovered more frequently in the last few years than they have been in the last few decades. The discovery of new sources provides astronomers with more opportunities to test individual theoretical predictions. One such source that 'burst onto the scene' and initiated a barrage of ATels and scientific papers, is the X-ray transient source MAXI J0637-430, which went into an outburst in early November 2019.

## 4.1   A Star is Born

A bright new transient was reported in Negoro et al. (2019) at an RA and Dec of $06^{\mathrm{h}}37^{\mathrm{m}}43^{\mathrm{s}}$, $-43°03'15''$ respectively by *MAXI/GSC* on 3 November 2019. The source was predominantly soft, emitting at $\sim 60$ mCrab in the 2–4 keV energy band on 2 November 2019, which climbed to 200 mCrab by 3 November 2019. The 4−10 keV flux remained constant at around 50 mCrab. Follow-up observations with *Swift* came next, where a preliminary modelling of the $2-10$ keV X-ray spectrum was performed. Observations with *Swift/UVOT* aided in the localization of the source with a more precise estimate of the position ((RA, Dec) = ($06^{\mathrm{h}}$ $36^{\mathrm{m}}$ $23.6^{\mathrm{s}}$, $-42°$ $52'4.1''$) (Kennea et al., 2019). Preliminary spectral fits with the phenomenological model of an absorbed multicolour disc combined with a powerlaw component returned a disc temperature of 0.9 keV and a spectral index of 2.3. Strong evidence for MAXI J0637-430 being a low mass X-ray binary in outburst came with optical spectroscopy of the source with

*Goodman Spectrograph* on *SOuthern Astrophysical Research (SOAR)* telescope. Broad, double peaked H-α, He II 4686 emission lines at Galactic velocities were observed in the low resolution spectrum (Strader et al., 2019).

The first *NuSTAR* observation was performed on 5 November 2019 (Tomsick et al., 2019). This was significant as the *NuSTAR* energy band extends from 3 to 79 keV, thereby affording the first look at the higher energy spectra. Additional features like residuals at 6 keV and above 20 keV were reported. However, confirmation of reflection features could not be obtained without detailed spectral modelling. Radio detection was also reported on 6 November 2019 (Russell et al., 2019) using *Australian Telescope Compact Array (ATCA)*. Flux densities of 66 ± 15 μJy at 5.5 GHz and 60 ± 10 μJy at 9 GHz were measured. The discrimination between emission from a compact object and a discrete ejection event in a transient jet was not possible, although, the latter is more probable based on the softness of the source. Optical observations followed, revealing an optical counterpart with average source magnitude of g= 16.1 (Hambsch et al., 2019; Kravtsov et al., 2019; Li and Kong, 2019). A near IR counterpart was also detected (Murata et al., 2019). An observation with *AstroSat* was reported (Thomas et al., 2019) on 8 November 2019, where the spectrum was slightly harder than the one obtained with *Swift/XRT* and *NuSTAR*.

Every new discovery prompts answers to a few general questions. The first one almost invariably relates to the nature of the compact object. Is it a neutron star or a black hole? Secondly, are state transitions clearly observed or is it a 'failed' outburst? Finally, we look past the peripherals and get down to brass tacks. What are the physical parameters of the source - mass of the compact object, its spin and so on? We attempt to answer these questions through our studies. In the following sections we detail the steps followed in our quest and discuss the implications.

## 4.2 A comprehensive list of observations - Data, data, data!

Multiple instruments were pointed at the source MAXI J0637-430, some more frequently than the others. *NICER* and *Swift* observed the source in X-rays regularly. *NICER* observed the source for a total of 101 times throughout the duration of its outburst, while 96 observations are available with *Swift*. *NuSTAR* observations were performed 9 times. *AstroSat* observed the source three times, when the source was bright and a transition to the hard state had not yet been reported. We plot the *MAXI* lightcurve in the 2–20 keV energy range in the top panel of Figure 4.1. The second and third panels show the *NICER* lightcurve in the 0.5–10 keV range and hardness ratio respectively. The green and red vertical lines correspond to *AstroSat* and *Swift-XRT* observations respectively, used in this study. Each point in the second and third panel corresponds to a *NICER* observation analysed

here. We consider *NICER* and *AstroSat* as our primary instruments. *Swift-XRT* is used to fill in the data gaps as *NuSTAR* data was not available at the time. The details of observations chosen are given in Tables 4.1, 4.2 and 4.3.
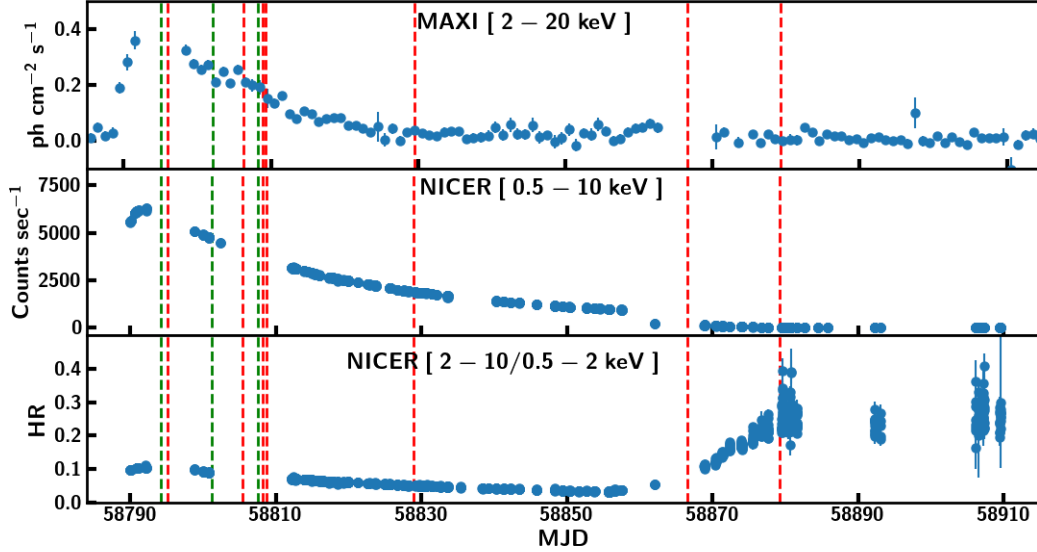


**Figure 4.1:** *MAXI* lightcurve is shown in the top panel along with observations from *Swift-XRT* and *AstroSat* in red and green vertical lines respectively. The *NICER* lightcurve in the $2.5 - 10$ keV range along with the hardness ratios are plotted in the second and third panels respectively.

### 4.2.1  *NICER*

*NICER* observed MAXI J0637-430 at regular intervals since 3 November 2019 till the end of April 2020. We obtain all available data for the source between 3 November 2019 and 30 January 2020. For observations from 3 February 2020 to March 2020, where the source count rate is below 10 counts s$^{-1}$ and variation in hardness ratios and spectral parameters is minimal, we consider only those observations where the exposure time is $> 1.5$ ks. Details of the observations and the count rates are given in Table 4.1. Data reduction is performed using the steps detailed in Chapter 2. The latest version of Redistribution Matrix File (RMF) provided by the team is used. Ancillary Response Files (ARF) for 50 detectors are co-added to generate the final ARF file. The spectra are rebinned to have a minimum of 25 counts per bin. To create the lightcurve and obtain hardness ratios, we first produce 1 s binned lightcurves in the $0.5-10$, $0.5-2$ and $2-10$ keV bands using XSELECT. The Hardness ratio is defined as the ratio of counts in the
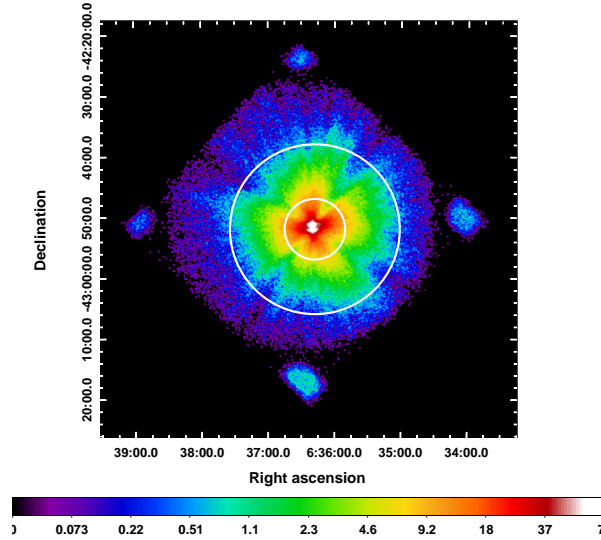
**Figure 4.2:** *SXT* image of the source observed on 21 November 2019. An annular source region with inner and outer radii of 5 and 14 arcmin respectively is chosen for spectral extraction to avoid pile-up issues.

$2-10$ keV band to the counts in $0.5-2$ keV band. The lightcurves in the $0.3-12$ keV range with a binsize of 5 ms are used to generate the PDS.

### 4.2.2 *AstroSat*

*AstroSat* carried out ToO observations of MAXI J0637-430 in three different intervals on 8, 15 and 21 November 2019. The Level-1 data of *SXT* and *LAXPC* are obtained from the Indian Space Science Data Centre (ISSDC) archive [1]. The details of the *AstroSat* observations are given in Table 4.2. *SXT* Level-1 data is obtained in the Photon Counting (PC) mode. The details of the pipeline used and the reduction techniques are presented in Chapter 2. Pile-up issues are observed in the data at a count rate greater than 40 counts s$^{-1}$. In such a scenario, an inner region is excluded such that the count rate falls below this limit[2]. Therefore, we consider an annular source region with an outer radius of 14 arcmin [3]. Different values of inner radii are taken to bring the count rate below the specified limit. We exclude a central circular region with radius $8'$, $7'$ and $5'$ for observations on 8, 15 and 21 November respectively, to generate the lightcurve and spectra. *SXT* image from 21 November 2019 is shown in Figure 4.2. Response and background

---

[1]http://astrobrowse.issdc.gov.in/astro_archive/archive

[2]https://www.tifr.res.in/~astrosat_sxt/dataanalysis.html

[3]Recent studies with other sources have revealed that the pile-up limit could be raised to $\sim$ 80-100 counts s$^{-1}$(private communication with *SXT* team)

files provided by the team are used. To correct for offset, `arf` file is generated using `sxtARFmodule` provided separately[4]. *SXT* data are grouped by 30 counts per bin for better statistics.

*LAXPC* data is obtained in the Event Analysis (EA) mode for all the observations. Only single event data from *LAXPC20* is used for analysis for reasons elucidated in Chapter 2. Background is generated using the background model closest in time to the observations. The background contributed to more than 50% of the observed flux beyond 25 keV. Hence, we perform the spectral analysis for *LAXPC* in the $4-25$ keV energy band. The exposure times for both instruments are given in Table 4.2. To generate PDS, lightcurves are obtained in the $3-12$ keV band with 5 ms binsize for comparison with *NICER* PDS.

### 4.2.3 *Swift-XRT*

Four observations of *Swift-XRT* in Windowed Timing (WT) mode, within or close to the dates of the *AstroSat* observations, are considered, to complement the existing *NICER* and *AstroSat* data. Details of the observations are given in Table 4.3. An additional four observations are chosen corresponding to different epochs during the outburst, to check for consistency in spectral parameters with other instruments. These are marked as red dashed lines in Figure 4.1. Bulk of the *Swift* observations are already analysed in Tetarenko et al. (2021). Here, we only present a subset of those observations. The $0.5-10$ keV spectra are generated using the standard online tools provided by the UK *Swift* Science Data Centre (Evans et al., 2009), as mentioned in Chapter 2. Slight variation is seen in the results obtained by Tetarenko et al. (2021) when compared with our results. The photon index is lower and the disc temperatures are slightly higher for all the observations in the soft state presented in Tetarenko et al. (2021). Count rate exceeds the pile-up limit of 100 counts s$^{-1}$ in the WT mode during the soft state. Manual selection of source region was performed in Tetarenko et al. (2021), which probably affected the results due to severe pile-up issues in the WT mode observations of this source. Effects of pile-up are studied in detail in the Appendix of Baby et al. (2021). The spectra are grouped to have a minimum of 5 counts per bin.

---

[4]https://www.tifr.res.in/~astrosat_sxt/dataanalysis.html

**Table 4.1:** Details of *NICER* observations chosen for analysis are provided in the first 5 columns. Spectral parameters fitted with model *TBabs (thcomp ⊗ diskbb)* are presented with 90% confidence.

| ObsId | Date | MJD | Exp. time (ks) | Rate (counts s$^{-1}$) | $n_H$ ($\times 10^{20}$ cm$^{-2}$) | $\Gamma$ | $f_{cov}^a$ | $T_{in}$ (keV) | $N_{diskbb}$ | $F_{0.5-10\,keV}$ ($\times 10^{-10}$ erg cm$^{-2}$ s$^{-1}$) | $\chi^2$/dof |
|---|---|---|---|---|---|---|---|---|---|---|---|
| 2200950101 | 2019-11-03 | 58790.89 | 1.1 | 5607 | $2.3^{+0.1}_{-0.1}$ | $4.60^{+0.10}_{-0.02}$ | $0.20 \pm 0.10$ | $0.58^{+0.001}_{-0.001}$ | $3606^{+19}_{-62}$ | $72.00 \pm 0.20$ | 457/556 |
| 2200950102 | 2019-11-04 | 58791.02 | 4.5 | 6140 | $2.5^{+0.2}_{-0.2}$ | $4.50^{+0.30}_{-0.30}$ | $0.32^{+0.08}_{-0.06}$ | $0.59^{+0.002}_{-0.003}$ | $3731^{+19}_{-87}$ | $79.40 \pm 0.20$ | 576/702 |
| 2200950103 | 2019-11-05 | 58792.05 | 0.6 | 6226 | $2.6^{+0.2}_{-0.2}$ | $4.30^{+0.10}_{-0.10}$ | $0.25 \pm 0.07$ | $0.59^{+0.002}_{-0.002}$ | $3673^{+19}_{-62}$ | $81.50 \pm 0.40$ | 540/534 |
| 2200950104 | 2019-11-06 | 58793.15 | 0.3 | 6271 | $2.8^{+0.3}_{-0.2}$ | $4.00^{+0.10}_{-0.10}$ | $0.25 \pm 0.08$ | $0.59^{+0.003}_{-0.002}$ | $3826^{+19}_{-75}$ | $82.70 \pm 0.30$ | 428/501 |
| 2200950107 | 2019-11-12 | 58799.70 | 0.6 | 5068 | $2.0^{+0.2}_{-0.1}$ | $2.90^{+0.03}_{-0.03}$ | $0.25 \pm 0.03$ | $0.55^{+0.002}_{-0.002}$ | $3784^{+19}_{-72}$ | $65.70 \pm 0.10$ | 562/573 |
| 2200950108 | 2019-11-13 | 58800.22 | 1.2 | 4892 | $2.1^{+0.2}_{-0.2}$ | $3.20^{+0.04}_{-0.03}$ | $0.15 \pm 0.02$ | $0.56^{+0.002}_{-0.002}$ | $3594^{+19}_{-51}$ | $61.50 \pm 0.20$ | 544/585 |
| 2200950109 | 2019-11-14 | 58801.05 | 1.1 | 4759 | $2.2^{+0.2}_{-0.2}$ | $3.76^{+0.04}_{-0.05}$ | $0.25 \pm 0.04$ | $0.55^{+0.002}_{-0.002}$ | $3746^{+19}_{-61}$ | $60.90 \pm 0.30$ | 526/589 |
| 2200950112a | 2019-11-26 | 58813.03 | 3.2 | 3140 | $2.1^{+0.1}_{-0.2}$ | $4.09^{+0.04}_{-0.04}$ | $0.25 \pm 0.03$ | $0.49^{+0.001}_{-0.001}$ | $3722^{+19}_{-52}$ | $35.90 \pm 0.20$ | 639/577 |
| 2200950112b | 2019-11-26 | 58813.48 | 2.5 | 3111 | $2.0^{+0.2}_{-0.2}$ | $4.00^{+0.20}_{-0.20}$ | $0.31^{+0.07}_{-0.06}$ | $0.49^{+0.004}_{-0.004}$ | $3824^{+19}_{-127}$ | $35.60 \pm 0.30$ | 562/570 |
| 2200950113 | 2019-11-27 | 58814.77 | 1.2 | 2988 | $2.1^{+0.2}_{-0.2}$ | $3.70^{+0.30}_{-0.30}$ | $0.26^{+0.03}_{-0.09}$ | $0.48^{+0.004}_{-0.005}$ | $3892^{+19}_{-150}$ | $34.20 \pm 0.20$ | 504/505 |
| 2200950114 | 2019-11-28 | 58815.22 | 1.9 | 2913 | $2.1^{+0.2}_{-0.4}$ | $4.20^{+0.30}_{-0.30}$ | $0.40^{+0.10}_{-0.10}$ | $0.47^{+0.004}_{-0.005}$ | $3980^{+19}_{-157}$ | $33.00 \pm 0.20$ | 575/537 |
| 2200950115 | 2019-11-29 | 58816.26 | 2.0 | 2789 | $2.0^{+0.2}_{-0.2}$ | $4.45^{+0.06}_{-0.05}$ | $0.35 \pm 0.05$ | $0.47^{+0.002}_{-0.002}$ | $3825^{+19}_{-34}$ | $31.30 \pm 0.20$ | 520/516 |
| 2200950116 | 2019-11-30 | 58817.60 | 1.1 | 2725 | $2.2^{+0.2}_{-0.2}$ | $4.14^{+0.07}_{-0.07}$ | $0.25 \pm 0.05$ | $0.47^{+0.002}_{-0.002}$ | $3826^{+19}_{-73}$ | $30.70 \pm 0.30$ | 520/464 |
| 2200950117 | 2019-12-01 | 58818.19 | 1.8 | 2638 | $1.8^{+0.1}_{-0.2}$ | $4.19^{+0.06}_{-0.06}$ | $0.25 \pm 0.04$ | $0.47^{+0.002}_{-0.002}$ | $3658^{+19}_{-32}$ | $29.40 \pm 0.10$ | 561/494 |
| 2200950118 | 2019-12-02 | 58819.42 | 0.7 | 2570 | $2.2^{+0.2}_{-0.2}$ | $3.96^{+0.07}_{-0.07}$ | $0.25 \pm 0.06$ | $0.46^{+0.001}_{-0.002}$ | $3904^{+19}_{-88}$ | $28.60 \pm 0.20$ | 460/435 |
| 2200950119 | 2019-12-03 | 58820.19 | 2.9 | 2482 | $1.8^{+0.2}_{-0.2}$ | $4.00^{+0.20}_{-0.30}$ | $0.29^{+0.07}_{-0.06}$ | $0.46^{+0.004}_{-0.004}$ | $3772^{+19}_{-132}$ | $27.20 \pm 0.10$ | 630/547 |
| 2200950120 | 2019-12-05 | 58822.19 | 0.6 | 2379 | $1.9^{+0.2}_{-0.2}$ | $3.72^{+0.06}_{-0.06}$ | $0.25 \pm 0.05$ | $0.45^{+0.002}_{-0.002}$ | $3896^{+19}_{-99}$ | $26.40 \pm 0.10$ | 452/420 |
| 2200950121 | 2019-12-06 | 58823.50 | 1.9 | 2277 | $1.8^{+0.2}_{-0.2}$ | $3.75^{+0.04}_{-0.04}$ | $0.25 \pm 0.03$ | $0.45^{+0.002}_{-0.002}$ | $3856^{+19}_{-73}$ | $24.80 \pm 0.10$ | 602/514 |
| 2200950122 | 2019-12-07 | 58824.47 | 1.8 | 2217 | $2.1^{+0.2}_{-0.3}$ | $4.00^{+0.30}_{-0.20}$ | $0.36^{+0.10}_{-0.08}$ | $0.44^{+0.005}_{-0.005}$ | $4152^{+19}_{-188}$ | $24.10 \pm 0.10$ | 513/508 |
| 2200950123 | 2019-12-08 | 58825.80 | 1.2 | 2124 | $1.9^{+0.2}_{-0.2}$ | $3.92^{+0.05}_{-0.05}$ | $0.30 \pm 0.05$ | $0.43^{+0.002}_{-0.002}$ | $3987^{+19}_{-89}$ | $23.00 \pm 0.20$ | 474/459 |
| 2200950124 | 2019-12-09 | 58826.53 | 2.1 | 2071 | $1.7^{+0.2}_{-0.2}$ | $4.08^{+0.04}_{-0.03}$ | $0.30 \pm 0.04$ | $0.43^{+0.003}_{-0.002}$ | $3886^{+19}_{-76}$ | $22.30 \pm 0.10$ | 592/505 |
| 2200950125 | 2019-12-10 | 58827.57 | 0.9 | 1994 | $2.0^{+0.2}_{-0.2}$ | $4.50^{+0.10}_{-0.10}$ | $0.30 \pm 0.08$ | $0.43^{+0.002}_{-0.002}$ | $3881^{+19}_{-95}$ | $21.20 \pm 0.20$ | 587/413 |
| 2200950126 | 2019-12-11 | 58828.34 | 1.4 | 1944 | $1.8^{+0.2}_{-0.1}$ | $4.38^{+0.07}_{-0.06}$ | $0.30 \pm 0.06$ | $0.43^{+0.002}_{-0.002}$ | $3840^{+19}_{-84}$ | $20.60 \pm 0.10$ | 524/441 |
| 2200950127 | 2019-12-12 | 58829.11 | 1.2 | 1920 | $1.9^{+0.2}_{-0.2}$ | $4.24^{+0.06}_{-0.06}$ | $0.30 \pm 0.06$ | $0.42^{+0.002}_{-0.002}$ | $3969^{+19}_{-92}$ | $20.30 \pm 0.20$ | 493/433 |
| 2200950128 | 2019-12-13 | 58830.08 | 2.1 | 1852 | $1.8^{+0.2}_{-0.2}$ | $4.26^{+0.04}_{-0.05}$ | $0.30 \pm 0.05$ | $0.42^{+0.002}_{-0.002}$ | $3855^{+19}_{-78}$ | $19.50 \pm 0.10$ | 532/468 |
| 2200950129 | 2019-12-14 | 58831.04 | 3.0 | 1822 | $1.9^{+0.2}_{-0.2}$ | $4.15^{+0.04}_{-0.04}$ | $0.30 \pm 0.04$ | $0.42^{+0.002}_{-0.002}$ | $3923^{+19}_{-72}$ | $19.10 \pm 0.20$ | 596/502 |

**Table 4.1 continued**

| | | | | | | | | | | | |
|---|---|---|---|---|---|---|---|---|---|---|---|
| 2200950130 | 2019-12-15 | 58832.32 | 2.0 | 1770 | $2.1^{+0.1}_{-0.2}$ | $4.04^{+0.05}_{-0.04}$ | $0.30\pm0.04$ | $0.41^{+0.002}_{-0.002}$ | $4078^{+19}_{-83}$ | $18.50\pm0.20$ | 547/471 |
| 2200950131 | 2019-12-16 | 58833.35 | 1.0 | 1722 | $2.2^{+0.2}_{-0.3}$ | $4.50^{+0.10}_{-0.10}$ | $0.30\pm0.07$ | $0.41^{+0.003}_{-0.003}$ | $3994^{+19}_{-99}$ | $18.00\pm0.10$ | 399/391 |
| 2200950132 | 2019-12-17 | 58834.39 | 1.4 | 1673 | $1.7^{+0.2}_{-0.1}$ | $4.47^{+0.06}_{-0.07}$ | $0.30\pm0.07$ | $0.41^{+0.002}_{-0.002}$ | $3818^{+19}_{-91}$ | $17.30\pm0.20$ | 462/419 |
| 2200950133 | 2019-12-18 | 58835.99 | 0.8 | 1605 | $2.1^{+0.4}_{-0.3}$ | $4.01^{+0.07}_{-0.07}$ | $0.30\pm0.06$ | $0.40^{+0.002}_{-0.002}$ | $4204^{+19}_{-123}$ | $16.70\pm0.30$ | 423/389 |
| 2200950135 | 2019-12-22 | 58839.22 | 0.8 | 1470 | $2.4^{+0.4}_{-0.4}$ | $4.40^{+0.50}_{-0.50}$ | $0.40^{+0.20}_{-0.20}$ | $0.38^{+0.007}_{-0.009}$ | $4634^{+19}_{-369}$ | $14.90\pm0.20$ | 429/379 |
| 2200950136 | 2019-12-23 | 58840.06 | 0.5 | 1446 | $2.7^{+0.3}_{-0.3}$ | $4.10^{+0.10}_{-0.10}$ | $0.30\pm0.09$ | $0.38^{+0.003}_{-0.003}$ | $4596^{+19}_{-153}$ | $14.80\pm0.20$ | 432/336 |
| 2200950137 | 2019-12-24 | 58841.09 | 0.8 | 1405 | $2.0^{+0.3}_{-0.3}$ | $4.19^{+0.09}_{-0.08}$ | $0.30\pm0.08$ | $0.38^{+0.002}_{-0.002}$ | $4213^{+19}_{-127}$ | $14.20\pm0.10$ | 495/386 |
| 2200950138 | 2019-12-25 | 58842.13 | 1.0 | 1371 | $2.1^{+0.3}_{-0.3}$ | $4.12^{+0.07}_{-0.07}$ | $0.30\pm0.07$ | $0.38^{+0.002}_{-0.002}$ | $4220^{+19}_{-124}$ | $13.90\pm0.10$ | 472/377 |
| 2200950139 | 2019-12-26 | 58843.16 | 1.0 | 1344 | $1.6^{+0.2}_{-0.2}$ | $4.02^{+0.07}_{-0.06}$ | $0.30\pm0.06$ | $0.38^{+0.002}_{-0.002}$ | $4320^{+19}_{-140}$ | $13.70\pm0.10$ | 484/381 |
| 2200950140 | 2019-12-27 | 58844.32 | 0.9 | 1307 | $2.0^{+0.4}_{-0.4}$ | $3.40^{+0.30}_{-0.30}$ | $0.20^{+0.09}_{-0.06}$ | $0.38^{+0.005}_{-0.006}$ | $4289^{+19}_{-249}$ | $13.00\pm0.10$ | 459/385 |
| 2200950142 | 2019-12-29 | 58846.66 | 1.1 | 1224 | $2.0^{+0.3}_{-0.3}$ | $4.00^{+0.06}_{-0.06}$ | $0.30\pm0.06$ | $0.37^{+0.002}_{-0.003}$ | $4324^{+19}_{-132}$ | $12.10\pm0.20$ | 486/372 |
| 2200950144 | 2020-01-01 | 58849.22 | 1.7 | 1150 | $2.0^{+0.3}_{-0.5}$ | $4.12^{+0.05}_{-0.05}$ | $0.30\pm0.10$ | $0.36^{+0.002}_{-0.002}$ | $4392^{+19}_{-126}$ | $11.40\pm0.10$ | 518/421 |
| 2200950145 | 2020-01-02 | 58850.26 | 1.9 | 1123 | $2.0^{+0.2}_{-0.2}$ | $3.90^{+0.04}_{-0.04}$ | $0.30\pm0.04$ | $0.36^{+0.002}_{-0.002}$ | $4402^{+19}_{-120}$ | $11.00\pm0.10$ | 486/409 |
| 2200950146 | 2020-01-03 | 58851.23 | 1.1 | 1098 | $2.5^{+0.3}_{-0.3}$ | $4.15^{+0.08}_{-0.07}$ | $0.30\pm0.07$ | $0.36^{+0.002}_{-0.002}$ | $4543^{+19}_{-138}$ | $10.80\pm0.10$ | 497/360 |
| 2200950147 | 2020-01-04 | 58852.46 | 1.3 | 1061 | $1.8^{+0.3}_{-0.4}$ | $4.28^{+0.07}_{-0.07}$ | $0.30\pm0.06$ | $0.36^{+0.002}_{-0.002}$ | $4143^{+19}_{-123}$ | $10.30\pm0.30$ | 448/359 |
| 2200950148 | 2020-01-05 | 58853.49 | 1.2 | 1049 | $2.1^{+0.3}_{-0.3}$ | $4.05^{+0.06}_{-0.06}$ | $0.30\pm0.06$ | $0.36^{+0.002}_{-0.002}$ | $4440^{+19}_{-142}$ | $10.20\pm0.20$ | 398/360 |
| 2200950149 | 2020-01-06 | 58854.65 | 1.1 | 1026 | $2.5^{+0.3}_{-0.4}$ | $4.20^{+0.40}_{-0.40}$ | $0.50^{+0.20}_{-0.20}$ | $0.34^{+0.006}_{-0.008}$ | $5024^{+19}_{-576}$ | $10.00\pm0.20$ | 432/359 |
| 2200950151 | 2020-01-08 | 58856.52 | 2.7 | 979 | $2.6^{+0.4}_{-0.4}$ | $4.40^{+0.20}_{-0.20}$ | $0.50^{+0.10}_{-0.10}$ | $0.34^{+0.005}_{-0.006}$ | $5241^{+19}_{-344}$ | $9.50\pm0.10$ | 434/424 |
| 2200950152 | 2020-01-09 | 58857.37 | 1.2 | 968 | $2.1^{+0.4}_{-0.4}$ | $3.30^{+0.20}_{-0.20}$ | $0.24^{+0.06}_{-0.08}$ | $0.34^{+0.005}_{-0.005}$ | $4585^{+19}_{-289}$ | $9.30\pm0.10$ | 442/389 |
| 2200950153 | 2020-01-10 | 58858.34 | 1.0 | 945 | $2.6^{+0.5}_{-0.4}$ | $3.20^{+0.20}_{-0.20}$ | $0.34^{+0.08}_{-0.06}$ | $0.33^{+0.006}_{-0.006}$ | $5383^{+19}_{-422}$ | $9.40\pm0.10$ | 446/397 |
| 2200950154 | 2020-01-14 | 58862.85 | 0.3 | 197 | $2.5^f$ | $2.21^{+0.09}_{-0.09}$ | $0.29^{+0.04}_{-0.04}$ | $0.19^{+0.005}_{-0.005}$ | $10636^{+19}_{-1073}$ | $1.96\pm0.03$ | 221/219 |
| 2200950155 | 2020-01-21 | 58869.71 | 1.1 | 134 | $2.5^f$ | $1.89^{+0.03}_{-0.03}$ | $0.27^{+0.01}_{-0.01}$ | $0.13^{+0.003}_{-0.003}$ | $46265^{+19}_{-5144}$ | $1.54\pm0.02$ | 355/383 |
| 2200950156 | 2020-01-23 | 58871.19 | 1.1 | 109 | $2.5^f$ | $1.86^{+0.03}_{-0.03}$ | $0.29^{+0.01}_{-0.01}$ | $0.12^{+0.003}_{-0.003}$ | $47390^{+19}_{-6368}$ | $1.34\pm0.02$ | 348/375 |
| 2200950157 | 2020-01-24 | 58872.03 | 1.4 | 82 | $2.5^f$ | $1.84^{+0.02}_{-0.03}$ | $0.34^{+0.02}_{-0.02}$ | $0.11^{+0.004}_{-0.004}$ | $49297^{+19}_{-9675}$ | $1.12\pm0.02$ | 376/388 |
| 2200950158 | 2020-01-25 | 58873.19 | 0.8 | 64 | $2.5^f$ | $1.78^{+0.04}_{-0.03}$ | $0.39^{+0.03}_{-0.03}$ | $0.12^{+0.006}_{-0.004}$ | $27830^{+19}_{-9985}$ | $0.95\pm0.02$ | 260/298 |
| 2200950159 | 2020-01-26 | 58874.81 | 2.5 | 58 | $2.5^f$ | $1.82^{+0.02}_{-0.02}$ | $0.46^{+0.02}_{-0.02}$ | $0.11^{+0.005}_{-0.006}$ | $33195^{+19}_{-7506}$ | $0.87\pm0.01$ | 437/449 |
| 2200950160 | 2020-01-28 | 58876.36 | 1.2 | 44 | $2.5^f$ | $1.82^{+0.03}_{-0.03}$ | $0.58^{+0.04}_{-0.05}$ | $0.11^{+0.010}_{-0.005}$ | $19041^{+19}_{-6906}$ | $0.71\pm0.01$ | 334/333 |
| 2200950161 | 2020-01-29 | 58877.58 | 1.2 | 30 | $2.5^f$ | $1.72^{+0.03}_{-0.04}$ | $0.73^{+0.06}_{-0.06}$ | $0.12^{+0.020}_{-0.010}$ | $9619^{+19}_{-3691}$ | $0.59\pm0.01$ | 308/299 |
| 2200950162 | 2020-01-30 | 58878.42 | 1.3 | 26 | $2.5^f$ | $1.78^{+0.04}_{-0.04}$ | $0.85^{+0.08}_{-0.08}$ | $0.12^{+0.020}_{-0.010}$ | $8073^{+19}_{-4317}$ | $0.50\pm0.02$ | 326/298 |

**Table 4.1 continued**

| | | | | | | | | | |
|---|---|---|---|---|---|---|---|---|---|
| 2200950164 2020-02-01 58880.23 | 5.0 | 20 | $2.5^f$ | $1.69^{+0.02}_{-0.02}$ | $0.92^{+0.04}_{-0.04}$ | $0.14^{+0.020}_{-0.020}$ | $2852^{+19}_{-112}$ | $0.44 \pm 0.02$ | 535/525 |
| 2200950165 2020-02-02 58881.07 | 3.1 | 17 | $2.5^f$ | $1.76^{+0.01}_{-0.02}$ | $1.00 \pm 0.10$ | $0.10^f$ | $8974^{+19}_{-135}$ | $0.36 \pm 0.04$ | 369/397 |
| 2200950166 2020-02-03 58882.43 | 1.6 | 15 | $2.5^f$ | $1.77^{+0.02}_{-0.03}$ | $1.00 \pm 0.10$ | $0.10^f$ | $7995^{+19}_{-172}$ | $0.32 \pm 0.02$ | 306/282 |
| 2200950176 2020-02-14 58893.13 | 1.6 | 8 | $2.5^f$ | $1.72^{+0.02}_{-0.03}$ | $1.00 \pm 0.20$ | $0.10^f$ | $4287^{+19}_{-126}$ | $0.18 \pm 0.02$ | 187/220 |
| 2200950188 2020-02-28 58907.04 | 1.9 | 5 | $2.5^f$ | $1.70^{+0.04}_{-0.03}$ | $1.00 \pm 0.20$ | $0.10^f$ | $2424^{+19}_{-76}$ | $0.11 \pm 0.02$ | 200/199 |
| 2200950189 2020-02-29 58908.05 | 1.6 | 5 | $2.5^f$ | $1.65^{+0.04}_{-0.04}$ | $1.00 \pm 0.20$ | $0.10^f$ | $2331^{+19}_{-79}$ | $0.12 \pm 0.01$ | 220/187 |
| 3200950102 2020-03-02 58910.32 | 1.6 | 4 | $2.5^f$ | $1.77^{+0.05}_{-0.05}$ | $1.00 \pm 0.40$ | $0.10^f$ | $2282^{+19}_{-134}$ | $0.09 \pm 0.00$ | 153/146 |

[a] Errors quoted with 68% confidence where a single value is given

[f] parameter frozen

**Table 4.2:** Details of *AstroSat* observations chosen for analysis are given in the first 7 columns. Spectral parameters fitted with model $TBabs\ (thcomp \otimes diskbb)$ are presented with 90% confidence.

| ObsId | Date | MJD | SXT | | LAXPC | | $n_H$ | $\Gamma$ | $f_{cov}^{a}$ | $T_{in}$ | $N_{diskbb}$ | $F_{0.5-10\,keV}$ | $\chi^2$/dof |
|---|---|---|---|---|---|---|---|---|---|---|---|---|---|
| | | | Exp. time | Rate | Exp. time | Rate | | | | | | | |
| | | | (ks) | counts s$^{-1}$ | (ks) | counts s$^{-1}$ | ($\times 10^{20}$ cm$^{-2}$) | | | (keV) | | ($\times 10^{-10}$ erg cm$^{-2}$ s$^{-1}$) | |
| 3290 | 2019-11-08 | 58795.09 | 5.6 | 34 | 6.1 | 154 | $2.6^{+0.5}_{-0.5}$ | $2.32^{+0.08}_{-0.09}$ | $0.04^{+0.01}_{-0.01}$ | $0.63^{+0.006}_{-0.006}$ | $2729^{+19}_{-112}$ | $73.60 \pm 0.10$ | 486/392 |
| 3306 | 2019-11-15 | 58802.07 | 8.0 | 33 | 14.7 | 92 | $2.5^{+0.5}_{-0.5}$ | $2.33^{+0.09}_{-0.09}$ | $0.04^{+0.01}_{-0.01}$ | $0.58^{+0.005}_{-0.005}$ | $2018^{+19}_{-81}$ | $39.80 \pm 0.10$ | 508/397 |
| 3328 | 2019-11-21 | 58808.28 | 6.0 | 38 | 11.4 | 96 | $2.5^{f}$ | $2.58^{+0.09}_{-0.09}$ | $0.17^{+0.02}_{-0.02}$ | $0.53^{+0.005}_{-0.005}$ | $2054^{+19}_{-80}$ | $29.50 \pm 0.10$ | 478/393 |

$^f$ parameter frozen

**Table 4.3:** Details of *Swift-XRT* observations chosen for analysis are given in the first 5 columns. Spectral parameters fitted with model $TBabs\ (thcomp \otimes diskbb)$ are presented with 90% confidence

| ObsId | Date | MJD | Exp. time | Rate | $n_H$ | $\Gamma$ | $f_{cov}^{b}$ | $T_{in}$ | $N_{diskbb}$ | $F_{0.5-10\,keV}$ | $\chi^2$/dof |
|---|---|---|---|---|---|---|---|---|---|---|---|
| | | | (ks) | counts s$^{-1}$ | ($\times 10^{20}$ cm$^{-2}$) | | | (keV) | | ($\times 10^{-10}$ erg cm$^{-2}$ s$^{-1}$) | |
| 12172002 | 2019-11-08 | 58795.96 | 0.6 | 7.7 | $2.5^{f}$ | - | - | $0.61^{+0.030}_{-0.030}$ | $2889^{+19}_{-495}$ | $68.00 \pm 1.00$ | 371/390 |
| 12172003 | 2019-11-09 | 58796.74 | 1.4 | 7.2 | $2.5^{f}$ | $2.60^{+0.50}_{-0.30}$ | $0.20^{+0.20}_{-0.20}$ | $0.59^{+0.020}_{-0.020}$ | $3004^{+19}_{-364}$ | $69.90 \pm 0.30$ | 324/321 |
| 12172012 | 2019-11-19 | 58806.31 | 1.1 | 8.1 | $2.5^{f}$ | $2.60^{+0.30}_{-0.20}$ | $0.30 \pm 0.20$ | $0.48^{+0.040}_{-0.020}$ | $3929^{+19}_{-953}$ | $41.00 \pm 1.00$ | 197/179 |
| 12172014 | 2019-11-21 | 58808.89 | 1.7 | 5.9 | $2.5^{f}$ | $3.20^{+0.50}_{-0.30}$ | $0.30 \pm 0.10$ | $0.50^{+0.050}_{-0.020}$ | $3507^{+19}_{-1065}$ | $39.00 \pm 1.00$ | 188/181 |
| 12172015 | 2019-11-22 | 58809.29 | 1.4 | 8.0 | $2.5^{f}$ | $3.20^{+0.90}_{-0.50}$ | $0.30 \pm 0.20$ | $0.52^{+0.020}_{-0.020}$ | $3420^{+19}_{-574}$ | $39.00 \pm 1.00$ | 232/190 |
| 12172032 | 2019-12-12 | 58829.54 | 2.1 | 7.7 | $2.5^{f}$ | $3.00^{+2.00}_{-1.00}$ | $0.30^{+0.20}_{-0.20}$ | $0.43^{+0.020}_{-0.030}$ | $3465^{+19}_{-531}$ | $18.90 \pm 0.20$ | 271/275 |
| 12172066 | 2020-01-18 | 58866.61 | 0.7 | 11.1 | $2.5^{f}$ | $2.00^{+0.10}_{-0.10}$ | $0.21^{+0.05}_{-0.04}$ | $0.16^{+0.009}_{-0.009}$ | $36113^{+19}_{-9292}$ | $2.70 \pm 0.20$ | 231/263 |
| 12172077 | 2020-01-31 | 58879.22 | 1.7 | 1.1 | $2.5^{f}$ | $1.67^{+0.05}_{-0.10}$ | $0.60^{+0.30}_{-0.20}$ | $0.10^{f}$ | $11174^{+19}_{-5139}$ | $0.38 \pm 0.01$ | 215/212 |

$^b$ Errors quoted with 68% confidence where a single value is given
$^f$ parameter frozen

## 4.3 Let the fits begin - spectral and temporal analysis

The first step in interpreting the obtained data is the spectral and temporal analysis, as described in earlier chapters. This becomes all the more important in the case of a newly discovered source. The spectra and the lightcurve are the only fresh ingredients available to us with which to prepare and present a delectable theory about its nature and geometry. The spectral and temporal analysis is explained in the following sections.

### 4.3.1 Spectral Analysis

We have already discussed fitting the spectra with phenomenological models in Chapter 1 and its application to 4U 1630-472 in Chapter 3 respectively. We begin with phenomenological fits and then proceed to more complex physical models, as explained earlier. Multiple ATels (Kennea et al., 2019; Thomas et al., 2019, etc.) suggested that the source emits predominantly in the soft X-ray band. In the $0.5 - 10$ keV band - in which *NICER* spectra is obtained - we therefore expect a significant contribution from the multicolor disc blackbody component. The spectrum is first modelled with the *diskbb* model in XSPEC (Mitsuda et al., 1984; Makishima et al., 1986). *TBabs* (Wilms et al., 2000) is used to account for the interstellar absorption with abundance set to wilms with vern cross-section (Verner et al., 1996). Even in such a limited energy range, the spectral modelling resulted in poor fits with $\chi^2_{\rm red} = 1135/578$. A very steep powerlaw is required to account for the residuals above 5 keV giving a much better value of $\chi^2_{\rm red} = 415/576$. A systematic error of 1.5% is added during the spectral fitting (Jana et al., 2021). Residuals below 1 keV are still observed. Although we attempt to model them using variable abundances in iron and oxygen in the interstellar absorption, the fits did not improve significantly. Some instrumental residuals are reported in *NICER* data below 1 keV in previous papers (Alabarta et al., 2020; Fabian et al., 2020, and so on), although, this should not be a significant issue with the updated CALDB. Therefore, we reached out to the *NICER* team for assistance. After going through multiple checks, we conclude that the residuals below 1 keV are probably instrumental in nature and do not affect the fits as they are within the systematic limit of the instrument i.e., a few percent at 1 keV.

However, the powerlaw component seems to contribute significantly in the lower energy range, which is unlikely in the soft state. Therefore, it is clear that phenomenological modelling is not sufficient to interpret the system. The *nthcomp* model is generally used as a replacement for the *powerlaw* model to represent Comptonisation. Here, we convolve the disc with the thermal Comptonisation model *thcomp* (Zdziarski et al., 2020), a more accurate version of *nthcomp*. The parameters are similar to those in *nthcomp* with the addition of a Comptonisa-

tion fraction term ($f_{cov}$). Since the electron plasma temperature ($kT_e$) cannot be constrained, owing to the cut-off energy possibly lying beyond the *NICER* energy range considered, we freeze it to 100 keV. The final model used is *TBabs (thcomp ⊗ diskbb)*. The $n_H$ parameter ranges from $\sim 1-3 \times 10^{20}$ cm$^{-2}$ with most of the values lying between 2 and 3 $\times 10^{20}$ cm$^{-2}$. We, therefore, freeze $n_H$ to an average value of $2.5 \times 10^{20}$ cm$^{-2}$ in cases where it could not be constrained towards the end of the outburst.

The broadband spectra ($0.5-25.0$ keV) from *AstroSat* are also modelled with *TBabs (thcomp ⊗ diskbb)* model as described above. Response is modified for both *SXT* and *LAXPC* spectra using the `gain` command (Singh et al., 2017; Antia et al., 2021) as detailed in Chapter 2. A systematic error of 2.5% is applied to the combined fit (Mukerjee et al., 2020). Residuals around 6 keV were observed with *NuSTAR* (Tomsick et al., 2019), although the presence of reflection could not be stated with certainty. Similarly, positive residuals are observed in the $5-7$ keV range in the energy spectrum obtained with *AstroSat* on 21 November 2019 (ObsId 3328). No such features are seen in the other *AstroSat* observations. To test for evidence of reflection, we replace *thcomp* with the relativistic reflection model *relxillCp* (García et al., 2014; Dauser et al., 2014) which includes a physical Comptonisation continuum. Both models fit the spectrum well with $\chi^2_{red}$ of 476/390 and 478/393, with and without the inclusion of reflection respectively. However, individual parameters in the model could not be constrained. Addition of either a reflection component from the returning radiation or a single-temperature blackbody component, associated with the boundary of the black hole, was required for spectral fits in observations close to this date using *NuSTAR* data in Lazar et al. (2021). We also include a blackbody component (*bbodyrad*) to check for the requirement of such an additional component. This results in poorer fits with $\chi^2_{red} > 2$. Moreover, a few parameters are pegged at their respective limits. Therefore, we fit all the spectra with the model *TBabs (thcomp ⊗ diskbb)*. The *Swift-XRT* spectra in the $0.5-10$ keV range can also be fit using the same model. However, the $n_H$ value could not be constrained and is fixed at $2.5 \times 10^{20}$ cm$^{-2}$.

Figure 4.3 shows the unfolded *NICER* and *AstroSat* spectra fit with the model *TBabs (thcomp ⊗ diskbb)* on the left and right respectively. *NICER* spectra for 6 November 2019 is shown in black and 14 February 2020 in blue, to show the evolution of the spectrum from the soft to hard state. *AstroSat* spectrum from 21 November 2021 is shown in red and black (corresponding to *SXT* and *LAXPC* respectively). The residuals are shown in the bottom panels. The fit parameters using all the instruments are presented in Tables 4.1, 4.2 & 4.3. All errors are quoted at 90% confidence unless stated otherwise.
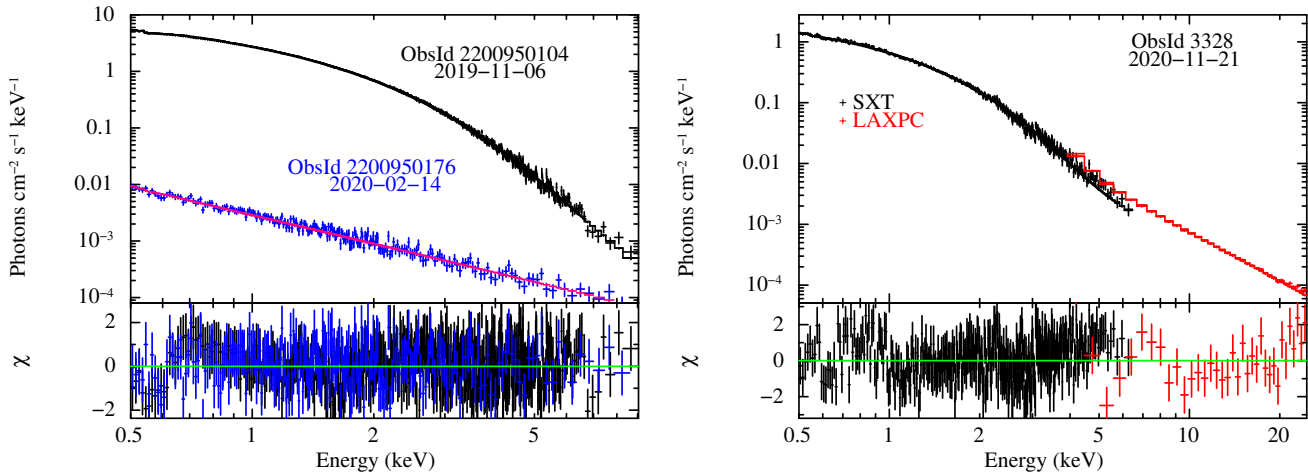
**Figure 4.3:** Unfolded *NICER* and *AstroSat* spectra fit with the model *TBbabs ( thcomp ⊗ diskbb )* are shown in the left and right panels respectively. The spectra on the left are from 6 November 2019 (black) and 14 February 2020 (blue). The spectrum on the right is from 21 November 2019. *SXT* and *LAXPC* data are marked with black and red markers respectively.

### 4.3.2 Temporal Analysis

Not much variability is expected in the lightcurve when the spectrum is dominated by a soft, thermal disc component. To verify this, *NICER* lightcurves in the 0.3–12 keV energy band are generated with a binsize of 5 ms to study the evolution of the temporal properties of the source. PDS is obtained in the rms space using `powspec` command from `XRONOS v6.0`. Lightcurves are divided into intervals of 16384 bins and Poisson noise subtracted PDS is obtained for each interval. Averaging all the PDS in the frequency range 0.01–100 Hz gives the final PDS. Geometric rebinning by a factor of 1.05 is performed. All the *NICER* observations upto MJD 58858 could be modelled by a powerlaw. A significant change in the PDS is observed only when a transition from soft to hard state was reported around 14 January 2020. Band-limited noise is seen during this period in the *NICER* data, which is modelled with zero centred Lorentzian (Figure 4.5). The rms values are computed over the frequency range of 0.01 to 100 Hz (Remillard and McClintock, 2006).

Lightcurves in the 3–25 keV energy band can be obtained with *AstroSat*. However, due to the limited number of observations, we take the *NICER* data as reference and try to append the information obtained with it using the *AstroSat* data. The 3 – 12 keV lightcurves with the same binsize of 5 ms are generated with *LAXPC20*. This band is chosen as the closest approximation to the *NICER* operational energy band. PDS are obtained in the rms space following the procedure detailed above. The first two observations with *AstroSat* could be modelled by a powerlaw. Surprisingly, broad Lorentzian components are required to model

88

the PDS of *LAXPC20* observation of 21 November 2019, where, technically, the source falls in the 'disc-dominant' state. These aspects are discussed in Section 4.4.2.

## 4.4 Keeping up with the evolution

### 4.4.1 Spectral Properties

Energy spectra are modelled with *TBabs (thcomp ⊗ diskbb)* as detailed in Section 4.3.1. The results of the fit are presented in Tables 4.1, 4.2 and 4.3. Sample spectra are presented in Figure 4.3. The $n_H$ parameter is left free and varies from $1.7-2.8$ $\times 10^{20}$ cm$^{-2}$ except for cases where it is fixed at $2.5 \times 10^{20}$ cm$^{-2}$, as mentioned previously. As the outburst progresses, the contribution of the disc component reduces and the spectrum becomes harder. The Compton scattering fraction ($f_{cov}$) increases significantly after 25 January 2020. The energy spectra from 2 February 2020 follow a simple powerlaw distribution. Therefore, it is difficult to constrain the parameters of the *diskbb* component. We fix the temperature at 0.1 keV to perform the fits in this case as shown in Table 4.1. The energy spectrum from 14 February 2020 is shown in the left panel of Figure 4.3 as an example. The evolution in parameters is shown in Figure 4.4. Disc temperature and photon index decrease from 0.58 to $\sim$ 0.1 keV and $\sim$ 4.6 to $\sim$ 1.7, respectively as the source evolves in the decay phase (Table 4.1 and Figure 4.4). The total flux is obtained in the range $0.5-10$ keV for all the observations using the *cflux* command. The parameter $f_{cov}$ acts as a marker for the rise in prominence of the Comptonisation component seen in the fourth panel of Fig 4.4. However, lack of high energy spectra limits the accurate estimation of this parameter. In many cases, a precise estimation of $f_{cov}$ is not possible during the soft states, and therefore, we define the upper limit to be 0.3 and quote the error at 68% confidence (see Tables 4.1, 4.3). The existence of broadband spectra upto 25 keV allows us to obtain better estimates of $f_{cov}$ during *AstroSat* observations. It can be seen from Table 4.2 that $f_{cov}$ is < 0.1 on 8 and 15 November 2019. A slight increase in $f_{cov}$ and low values of $\Gamma$ (2.3-2.6) are seen during *AstroSat* observations, suggesting that the source could have been in an intermediate state. Reflection features are not observed in the spectrum. In the absence of *NICER* data, we also evaluate *Swift-XRT* data to confirm this transition and find that a decrease in $\Gamma$ is noted here as well. However, better constraints on the parameters cannot be obtained due to lack of high energy data. Based on the evolution of spectral parameters, we now divide the outburst into 3 states, i.e., LHS, Intermediate State (IMS) and HSS. The red, purple and yellow patches in Figure 4.4 denote these states. Based on only the *NICER* lightcurve and HR (Figure 4.1), the source seems to have moved to the soft state at the peak of the outburst. However, the addition of *AstroSat* and *Swift-XRT* data
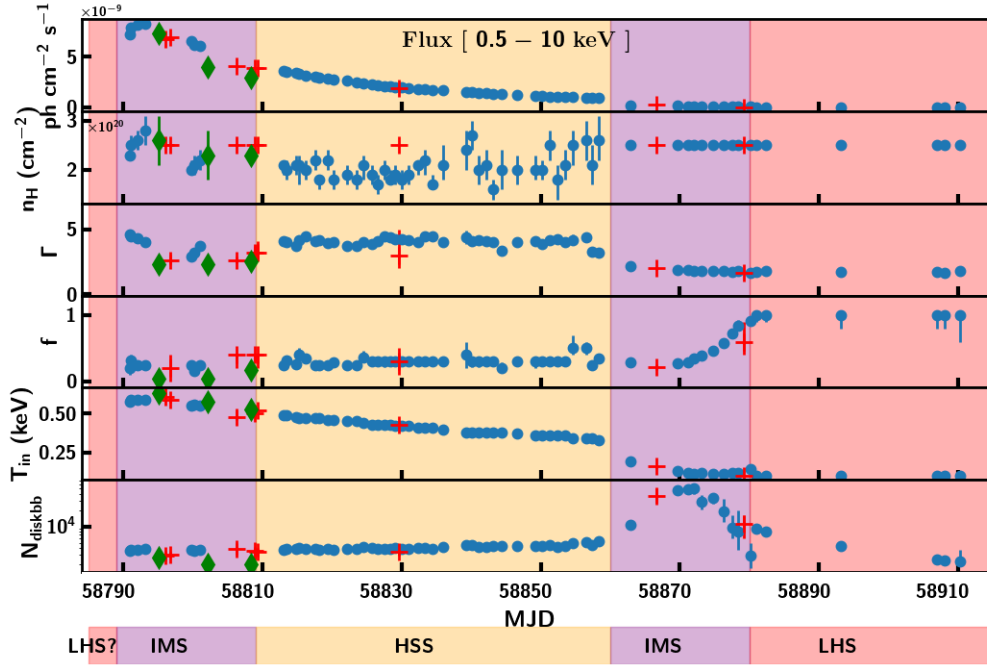
**Figure 4.4:** Evolution of model flux is shown in the top panel. Change in $n_H$, $\Gamma$, $f_{cov}$, $T_{in}$ and $Norm_{diskbb}$ is shown in panels 2 to 6 from the top (see text for description of parameters). The outburst is divided into different states based on the spectro-temporal variation as indicated by the colour bar below the plot. The red, yellow and purple patches correspond to LHS, IMS and HSS respectively.

show a clear dip in $\Gamma$ accompanied by a variation in the value of $f_{cov}$. It seems to imply that the source did not transition to HSS and was still in an intermediate state. Hence, we extend the intermediate state to at least MJD 58809. The source remains in the soft state from MJD 58813 to 58880 and then reaches the canonical hard state, where $f_{cov}$ reaches the upper limit of 1 and a corresponding decrease in $\Gamma$ is seen.

### 4.4.2  Temporal Properties

The top panel of Figure 4.5 shows the PDS obtained from *AstroSat* data on 21 November 2019, when the source is in an intermediate state. An increase in rms values from 11% to 20% is observed using *LAXPC20*, from 8 November to 21 November 2019. An additional broad Lorentzian component is also required to model the PDS obtained on 21 November 2019 with centroid frequency at $\sim 2$ Hz. The PDS also shows a small bump at 0.02 Hz. We attempt to model it using a Lorentzian component. However, as the change in $\chi^2_{red}$ is very small (124/118

to 118/115), we model the PDS using a powerlaw component and a single broad Lorentzian.
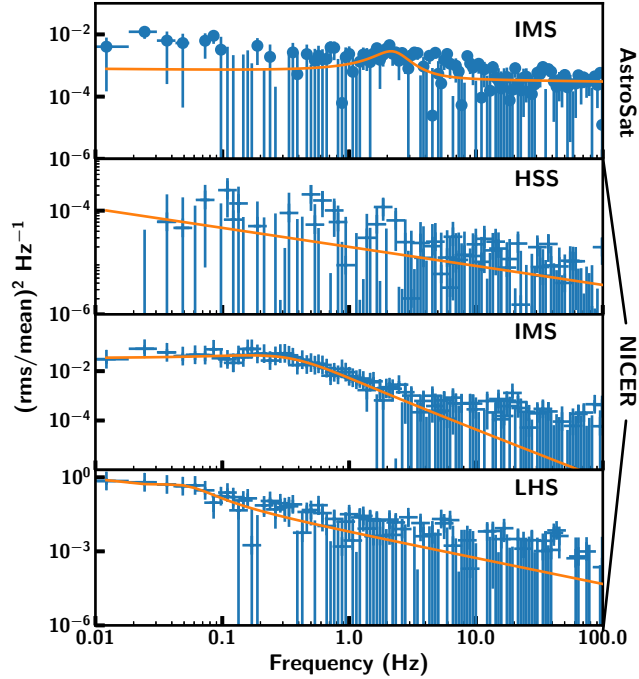


**Figure 4.5:** PDS for source in HSS (*NICER*), IMS (*LAXPC*) and LHS (*NICER*) is shown above. The solid line shows the best fit model consisting of only powerlaw for HSS and a combination of broad Lorentzians and powerlaw for IMS and LHS.

The PDS for all the observations from 3 November to 15 December 2019 using *NICER* exhibit weak red noise, which are modelled with a powerlaw. A sample PDS is shown in the second panel of Figure 4.5 which corresponds to 26 November 2019. The rms remains less than 5% for these observations, typical of a BHB in the HSS (Remillard and McClintock, 2006; Motta et al., 2018; Baby et al., 2020). Band-limited noise (BLN), characteristic of a harder state, is observed in the PDS for the observations with *NICER* after 21 January 2020, modelled by zero centred Lorentzians as shown in third and fourth panels of Figure 4.5. An increase in rms from $18.7 \pm 0.5\%$ on 21 January 2020 to $24 \pm 2\%$ on 30 January 2020 is seen, which is close to the expected rms from BHBs in LHS (Remillard and McClintock, 2006; Nandi et al., 2012; Belloni and Stella, 2014). The rms continues to increase till 3 February 2020 and reaches upto $\sim 30\%$. Although the source remains in a canonical hard state in the following observations, the flux from the

source decreases further, limiting the estimation of rms. The PDS become largely dominated by noise and can be modelled by a powerlaw component.

### 4.5   Scouting out the details on MAXI J0637-430

The X-ray transient MAXI J0637-430 was discovered in November 2019 and was extensively observed during its outburst. Several papers were published with multiple studies on the source. Tetarenko et al. (2021) performed multi-wavelength spectral analysis of X-ray, UV and optical data and suggested that the spectrum can be explained by an irradiated disc and a powerlaw component. Also, assuming standard parameters, the orbital period of the source was likely to be in the range of $2-4$ hrs. Meanwhile, Jana et al. (2021) attempted to classify the outburst into SIMS, HSS, HIMS and HSS based on spectro-temporal analysis using only *NICER* data. Further, the mass of the compact object was proposed to lie between $5-12$ $M_\odot$ at a distance of $< 10$ kpc. Additionally, Lazar et al. (2021) suggested that the spectrum in the soft state is complex and a simple model consisting of a thermal disc and Comptonisation is not sufficient to describe it. One needs to include an additional component accounting for either the emission from the plunging region or reprocessing of the returning disc radiation. Building on these inferences, we attempt a closer look at the source to try and unlock a few more snippets of information.

We first attempt to obtain a lower limit on distance using the normalization of the *diskbb* model ($N_{diskbb}$) resulting from spectral fits to an observation during the disc dominant state. It is defined as $N_{diskbb} = (r_{in}/d_{10})^2 \cos i$, where $r_{in}$ is the apparent inner disc radius, $d_{10}$ is the distance to the source in units of 10 kpc and i is the inclination angle. We use this relation to obtain a lower limit on the distance, considering inclination in the range $5-80°$ (Motta et al., 2018) and mass as 3 $M_\odot$ as the compact object is more likely to be a black hole. The colour to effective temperature ratio ($f_{col}$) is considered to be 1.7 (Shimura and Takahara, 1995). Assuming a non-rotating BH and $N_{diskbb} \sim 3800$, the distance to the source is greater than 2 kpc.

Spin is another fundamental property of the black hole. Generally, the way to estimate spin is by modelling the reflection features. Here, with the existence of so many unknowns, it is difficult to obtain a particular value with certainty. Therefore, we take up an exercise, where we try to obtain the most probable range of spin along with a plausible mass and distance combination. For this, we model the spectrum using relativistic disc model *kerrbb* (Li et al., 2005), with the final model as *TBabs (thcomp ⊗ kerrbb)*. This gives an opportunity to constrain the mass of the compact object with varying inputs of distance and spin. *kerrbb* model can be used when the contribution of the disc to the total flux is more than 70%. Although this criterion is satisfied in all the observations before MJD 58862,
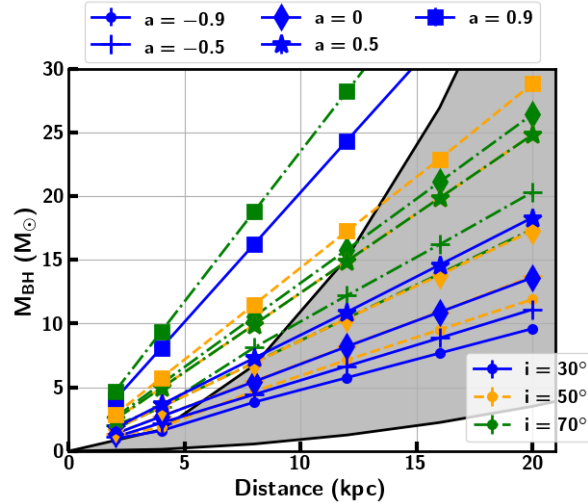
**Figure 4.6:** Mass plotted as a function of distance and inclination is shown in the above figure. Solid, dashed and dotted lines denote inclination angle of 30°, 50° and 70° respectively. Spins ranging from -0.9 to 0.9 are considered in steps as marked above the plot. The grey, shaded region denotes the most probable combination of mass and distance based on transition luminosity.

we choose the observation with the maximum flux on 6 November 2019. As the lower limit of distance is obtained as 2 kpc in the first part of this section, we systematically increase the distance in the broad range 2 to 20 kpc in multiples of 2 and spin from -0.9 to 0.9 (-0.9, -0.5, 0 , 0.5, 0.9) to obtain the mass of the compact object at a fixed spectral hardening factor of 1.7 (Shimura and Takahara, 1995). The variation of mass with distance and spin is presented in Figure 4.6. The inclination angle is frozen in steps of 10° between 30° and 70°. The curves obtained with inclination angles 30°, 50° and 70° are shown in Figure 4.6 for clarity. For inclination angles less than 30°, mass is found to be less than 3 $M_\odot$. Since the aim is to estimate the upper limit on mass with this exercise, we limit ourselves to inclination angles greater than 30°. We also plot mass as a function of distance using the luminosity of the source as it transits from soft to hard state. This transition generally occurs at $1-4$ % of $L_{Edd}$ (Maccarone and Coppi, 2003; Dunn et al., 2010; Tetarenko et al., 2016; Vahdat Motlagh et al., 2019). The shaded region in Figure 4.6, gives the range of mass obtained following this assumption. From the overlap of the shaded region and the distance-mass curves obtained, mass is constrained within $3-19$ $M_\odot$ for distance < 15 kpc with retrograde spin. Mass of the BH is > 20 $M_\odot$ when a non-rotating BH or one with prograde rotation is considered. As mentioned earlier, the orbital period of the system is estimated to be 2–4 hrs (Tetarenko et al., 2021). Such low orbital period Galactic systems are unlikely to contain a BH of mass > 20 $M_\odot$ (Motta et al.,

2018; Jonker et al., 2021). Therefore, we propose that MAXI J0637-430 consists of a BH with mass in range $3 - 19$ M$_\odot$ with retrograde rotation at a distance $<$ 15 kpc.

## 4.6  Similarity with 4U 1630-472? - an investigation

The fast rise and slow decay profile of the lightcurve and an outburst lasting roughly 200 days seems to bear an uncanny resemblance to the 'mini'-outbursts of 4U 1630-47 (Abe et al., 2005; Capitanio et al., 2015; Baby et al., 2021). Moreover, 4U 1630-472 also remains predominantly in the soft states during these 'mini'-outbursts. So one wonders, if these two sources share more than the aforementioned characteristics or do the similarities end there? This question prompted us to examine the lightcurves and the HID more closely. As can be seen from the top panel of Figure 4.1, MAXI J0637-430 brightened to $\sim 90$ mCrab within 2 days of its detection. Thereafter, a gradual decay is seen for the next $\sim 25$ days. The source remained faint for the rest of the outburst, eventually reaching quiescence towards the end of April (not shown in the plot). The second panel shows the *NICER* lightcurve binned by 100 s for clarity. HR is also obtained from *NICER*, defined as the ratio of counts in the $2 - 10$ keV band to the counts in $0.5 - 2$ keV band. HR shows a slight rise towards the beginning of the outburst and then dips lower than 0.1. The source then remained in soft state till MJD 58858. An evident rise in HR is seen after MJD 58858 till MJD 58880, where the HR reaches 0.4 and remains constant. Although a clear transition from soft to a harder state is seen at MJD 58858, it is difficult to exactly isolate and mark the intermediate states based on this information alone.

At this point we turn to the HID obtained with *NICER* to examine the existence of state transitions, if any. We plot the HID using *NICER* in Figure 4.7. The unabsorbed model flux obtained from fitting *NICER* spectra in the $0.5 - 10$ keV range is plotted against the hardness ratio i.e. the ratio of flux in the $2 - 10$ keV to $0.5 - 2$ keV energy bands. The source traces a 'c' shaped profile in the HID. However, *NICER* data is available only from 3 November 2019. We, therefore, use *MAXI* data available before this date to obtain a complete picture of evolution of the HID. The HID traces out the path marked by arrows from points 1 to 5 (Figure 4.7). Crab spectrum from *MAXI* is accumulated within the duration of the observations used here (MJD 58790–58910) using *MAXI* on-demand process[5]. The correlation factor between the flux in the $2 - 10$ keV range and count rate is calculated. This number is then used to correlate the count rate and flux in $2 - 10$ keV in MAXI J0637-430 on 2 November 2019 in Crab units. Total flux is obtained by extrapolating the response to lower energies. Similar procedure is

---

[5]http://maxi.riken.jp/mxondem/
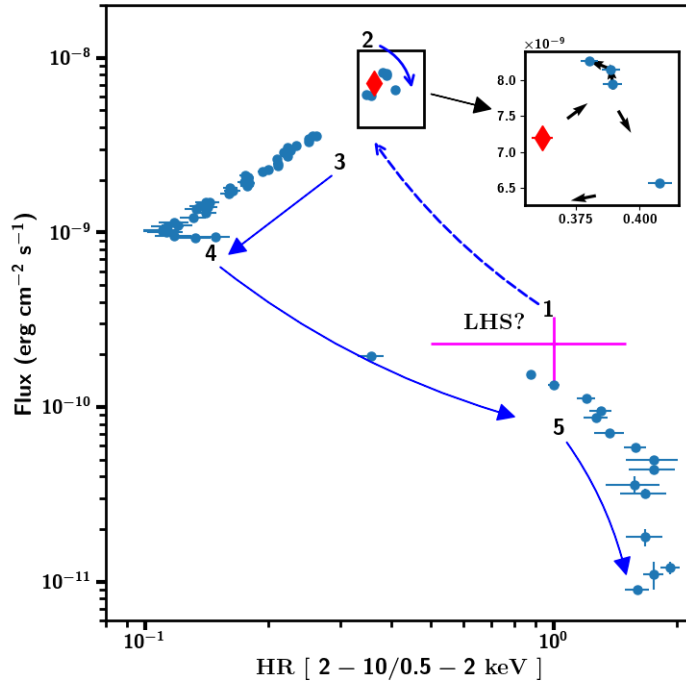
**Figure 4.7:** Flux in the $0.5 - 10$ keV is plotted against HR. HR is defined as ratio between model flux in $2 - 10$ keV and $0.5 - 2$ keV. The evolution of HID is shown with arrows. The magenta cross marks the approximate beginning of the outburst obtained with *MAXI* spectrum normalized using Crab counts (see text for details). The rectangular patch represents the probable intermediate state. A zoomed in version of the patch is also shown to highlight the direction of evolution of source in this duration. The red diamond denotes the first observation with *NICER*.

used to obtain flux in the $0.5 - 2$ keV band. The error bars take into account the errors in the Crab flux and the errors in the model flux using error propagation method. We also consider a variation of $3\sigma$ in the conversion factor, which is larger than the error obtained using the error propagation method. However, this point is taken only as a reference as the calibration difference between the instruments is not considered. Therefore, the evolution from points 1 to 2 is marked as a dotted line denoting the possible path. Solid arrows from the points 2 through 5 show the evolution of the source as seen using *NICER*. Interestingly, the source seems to follow a loop within the rectangle at point 2 before moving to a possible bright, intermediate state. This is emphasized in the inset of Figure 4.7. The arrows show the direction of evolution. The red diamond denotes the first observation with *NICER*. The HR decreases from 0.5 to 0.1 (point 3 to 4) where the source is in the HSS. Then the source moves to the LHS, where a sudden increase in HR

is seen (0.1 to 0.8) and flux is reduced by an order ($10^{-8}$ to $10^{-9}$ erg cm$^{-2}$ s$^{-1}$) (point 4 to 5). Therefore, faint traces of an intermediate state can be found in the area enclosed by the rectangular box. This suggests that the source exhibited atleast two transitions during the outburst - Intermediate state (IMS) to HSS, HSS to LHS with a hint of a possible LHS to IMS transition at the beginning of the outburst.

Interestingly, this source also seems to track out a distinctive 'c' in the HID (see Figure 4.7) with a circular knot at the top instead of the 'q'-shaped HID expected during a canonical outburst. A similar profile was seen for the BHB 4U 1630-472 (Baby et al., 2020), which is presented in Figure 3.6 of Chapter 3. The initial transition from hard to soft state in 4U 1630-472 source would have been entirely missed, were it not for the serendipitous observation of *AstroSat* scheduled on the very same day as the start of the 2016 outburst. Detailed discussions are presented in Chapter 3. A similar fast transition could have occurred in this case too. *NICER* observations exist only after 2 November 2019; so do the observations with all other pointed instruments. The *MAXI* data point (magenta cross) plotted in Figure 4.7, even with the large error bars, suggests that the source was in the hard state for a very short duration at the beginning of the outburst. A quick transition from hard to disc dominant state could have occurred within the time span of a few hours on 2 November 2019 or even earlier. Additionally, the existence of an intermediate state can be inferred at the beginning of the outburst based on the spectral characteristics, although a clear distinction from the soft state is difficult to observe in the absence of broadband spectra. Hence it is not surprising that earlier studies classify the source as being in the soft state for most of the duration of the outburst (Tetarenko et al., 2021; Jana et al., 2021; Lazar et al., 2021). Lower values of $\Gamma$ and a slight increase in rms were reported for observations with *Swift+NuSTAR* from MJD 58801 to 58812 (Lazar et al., 2021). The gulf between these two supposedly contrasting conclusions can be filled by including the *AstroSat* observations. This is the missing piece of the puzzle that brings the entire picture into focus. The analysis in both Lazar et al. (2021) and this work, taken together, suggest that the source was not in a canonical soft state at the beginning of the outburst. Due to the availability of broadband spectra from *AstroSat*, where $\Gamma$ and f$_{\mathrm{cov}}$ are better constrained, it can be stated that the source undergoes transition to an intermediate state lasting for a few days before going to the soft state. A similar transition to an IMS was also postulated for 4U 1630-472 at the corresponding stage of evolution of the source in the HID. Random variation in spectral parameters in this duration (MJD 58790 to MJD 58809) is also seen (Tables 4.1, 4.2, 4.3 and Figure 4.4), which is also a testimony to the fact that the source was in an intermediate state .

Based on the available information, we divide the source into LHS, IMS and HSS, which are marked in Figure 4.4 as red, purple and yellow patches. A similar

classification was attempted for 4U 1630-472 as discussed in Chapter 3.

## 4.7 A few more inferences...

Tracing the evolution of the source, from the first report of an outburst to eventual quiescence, yields a lot of information about the source. Before commenting on the possible accretion geometry of the source, a specific point requires attention. In all the analysis performed, the presence of a reflection component has remained a mystery. Residuals at $5-7$ keV range were observed, both with *NuSTAR* (Lazar et al., 2021) and *AstroSat*. However, we remain sceptical of its origin in reflection process, as do Lazar et al. (2021). Reasonably good fits are obtained with *relxillCp* model as discussed in Section 4.3.1. However, clear positive residuals in the $5-7$ keV range are seen only in the spectrum from MJD 58808.28. Detailed inferences from just a solitary observation can be unreliable. Therefore, we refrain from commenting on the reflection features. We discuss the spectral and temporal properties only in the context of evolution of the accretion disc and a Comptonisation component.
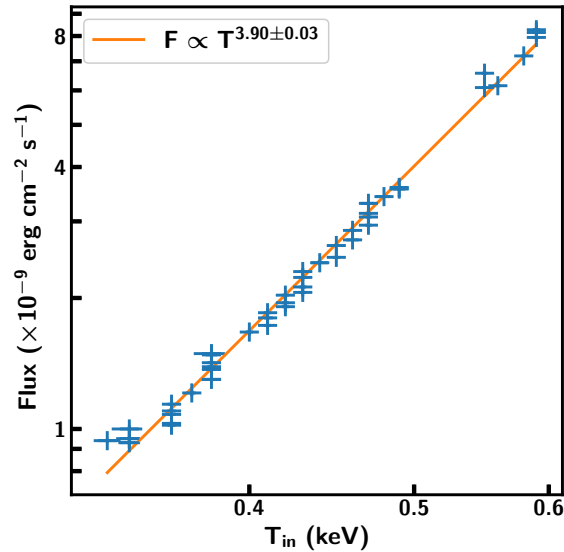


**Figure 4.8:** The model flux in the $0.5-10$ keV band is plotted against the disc temperature. The solid line shows the best fit. The equation obtained from the fit is given in the top right.

The rapid fluctuations in spectral parameters (within hours or a few days) can be associated with the changes in the disc during a predominantly soft state where the assumption of a standard Shakura-Sunyaev disc (Shakura and Sunyaev, 1973)

breaks down. Such deviations are expected at the beginning and end of disc-dominated states or intermediate states which can be explained by a moving disc or change in colour correction factor ($f_{col}$) as disc fraction decreases (Dunn et al., 2011), corresponding to a change in degree of ionization in the disc. Simply put, the disc no longer follows the standard picture. To check for deviations from the standard picture during the soft state, we plot the disc temperature vs. flux in Figure 4.8. The solid line shows the best fit relation between the two parameters ($T_{in}$ and F) as $F \propto T^{3.90\pm0.03}$. This is clearly close to the standard relation of $F \propto T^4$ expected of SS discs. It suggests that the source evolved to the canonical HSS quickly, which is unlikely, if it is driven only by the disc accretion. Such a scenario in 4U 1630-472 is explained by Capitanio et al. (2015) by invoking an external perturbation that triggers a rise in disc temperature, independent of the disc accretion rate. The results obtained so far suggest that the physical mechanism underlying the origin of outbursts for MAXI J0637-430 and 4U 1630-472 could be similar. However, further inferences cannot be made unless extensive broadband observations of the sources are performed for the subsequent outbursts and recurrence times are closely monitored.

## 4.8  In a nutshell

- MAXI J0637-430 is a new X-ray transient which went into outburst on 2 November 2019. Outburst lasted for roughly 200 days.

- The source remained in the soft state for most of initial bright phase of the outburst.

- We classify the outburst into LHS, IMS and HSS based on HID and spectro-temporal properties.

- The HID follows a 'c' shaped profile similar to 4U 1630-472. Lack of initial bright hard states and presence of an intermediate state in a predominantly disc dominant state are further similarities observed with the source.

- Physical modelling suggests that the source consists of a black hole with retrograde spin and mass $< 19$ $M_\odot$ at a distance less than 15 kpc.

# Chapter 5

# Understanding the accretion geometry of Swift J1753.5-0127

In the previous chapters, we have dealt with transient BHB sources which undergo outbursts lasting for around a hundred days. Another common thread that connects the previous two sources is that they emit mostly in the soft X-ray region. Transitions to hard states seem to occur very late or not at all. Now we visit the curious case of a BHB source, which would be on the other end of this peculiarity spectrum. Swift J1753.5-0127 has only undergone one outburst in its observable lifetime, and that too, one that lasted for a whopping twelve years! Also, this source emitted mostly in the hard X-ray region, even at its brightest. So, this is one example of a source which seems to have undergone a so-called "failed" outburst. The questions that we attempt to answer in this chapter are as follows (a) What is the physical mechanism which could facilitate such an outburst? and (b) How does the truncated disc geometry hold up in such a scenario?

The answers for these two questions have to be arrived at using spectro-temporal analysis. However, as we have seen in the earlier chapters, spectral modelling by itself cannot provide a concrete answer, as the same spectrum can be satisfactorily fit with multiple models giving rise to spectral degeneracy. One model cannot be chosen over the other based on spectral analysis alone. A correlated spectro-temporal analysis can provide a way out of this degeneracy. Although many methods exist, here we explore Frequency Resolved Spectroscopy (FRS) to achieve the same. Before getting into the details of the methodology, we begin by presenting a brief introduction to the source - Swift J1753.5-0127.

### 5.1 Swift J1753.5-0127 : The one that lasted 12 years!

Swift J1753.5-0127 is a BHB discovered by *Burst Alert Telescope (BAT)* (Barthelmy et al., 2005) onboard *Neil Gehrels Swift Observatory* in May 2005 (Palmer et al., 2005), which remained in outburst for a period of $\sim$ 12 years from May 2005 to April 2017 (Shaw et al., 2016c). Another distinctive feature of the source is the occurrence of re-brightening or mini-outbursts from January to April 2017 (Bright et al., 2017; Tomsick et al., 2017; Bernardini et al., 2017). Multiple studies have been performed on this source in an effort to determine its physical characteristics. A lower limit of mass of the compact object is placed at 7.4 $M_\odot$ using the double-peaked hydrogen emission lines in the optical spectrum (Shaw et al., 2016b). The source is one of the few systems with an orbital period < 5 hr ($P_{orb}$ = 3.2 h) (Zurita et al., 2008). Although the source is considered to be at an inclination $\leq$ 55° (Froning et al., 2014; Shaw et al., 2016b), a precise measurement of inclination and distance is not available. During the main outburst, the source reached a peak flux of 200 mCrab within a week of its detection, as observed by *RXTE*, and then decreased within a few months to 20 mCrab. It remained constant at this flux for most of the duration of the outburst, with a few intermittent bursts, where transition to HIMS or soft states was seen and reported (Shaw et al., 2016a). However, during the Fast Rise and Exponential Decay (FRED) profile observed at the beginning of the outburst, the source was found to remain in the LHS, thus being classified as a Low Hard X-ray transient (LHXT) initially (Ramadevi and Seetha, 2007; Zhang et al., 2007). The presence of a soft excess in the spectra, while the source is apparently in the LHS, has intrigued many astronomers. Multiple explanations have been put forward to explain the same. Some studies claim that this points to the existence of a stable disc even in the LHS as opposed to the widely accepted disc truncation theory (for e.g., Ramadevi and Seetha, 2007). Others claim that the physical properties of the source are compatible with the presence of a fully irradiated disc truncated at large radii (Shaw et al., 2019). This is done by investigating the emission mechanisms during the re-brightenings or mini-outbursts (Shaw et al., 2019). One way to ascertain the actual geometry of the source is to study the origin of the LFQPOs seen in the power density spectra.

Several models describing the origin of QPOs are described in Chapter 1. Without going into the specifics of each model, we attempt to obtain a general picture of the accretion disc geometry. QPO origin theories can be divided into two broad categories. The first is due to instabilities in the transition layer where Keplerian flow from accretion disc meets the sub-Keplerian flow close to compact object (Titarchuk and Fiorito, 2004) and the second one is due to geometrical effects i.e., relativistic precession of the radially extended hot inner flow (Ingram et al., 2009). In either case, if we find a way to isolate the spectrum of this variability, it would help in determining the components which participate in it. This in turn

would help us determine the accretion geometry of the source, by comparing the QPO spectrum with the time averaged spectrum. This source serves as an ideal candidate to conduct this study as LFQPOs are observed throughout the decay phase of the outburst. In this work, we isolate the QPO spectra using FRS.

## 5.2   Digging through the archives - Observation and reduction
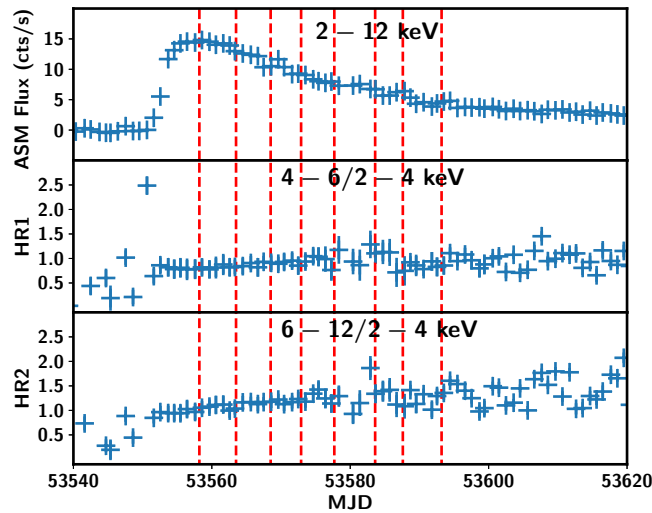


**Figure 5.1:** *ASM* lightcurve of the outburst from 19 June 2005 to 09 September 2005 in the energy band $2 - 12$ keV is plotted in the top panel. Hardness ratios HR1 is defined as ratio of counts in band B to band A and HR2 is defined as ratio of counts in band C to band A. Their variation with time is shown in the next two panels. The red dashed lines represent the observations chosen for analysis.

A unique requirement to perform FRS, is the availability of data with good spectral and temporal resolution. The only pointed instrument, which monitored the source for most of the duration of its long outburst, with good spectral and timing resolution, was *PCA* onboard *RXTE*. However, *PCA* data in different modes is binned on-board for better statistics. This results in a loss of information from channels at lower energy, which are usually binned together. Therefore, we first have to sift through the available data to choose data sets where energy channels are not binned together in bulk. Secondly, we also need to choose observations where the LFQPO is prominently seen. *RXTE* observed the source for a total of 344 times from the beginning of its outburst on 2 July 2005 to 29 November 2011. Of these 344 observations, Type C QPOs are observed in 46 observations, most of them at the beginning of the outburst. A majority of the observations performed with the proposal ID P91423 could be used to perform FRS studies

using both event and binned data. The *ASM* lightcurve of the source from 19 June to 9 September 2005 in $2-12$ keV energy band is shown in the top panel of Figure 5.1.

Lightcurves obtained in three energy bands i.e. A : $2-4$, B : $4-6$ and C : $4-12$ keV are used to generate the hardness ratios HR1 and HR2, where HR1 is defined as ratio of counts in band B to A and HR2 as ratio of counts in band C to A. These are plotted in the second and third panels of Figure 5.1. HR values remain fairly stable upto MJD 53600. HR2 seems to increase slightly beyond MJD 53600 as seen from panel 3. As significant evolution is not observed and state transitions are not reported, we choose eight observations (out of 30 observations where QPOs are reported in P91423), to generate QPO spectra. The observations are chosen such that they are separated by a time interval of $\sim 5$ days. These are marked as dashed vertical lines in Figure 5.1. We use Standard-2 files to generate the time averaged spectra from *PCA* data in the $3-25$ keV energy band. Event mode data files are used to generate the dead-time corrected lightcurves with a bin time of 8 ms. We use only PCU2 data for both the spectral and light curve extraction. Standard procedures are used to extract *HEXTE* data to obtain the energy spectra from $25-150$ keV. Only Cluster B is used as Cluster A had stopped rocking at that point. The details of the observations are given in Table 5.1.

## 5.3 Time averaged spectral analysis

We obtained the time averaged spectra for the eight observations listed in Table 5.1 with *PCA* and *HEXTE* from $3-25$ keV and $20-150$ keV respectively. We first fit the broadband spectrum with phenomenological models. Considering that the source is in the LHS, we fit the spectrum using a power law model along with *TBabs* (Wilms et al., 2000) to account for the interstellar absorption. The abundance is set at `wilm` with `vern` cross-section. The $N_H$ value could not be constrained and is frozen at $2 \times 10^{21}$ cm$^{-2}$ (Cadolle Bel et al., 2007). A simple powerlaw could not fit the spectrum and hence is replaced by a cut-off powerlaw. However, significant residuals are seen at lower energy, which required the addition of *diskbb* (Mitsuda et al., 1984; Makishima et al., 1986) model. A *gaussian* was included to account for residuals seen around 6 keV. This resulted in good fits with $\chi^2_{\mathrm{red}} = 81/80$. A normalization constant is also included to account for calibration difference in both instruments. To obtain a better understanding of the geometry of the system, we replace the *powerlaw* model with *nthcomp* (Zdziarski et al., 1996; Życki et al., 1999), which considers the Comptonisation of the disc photons by hotter electrons. The final model used is *Tbabs(diskbb+gaussian+nthcomp)*.

The fit parameters are given in Table 5.1. The temperature of the seed photons ($kT_{bb}$) is tied to the disc temperature where we consider the seed photons to originate from the disc. As the source was found to be in a hard state, we also
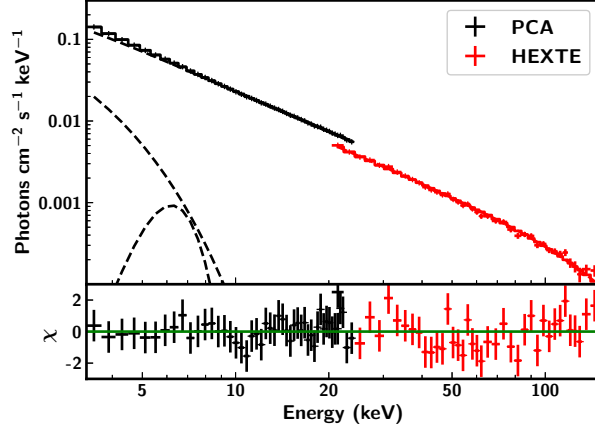
**Figure 5.2:** Unfolded broadband spectrum of ObsId 91423-01-02-05 is fit with model *TBabs (diskbb+gaussian+nthComp)*. *PCA* and *HEXTE* data is plotted in black and red markers respectively. Residuals are shown in the bottom panel.

attempt to replace *diskbb* with other Comptonisation models like *compTT*. Although the fits are satisfactory, with a $\chi^2_{\mathrm{red}}$ value of 73/77, the parameters of the model could not be constrained. Therefore, it cannot be determined if this is a viable replacement for the *diskbb* model. Hence, we fit all the available observations with *TBabs(diskbb+gaussian+nthcomp)* model as described above. We would also like to emphasize that the normalisation of the disc component could not be constrained in some cases. This is probably due to the absence of low energy spectra $(0.1-3\,\mathrm{keV})$, where the thermal disc is likely to be prominent. A sample spectrum of ObsId 91423-01-02-05 fit with this model is shown in Figure 5.2. The *PCA* and *HEXTE* data are plotted with black and red markers respectively. The residuals are plotted in the bottom panel.

## 5.4 Lightcurve, HID and temporal evolution

Swift J1753.5-0127 was in outburst from May 2005 to April 2017. *ASM* lightcurve of the source, plotted in the top panel of Figure 5.1, clearly shows a FRED profile. This profile was observed at the beginning of the outburst, which lasted for a few months. The HR values also remain fairly stable throughout this duration, where the source was mostly found to be in the LHS. The eight observations chosen for FRS studies are represented by the red, vertical dashed lines. HR1 remains almost constant, while a slight variation is seen in HR2. There seems to be a sudden rise in HR1 at the beginning of the outburst, with no corresponding change in HR2. HR2 varies significantly only beyond MJD 53600.
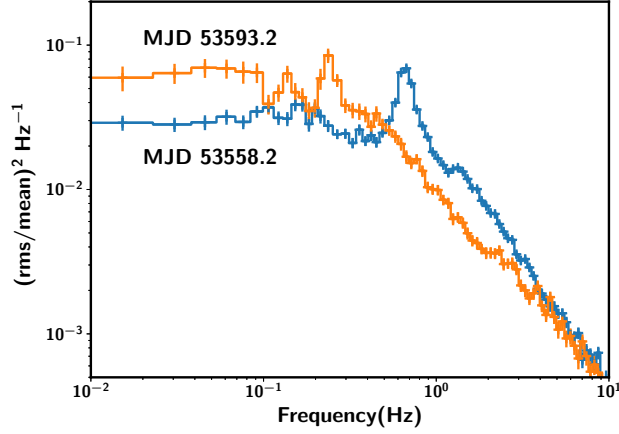
**Figure 5.3:** PDS of first and eighth observations (MJD 53558.2 and 53593.2) are plotted in blue and orange markers respectively. The centroid frequency of the QPO decreases from first to last observation.

PDS are generated for all the eight observations using a bin time of 8 ms and 8192 bins per intervals. The PDS for the first and last of the observations considered are plotted in Figure 5.3. A strong QPO is observed in all the cases varying from $0.2 - 0.7$ Hz along with a Band Limited Noise (BLN) component. The QPO frequency decreases with time as seen in Figure 5.3. A harmonic is also seen from $1.2 - 1.4$ Hz at the beginning which later disappears. A sub-harmonic is seen in the last observation on MJD 53593.2 at $\sim 0.13$ Hz.

## 5.5 Isolating the temporal features using frequency resolved spectroscopy

To generate frequency resolved spectra of the QPOs, we choose the event and binned mode data files with a timing resolution greater than 5 ms. We check for the data grouping using TEVTB2 keyword in the header file to ensure that channels corresponding to $8 - 13$ keV are not binned together. We follow Sobolewska and Życki (2006); Axelsson et al. (2014); Axelsson and Done (2016) to obtain the QPO rms spectra for all the eight observations considered.The details are given in Section 2.5. The final *.pha* file generated is then loaded into *XSPEC* along with response files generated for *std2f* files.

### 5.5.1 QPO Energy spectra vs Time averaged spectra

Low frequency QPOs were observed in the PDS throughout the exponential decay of the outburst. Here, we obtain the energy spectra, corresponding to the variability in the frequency range where the QPO is observed. We could fit the

104

spectra with an absorbed Comptonisation component in all the cases. The final model used was *TBabs\*nthComp*. There was no signature of a soft disc or a reflection component in the QPO rms spectrum. The temperature of the input seed photons could not be constrained due to statistical limitations. Therefore, we freeze the temperature to the one obtained from fitting the corresponding time-averaged spectrum. The origin of the Comptonised photons is assumed to be from the disc. The electron plasma temperature also could not be constrained for a few observations as shown in Table 5.1. Therefore, it was frozen to the values obtained using fits from time-averaged spectra.The QPO rms spectrum is shown along with the time averaged spectrum of ObsId 91423-01-02-05 in Figure 5.4. Results of fits with the model *TBabs(diskbb+gaussian+nthcomp)* along with fits to QPO spectra are presented in Table 5.1.

**Table 5.1:** All the eight time averaged spectra are fit using the model TBabs (diskbb+gaussian+nthComp) and the details are presented. The QPO spectra could be fit only using the nthComp model. The fit parameters for the corresponding QPO spectra are also presented.

| ObsId | MJD | $T_{in}$ (keV) | $\Gamma$ | $kT_e$ (keV) | $E_{line}$ (keV) | Eq. width (eV) | $\sigma$ | $N_{gauss}^a$ | $F_{3-25}^b$ erg cm$^{-2}$ s$^{-1}$ | $\chi^2$/dof |
|---|---|---|---|---|---|---|---|---|---|---|
| 91423-01-01-00 | 53558.2 | $0.84^{+0.03}_{-0.02}$ | $1.69^{+0.01}_{-0.01}$ | $54^{+5}_{-5}$ | $6.2^l$ | 76±3 | 0.9±0.3 | 4.3±0.2 | 8.39±0.08 | 72/80 |
| QPO | | | $1.64^{+0.04}_{-0.04}$ | | | | | | | |
| 91423-01-02-05 | 53563.5 | $0.88^{+0.04}_{-0.03}$ | $1.68^{+0.01}_{-0.01}$ | $54^{+7}_{-10}$ | $6.9^l$ | 74±4 | 1.0±0.5 | 3.8±0.9 | 7.43±0.02 | 66/80 |
| QPO | | | $1.1^{+0.5}_{-0.3}$ | | | | | | | |
| 91423-01-03-02 | 53568.5 | $1.01^{+0.03}_{-0.03}$ | $1.65^{+0.01}_{-0.01}$ | $55^{+7}_{-10}$ | $6.9^l$ | 47±2 | 0.6±0.4 | 1.6±0.4 | 6.36±0.02 | 51/80 |
| QPO | | | $1.0^{+0.4}_{-0.2}$ | | | | | | | |
| 91423-01-03-06 | 53572.9 | $0.96^{+0.04}_{-0.03}$ | $1.64^{+0.01}_{-0.01}$ | $63^{+13}_{-24}$ | $6.9^l$ | 40 ± 6 | 0.6±0.4 | 1.3±0.4 | 5.74±0.01 | 66/80 |
| QPO | | | $1.1^{+0.2}_{-0.7}$ | | | | | | | |
| 91423-01-04-04 | 53577.7 | $0.99^{+0.03}_{-0.03}$ | $1.62^{+0.01}_{-0.01}$ | $49^{+6}_{-8}$ | $6.9^l$ | 67±8 | 1.1±0.5 | 2.1±0.4 | 4.96±0.01 | 79/80 |
| QPO | | | $1.1^{+0.2}_{-0.3}$ | | | | | | | |
| 91423-01-05-01 | 53583.6 | $0.98^{+0.02}_{-0.04}$ | $1.61^{+0.01}_{-0.01}$ | $59^{+8}_{-14}$ | $6.2^l$ | 69±2 | 0.9±0.5 | 1.7±0.1 | 4.14±0.08 | 57/80 |
| QPO | | | $1.1^{+0.1}_{-0.1}$ | | | | | | | |
| 91423-01-06-00 | 53587.6 | $0.92^{+0.05}_{-0.04}$ | $1.59^{+0.01}_{-0.01}$ | $54^{+8}_{-12}$ | $6.2^l$ | 100±3 | 1.0±0.2 | 2.2±0.3 | 3.58±0.01 | 61/80 |
| QPO | | | $1.0^{+0.5}_{-0.2}$ | | | | | | | |
| 91423-01-06-03 | 53593.2 | $0.84^{+0.06}_{-0.04}$ | $1.59^{+0.01}_{-0.01}$ | $82^{+32}_{-22}$ | $6.2^l$ | 58±3 | 0.6±0.4 | 1.6±0.5 | 2.95±0.02 | 91/80 |
| QPO | | | $1.26^{+0.07}_{-0.06}$ | | | | | | | |

$^l$–upper limit

$^a$–in units of $10^{-3}$

$^b$–Flux is in units of $10^{-9}$ erg cm$^{-2}$ s$^{-1}$
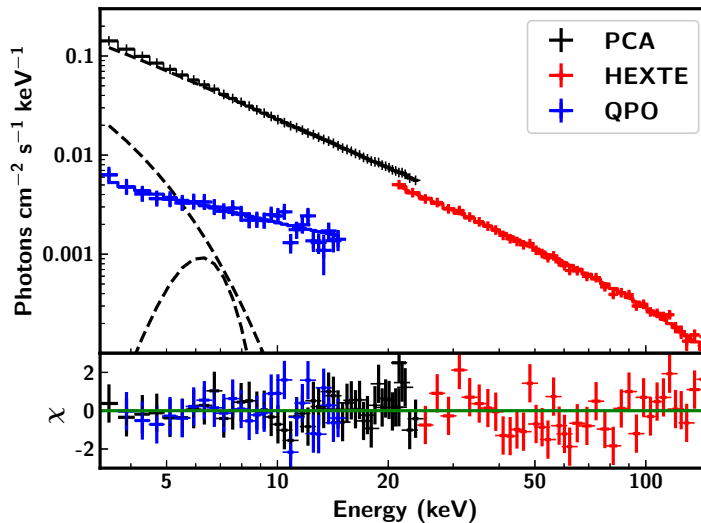
**Figure 5.4:** The time averaged spectrum is plotted with QPO rms spectrum for the ObsId 91423-01-02-05. The QPO rms spectrum is fit with an absorbed Comptonisation model and is scaled up for clarity. The QPO spectrum and residuals are shown in blue markers.

As the source moves to the faint-hard state, the time-averaged spectra become harder, while the disc temperature shows a slight increase from 0.84 to 1.01 keV within 10 days and again reduces to 0.84 keV. No discernible pattern is seen in the equivalent width of the *gaussian*. The fit results for the QPO spectra are also shown in Table 5.1 for comparison. The photon indices obtained for the QPO rms spectra are harder than those for the time-averaged spectra. However, the errors on the values are statistically limited.

To further probe the evolution of QPO spectra with respect to the time-averaged spectra, we plot the ratio of QPO rms spectra to the total spectra in Figure 5.5. The counts have been normalized to 1 at 5 keV for clarity (Axelsson and Done, 2016). Although Figure 5.5 suggests that the QPO rms spectra become harder as the source moves toward the faint-LHS, not much evolution is seen in the QPO spectra between observations separated by a duration of 40 days. It is also observed that the QPO spectra are harder than the time-averaged spectra in all cases.

## 5.6  Existence of a disc in the hard state?

Swift J1753.5-0127 has exhibited many peculiarities from the time of its detection. It underwent an unusually long period outburst for a source with small orbital period ($P_{orb} = 3.4$ hrs) (Zurita et al., 2008). Observation of mini-outbursts is also
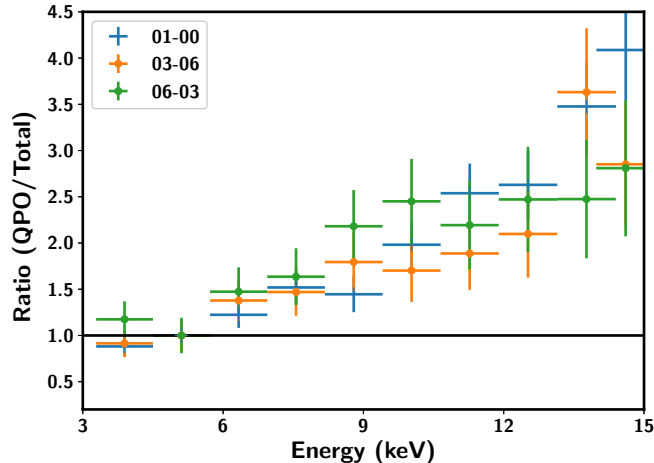
**Figure 5.5:** The ratio of QPO rms spectrum to the total spectrum for three observations is shown in the figure. QPO spectra are always harder than the time averaged spectra. The data is rebinned and counts are normalized at to 1 at 5 keV for a clearer representation.

reported towards the end of the main outburst (Shaw et al., 2016a). Although classified to be in the hard state, a soft excess at the lower energy range was observed in most of the cases, supporting the existence of disc even in the LHS. We therefore perform variability studies of the source to comment on its dynamic nature. FRS technique allows us to isolate and localize regions of fast variability and study the spectrum in detail. We study the QPO spectrum in an effort to localize the origin of this variability.

A canonical outburst typically follows LHS→ HIMS → SIMS→ HSS→ SIMS →HIMS → LHS path, tracing out a 'q'- shaped diagram in the HID. However, state transitions were not reported for the source during its main outburst as it remained only in the LHS. Hence, this outburst is termed as a 'failed' outburst. To probe further, we generate the HID using the model dependent flux obtained from spectral fits. Flux is obtained in the energy bands $2 - 6$ keV and $6 - 12$ keV. The ratio of the flux between the hard and soft bands is plotted against the total flux as seen in Figure 5.6. The source moves from the top left to bottom right during the decay in the main outburst with very less variation in the hardness ratio. It is clear that the source does not follow the 'q'-shaped profile. A few soft X-ray transients seem to follow a 'c' shaped profile in the HID like 4U 1630-472 (Capitanio et al., 2015; Baby et al., 2020) and MAXI J0637-430 (Baby et al., 2021). Although, data presented here is insufficient to draw such a conclusion, it is possible that the source could have evolved to follow a similar profile here. It is also possible that the source transitioned to a soft state briefly (lasting for
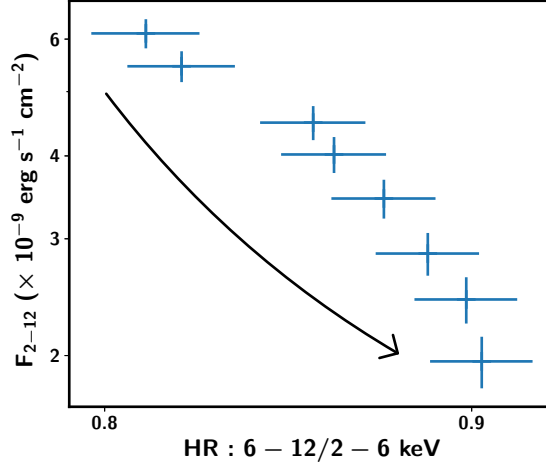
**Figure 5.6:** HID obtained from *RXTE/PCA* is shown in the figure. The source moves from the top left to the bottom right of the HID. The direction of evolution is marked with an arrow. As the source remains in hard state, slight increase in HR from 0.8 to 0.9 is seen from the peak to decay.

a few hours), which was missed by the *RXTE/PCA* instrument. Fast transitions have also been reported at the beginning of the outburst of 4U 1630-472 from the hard to soft state using *SXT* onboard *AstroSat* (Baby et al., 2020), after which it follows a similar profile as in Figure 5.6. Lack of observations at the beginning of the outburst makes it difficult to ascertain if such a transition occurred in this source. However, the similarities in the evolutionary track of the HID followed by soft and hard X-ray transients are suggestive of a common mechanism at play. Definitive comments on this aspect require a grouping studies considering all such sources, which will be undertaken later.

Similar to earlier studies (Ramadevi and Seetha, 2007; Zhang et al., 2007; Shaw et al., 2016a; Kajava et al., 2016; Shaw et al., 2019, etc.), we find that a disc component is required to model the spectra from the hard state. This was explained either by a disc extending close to the innermost stable circular orbit (ISCO) (Ramadevi and Seetha, 2007) or an irradiated disc truncated at large radii, where a large fraction of X-rays is reprocessed in the outer disc and the source of irradiation is produced in the corona within the truncation radius (Shaw et al., 2019). Kajava et al. (2016) suggests that the source of seed photons is synchrotron self Comptonisation below a critical flux limit, which conforms to the truncated disc scenario, but fails to explain the constant soft excess seen in the spectra. We also observe that the inclusion of a soft Comptonisation component, instead of a thermal disc, can also fit the spectra satisfactorily. However, the parameters corresponding to this component could not be constrained. This makes it difficult

to comment on the origin of the soft Comptonisation component. Nevertheless, the existence of an in-homogeneous corona cannot be ruled out. Changes in the disc temperature and equivalent width of reflection line are too small to suggest a significant change in the accretion disc geometry (see Table 5.1). This is consistent with a physical scenario where the accretion disc remains stable throughout the outburst with spectral and temporal variations driven by changes only in the hot inner flow. However, as the disc parameters could not be constrained in some cases, we reiterate that although the presence of disc is indisputable, the parameters obtained from the thermal disc component could be unreliable and further inferences based on these values is unwarranted.

FRS studies of the source can help in determining the cause for variability observed in the PDS. The PDS is characterized by a BLN and a QPO (see Figure 5.3) in most of the cases. The QPO rms spectrum is found to be slightly harder than the time averaged spectra and does not require the addition of a thermal disc component (see Table 5.1 and Figure 5.4). The Comptonisation component used to model the QPO rms spectrum seems to follow the main Comptonisation. Thus, it follows that the origin of the QPO is linked to the region where Comptonisation component originates, although at different radii (Axelsson and Done, 2018). This suggests that the variabilities are localized to different radii in the inner flow, independent of the disc.

Our results suggest that the disc is present and stable throughout the outburst, with the temporal variations likely to originate in the hot inner flow. Changes in QPO frequency are generally considered to be driven by the receding accretion disc. Here we find that the evolution in the QPO is independent of the disc and is more likely to be a manifestation of the variations in the Comptonisation component or localization of the variability to different radii in the hot inner flow. As the disc does not seem to contribute to the variability, it can be assumed that the disc is either stable or absent. However, the mini-outburst reported, requires the existence of a hot disc towards the end of the main outburst (Zhang et al., 2019). Hence, it can be inferred that the disc exists, but is stable and therefore, does not contribute to the variability.

## 5.7 In a nutshell

- The Black Hole Binary source Swift J1753.5-0127 remained in outburst for $\sim 12$ years from May 2005 to April 2017. For most part of the outburst, the source remained in the Low Hard State (LHS) displaying transitions to softer states only towards the end of the outburst for short periods of time.

- We present the spectral modelling of the time-averaged spectra and FRS of the LMXB Swift J1753.5-0127 using *RXTE* data. Using FRS studies, we localize the origin of the QPO to the inner hot flow rather than the disc.

- The disc does not seem to contribute to the variability seen in the source suggesting that it is either absent or stable. The soft excess seen in the time-averaged spectra and the detection of a mini-outburst suggests the existence of a stable disc at the end of the outburst, which agrees with the above analysis.

- Application of FRS technique to similar sources would help to provide a better picture of the accretion disc geometry of BHBs.

# Chapter 6

# Summary and Future Work

The study of BHBs, as a field, is vast yet generally unexplored. This field lures thousands of researchers across the globe every year to itself, more than a century after the the idea of 'black holes' was developed by Schwarzschild in 1916. Multiple attempts have been made to understand these enigmatic systems, each one taking us a little forward in our quest for knowledge. In this thesis, we attempt to take one microscopic step forward in the same direction. We study three different BHBs, those which are known to stray off the well-understood path in the HID. We perform spectral and temporal analysis of each of these sources and comment on their accretion geometry.

An in-depth spectral and timing analysis of the Black Hole binary 4U 1630-472 during 2016 and 2018 outbursts is performed using *AstroSat* and *MAXI*. The source follows a 'c'-shaped profile in the HID, in agreement with earlier findings. Based on the HIDs of previous outbursts, we track the evolution of the source during a 'super'-outburst and 'mini'-outbursts. We model the broadband energy spectra (0.7 – 20.0 keV) of *AstroSat* observations of both outbursts using phenomenological and physical models. No Keplerian disc signature is observed at the beginning of 2016 outburst. However, the disc appears within a few hours, after which it remains prominent with temperature ($T_{in}$) $\sim$ 1.3 keV and increase in photon index ($\Gamma$) from 1.8 to 2.0, whereas the source was at a disc dominant state throughout the *AstroSat* campaign of 2018 outburst. Based on the HIDs and spectral properties, we classify the outbursts into three different states - the 'canonical' hard and soft states along with an intermediate state. Evolution of rms along different states is seen although no QPOs are detected. Mass of the black hole is estimated using inner disc radius, bolometric luminosity and two component flow model to be $3 – 9$ $M_\odot$. The transition from hard to soft state is seen for the first time in the 2016 'mini'-outburst using *AstroSat*. The disc remains dominant for most of the duration of both outbursts.

We next study the spectral and temporal properties of MAXI J0637-430 during

its 2019-2020 outburst using *NICER*, *AstroSat* and *Swift-XRT* data. The source was in a disc dominant state within a day of its detection and also traces out a 'c' shaped profile in the HID, similar to the 'mini'-outbursts of 4U 1630-472. Energy spectrum is obtained in the $0.5 - 10$ keV band with *NICER* and *Swift-XRT*, and $0.5–25$ keV with *AstroSat*. The spectra are modelled using a multicolour disc emission (*diskbb*) convolved with a thermal Comptonisation component (*thcomp*). The disc temperature decreases from 0.6 keV to 0.1 keV during the decay with a corresponding decrease in photon index ($\Gamma$) from 4.6 to 1.8. The fraction of Compton scattered photons ($f_{cov}$) remains $< 0.3$ during the decay upto mid-January 2020 and gradually increases to 1 as the source reaches hard state. PDS generated in the 0.01-100 Hz range display no QPOs although BLN is seen towards the end of January 2020. During *AstroSat* observations, $\Gamma$ lies in the range $2.3 - 2.6$ and rms increases from 11 to 20%, suggesting that the source was in an intermediate state till 21 November 2019. Spectral fitting with the relativistic disc model (*kerrbb*), in conjunction with the soft-hard transition luminosity, favour a black hole with mass $3 - 19$ M$_\odot$ with retrograde spin at a distance $< 15$ kpc. In this case also, the disc remains dominant through most of the outburst, moving to a relatively harder state only towards the end of the outburst.

Moving on from the relatively short-period outbursts of the above two sources, we proceed to Swift J1753.5-0127, which remained in outburst for $\sim 12$ years from May 2005 to April 2017. For most part of the outburst, the source remained in the LHS, displaying transitions to softer states only towards the end of the outburst for short periods of time. QPOs were observed in the PDS only during the decay. A soft thermal component was required to model the spectrum in LHS, which does not conform to the generally accepted disc truncation theory. In this work, we adopt a different approach and attempt to obtain a clearer picture of the accretion disc geometry by studying the QPO variability using frequency resolved spectroscopy. We obtain the QPO rms spectrum of the source during the bright-hard state and model it with physical components. We find that the QPO rms spectrum can be described only by a Comptonisation component with no contribution from the thermal disc. This indicates that the variability observed in the PDS originates in the Comptonisation component and the evolution of the QPOs is likely to be a result of localization of the variabilities to different radii of the hot inner flow rather than disc truncation. The minimal variation in disc parameters also points to the existence of a stable disc throughout the outburst.

The common thread that binds these three sources, apart from the obvious difference in tracks traced out in the HID, may not be clear from the outset. So, we present a systematic review of the results. The first two sources remain predominantly in the soft state. However, quick transition from hard to soft state is reported in one case, i.e., beginning of 2016 outburst of 4U 1630-472. Although difficult to confirm due to limitations of the instruments and a very

narrow time frame in which to observe the said transitions, it is only logical to assume that such transitions are the norm, rather than the exception. When we consider the generally accepted picture, the existence of an initial hard state is not just plausible, but essential as well. This seems to be the case for MAXI J0637-430 too. If one were to take the evolution of disc (from quiescence to peak) as a fact, it implies that this evolution occurred quickly (within a few hours), and does not conform to the standard disc picture. However, when we study the relation between the luminosity and disc temperature in the soft state, the relation $L \propto T^4$ holds, for both sources. This leads to the conclusion that a *standard* disc was formed, sufficiently close to the black hole, within a few hours! When we move to the decay phase (peak to quiescence), it is clear that the source remains in disc dominant state till it reaches a flux level very close to the quiescent state. The source, by this stage, is very faint, where it is classified to be in the LHS state. This raises a genuine question of whether the disc close to the BH is actually evaporated or not. It has to be kept in mind that a $10 - 15$ % contribution of the disc may be present in the LHS, which could be affected by the continuum modelling (Done et al., 2007). The existence of discs in the LHS has been already proposed multiple times as mentioned in earlier chapters. Such a residual disc, close to the BH, may facilitate the fast recurrence period of outbursts seen in 4U 1630-472 (Capitanio et al., 2015). MAXI J0637-430 is a relatively new source which went into outburst only once. If further outbursts of this source are observed and studied, one could see if the evidence for a residual disc exists in this case too.

The third source, Swift J1753.5-0127, remains in the hard state, throughout its long, 12-yr outburst. Yet, we find the evidence of a disc using spectral analysis. To confirm if this disc contributes to the variability of the source, we perform FRS studies. The conclusion that we arrive at from these studies, is that the disc, although present, is stable and it is the variability of the coronal component that affects the changes in the PDS. Hence, the presence of a stable, residual disc, can be inferred from the results of the analysis performed here. However, the mechanism that governs the duration of the outbursts and the recurrence period, is still a complete mystery.

The three sources considered here are in no way unique and do not form the part of an exhaustive list on which the existence of a stable disc can be tested out. Multiple sources exist, which have been classified as Soft or Hard X-ray transients, based on the contribution of the Comptonisation component. In fact, such a test can also be performed on the sources which undergo the so-called canonical transitions while they are in the LHS ( to check for the presence of a disc through indirect methods ), provided, clear variability signatures are observed using instruments with good spectral and temporal resolution. However, one should also ensure that the transition from the LHS to HSS ( if it exists ) is fast

enough to postulate the existence of a disc before the beginning of an outburst. Liu et al. (2011) also suggest the co-existence of a weak disc with a coronally dominated spectrum, irrespective of the coronal radiation effects, at particular accretion rates. Another aspect that can be studied is the contribution of the disc and corona to the individual variability components like the BLN and QPOs. Using these studies, we can comment on the structure and composition of the corona and obtain further evidence, in favour of or against, the stability of the disc.

*AstroSat* provides a large reservoir of data, with which to proceed further in this direction. Specifically, the extensive observations of GRS 1915+105 with *AstroSat*, from the time of its launch, greatly aid in this endeavour. Similar studies performed on this source will help in understanding the mechanisms behind the dynamic nature of this source. These studies will be extended to other apparent SXTs and BHBs which are in the LHS. However, it is difficult to obtain good quality data in the faint LHS. Therefore, long, uninterrupted observations of sources in LHS (as allowed by instrumental limitations and other factors), can be proposed with *AstroSat*. We also hope to plan future observations with upcoming missions like *X-ray Imaging Spectroscopy Mission (XRISM)* and *X-ray Polarimeter Satellite (XPoSat)*, which will focus on spectroscopic and polarimetry studies of around 50 X-ray sources. These are expected to be launched in 2023. Further studies in this direction will definitely aid in understanding these enigmatic sources.

# Chapter 7

# Recommendations

- Further information can be obtained on accretion geometry of BHBs where lack of state transitions is observed. This can be built upon to predict the time and duration of subsequent outbursts.

- The study on the contribution of individual components to the observed variabilities in the PDS can help in identifying the underlying physical mechanism behind them.

- Usage of different physical models, including two component flow, will aid in arriving at better mass estimate of the black hole.

- High spectral and timing resolution instruments like *AstroSat*, *XRISM* and *XPoSat* can be used to study more BHBs to confirm the existence of a stable disc and the properties of the corona.

# Chapter A

# List of Publications

## A.1 Refereed Journals

- "Swift J1753.5-0127 : Understanding the accretion geometry through frequency resolved spectroscopy"
  **B. E. Baby** & Ramadevi M. C.
  JoAA, 43, 18, 2022.

- "Revealing the nature of transient source MAXI J0637-430 through spectro-temporal analysis"
  **B. E. Baby**, Bhuvana G. R., Radhika D., Tilak Katoch, Samir Mandal, Anuj Nandi.
  MNRAS, 508, 2447, 2021.

- "*AstroSat* and *MAXI* view of the Black Hole Binary 4U 1630-472 during 2016 and 2018 outbursts"
  **B. E. Baby**, V. K. Agrawal, Ramadevi M. C., Tilak Katoch, H. M. Antia, Samir Mandal, Anuj Nandi.
  MNRAS, 497, 1197, 2020.

- "*AstroSat* view of GRS 1915+105 and IGR J17091-3624 : decoding the 'pulse' in the 'Heartbeat' State"
  Tilak Katoch, **B. E. Baby**, Anuj Nandi, V. K. Agrawal, H. M. Antia, Kallol Mukherjee.
  MNRAS, 501, 6123, 2021.

- "Calibration of *Scanning Sky Monitor* Onboard *AstroSat*"
  Sarwade A., Ramadevi M. C., Ravishankar B. T., Brajpal Singh, **B. E. Baby**, D. Bhattacharya, S. Seetha.
  JoAA, 42, 70, 2021.

- "Study of X-ray Transients with *Scanning Sky Monitor (SSM)* onboard *AstroSat*"
  M.C. Ramadevi, B. T. Ravishankar, Abhilash R. Sarwade, S. Vaishali, Nirmal Kumar Iyer ,Anuj Nandi, Girish V., Vivek Kumar Agarwal, **Blessy Elizabeth Baby**, Mohammed Hasan, S. Seetha, Dipankar Bhattacharya. JoAA, 123, 2016.

- "Capturing transitions between different classes in GRS 1915+105 with *AstroSat*"
  **B. E. Baby** et al., *in preparation.*

## A.2   Conferences and ATels

- Presented a talk on 'Study of Faint Sources using *AstroSat*' in AstroSat Meet held at ISRO HQ, Bangalore on 26-27 September 2017.

- Presented my work on '*AstroSat* view of the 2018 outburst of 4U 1630-472' at ASI - 2019 organized at Christ University, Bangalore from 18-22 February, 2019.

- Participated in the 'Transient Astronomy Meet' held at URSC, Bangalore on November 11-12, 2019.

- Presented a talk on my work at International Conference held in online mode from Jan 19-21, 2021, to commemorate the completion of 5 years of AstroSat in Orbit.

- *ATel #10452 (2017), SSM on AstroSat detects neutron star X-ray transient Aql X-1 in its outburst*
  M.C. Ramadevi, Ravishankar, B.T., Abhilash R. Sarwade, Vaishali, S., **B. E. Baby**, Mohammed Hasan, Vivek Kumar Agarwal, Dipankar Bhattacharya, Seetha S. & Anil Agarwal.

# References

Abe, Y., Fukazawa, Y., Kubota, A., Kasama, D., and Makishima, K. (2005). Three Spectral States of the Disk X-Ray Emission of the Black-Hole Candidate 4U 1630- 47. *PASJ*, 57:629–641.

Abramowicz, M. A., Czerny, B., Lasota, J. P., and Szuszkiewicz, E. (1988). Slim Accretion Disks. *ApJ*, 332:646.

Abramowicz, M. A. and Kluźniak, W. (2001). A precise determination of black hole spin in GRO J1655-40. *A&A*, 374:L19–L20.

Adibekyan, V., de Laverny, P., Recio-Blanco, A., Sousa, S. G., Delgado-Mena, E., Kordopatis, G., Ferreira, A. C. S., Santos, N. C., Hakobyan, A. A., and Tsantaki, M. (2018). The ambre project: searching for the closest solar siblings. *A&A*, 619:A130.

Agrawal, P. C. (2006). Broad X-ray Spectral Band Studies with Astrosat. In Wilson, A., editor, *The X-ray Universe 2005*, volume 604 of *ESA Special Publication*, page 907.

Agrawal, V. K., Nandi, A., Girish, V., and Ramadevi, M. C. (2018). Spectral and timing properties of atoll source 4U 1705-44: LAXPC/AstroSat results. *MNRAS*, 477(4):5437–5446.

Alabarta, K., Altamirano, D., Méndez, M., Cúneo, V. A., Zhang, L., Remillard, R., Castro, A., Ludlam, R. M., Steiner, J. F., Enoto, T., Homan, J., Arzoumanian, Z., Bult, P., Gendreau, K. C., Markwardt, C., Strohmayer, T. E., Uttley, P., Tombesi, F., and Buisson, D. J. K. (2020). X-ray spectral and timing evolution of MAXI J1727-203 with NICER. *MNRAS*, 497(3):3896–3910.

Altamirano, D., Belloni, T., Linares, M., van der Klis, M., Wijnands, R., Curran, P. A., Kalamkar, M., Stiele, H., Motta, S., Muñoz-Darias, T., Casella, P., and Krimm, H. (2011). The Faint "Heartbeats" of IGR J17091-3624: An Exceptional Black Hole Candidate. *ApJL*, 742(2):L17.

Antia, H. M., Agrawal, P. C., Dedhia, D., Katoch, T., Manchanda, R. K., Misra, R., Mukerjee, K., Pahari, M., Roy, J., Shah, P., and Yadav, J. S. (2021). Large Area X-ray Proportional Counter (LAXPC) in orbit performance: Calibration, background, analysis software. *Journal of Astrophysics and Astronomy*, 42(2):32.

Antia, H. M., Yadav, J. S., Agrawal, P. C., Verdhan Chauhan, J., Manchanda, R. K., Chitnis, V., Paul, B., Dedhia, D., Shah, P., Gujar, V. M., Katoch, T., Kurhade, V. N., Madhwani, P., Manojkumar, T. K., Nikam, V. A., Pand ya, A. S., Parmar, J. V., Pawar, D. M., Pahari, M., Misra, R., Navalgund, K. H., Pandiyan, R., Sharma, K. S., and Subbarao, K. (2017). Calibration of the Large Area X-Ray Proportional Counter (LAXPC) Instrument on board AstroSat. *ApJS*, 231(1):10.

Arnaud, K. A. (1996). XSPEC: The First Ten Years. In Jacoby, G. H. and Barnes, J., editors, *Astronomical Data Analysis Software and Systems V*, volume 101 of *Astronomical Society of the Pacific Conference Series*, page 17.

Athulya, M. P., Radhika, D., Agrawal, V. K., Ravishankar, B. T., Naik, S., Mandal, S., and Nandi, A. (2022). Unravelling the foretime of GRS 1915+105 using AstroSat observations: Wide-band spectral and temporal characteristics. *MNRAS*, 510(2):3019–3038.

Augusteijn, T., Kuulkers, E., and van Kerkwijk, M. H. (2001). The IR counterpart of the black-hole candidate 4U 1630-47. *A & A*, 375:447–454.

Axelsson, M. and Done, C. (2016). Revealing the nature of the QPO and its harmonic in GX 339-4 using frequency-resolved spectroscopy. *MNRAS*, 458(2):1778–1784.

Axelsson, M. and Done, C. (2018). Breaking the spectral degeneracies in black hole binaries with fast timing data: the hard state of Cygnus X-1. *MNRAS*, 480(1):751–758.

Axelsson, M., Done, C., and Hjalmarsdotter, L. (2014). An imperfect double: probing the physical origin of the low-frequency quasi-periodic oscillation and its harmonic in black hole binaries. *MNRAS*, 438(1):657–662.

Baby, B. E., Agrawal, V. K., Ramadevi, M. C., Katoch, T., Antia, H. M., Mandal, S., and Nand i, A. (2020). AstroSat and MAXI view of the black hole binary 4U 1630-472 during 2016 and 2018 outbursts. *MNRAS*, 497(1):1197–1211.

Baby, B. E., Bhuvana, G. R., Radhika, D., Katoch, T., Mandal, S., and Nandi, A. (2021). Revealing the nature of the transient source MAXI J0637-430 through spectro-temporal analysis. *MNRAS*, 508(2):2447–2457.

Baby, B. E. and Ramadevi, M. C. (2022). Swift J1753.5-0127: understanding the accretion geometry through frequency-resolved spectroscopy. *JoAA*, 43(1):18.

Bakala, P., Török, G., Karas, V., Dovčiak, M., Wildner, M., Wzientek, D., Šrámková, E., Abramowicz, M., Goluchová, K., Mazur, G. P., and Vincent, F. H. (2014). Power density spectra of modes of orbital motion in strongly curved space-time: obtaining the observable signal. *MNRAS*, 439(2):1933–1939.

Balbus, S. A. (2005). Numerical Simulations of the MRI and Real Disks. In Hameury, J. M. and Lasota, J. P., editors, *The Astrophysics of Cataclysmic Variables and Related Objects*, volume 330 of *Astronomical Society of the Pacific Conference Series*, page 185.

Barthelmy, S. D., Barbier, L. M., Cummings, J. R., Fenimore, E. E., Gehrels, N., Hullinger, D., Krimm, H. A., Markwardt, C. B., Palmer, D. M., Parsons, A., Sato, G., Suzuki, M., Takahashi, T., Tashiro, M., and Tueller, J. (2005). The Burst Alert Telescope (BAT) on the SWIFT Midex Mission. *SSR*, 120(3-4):143–164.

Begelman, M. C. (1978). Black holes in radiation-dominated gas: an analogue of the Bondi accretion problem. *MNRAS*, 184:53–67.

Belloni, T. and Hasinger, G. (1990). Variability in the noise properties of Cygnus X-1. *A&A*, 227:L33–L36.

Belloni, T., Homan, J., Casella, P., van der Klis, M., Nespoli, E., Lewin, W. H. G., Miller, J. M., and Méndez, M. (2005). The evolution of the timing properties of the black-hole transient GX 339-4 during its 2002/2003 outburst. *A & A*, 440(1):207–222.

Belloni, T., Klein-Wolt, M., Méndez, M., van der Klis, M., and van Paradijs, J. (2000). A model-independent analysis of the variability of GRS 1915+105. *A&A*, 355:271–290.

Belloni, T., Parolin, I., Del Santo, M., Homan, J., Casella, P., Fender, R. P., Lewin, W. H. G., Méndez, M., Miller, J. M., and van der Klis, M. (2006). INTEGRAL/RXTE high-energy observation of a state transition of GX 339-4. *MNRAS*, 367(3):1113–1120.

Belloni, T. M. (2010). *States and Transitions in Black Hole Binaries*, volume 794, page 53.

Belloni, T. M., Sanna, A., and Méndez, M. (2012). High-frequency quasi-periodic oscillations in black hole binaries. *MNRAS*, 426(3):1701–1709.

Belloni, T. M. and Stella, L. (2014). Fast Variability from Black-Hole Binaries. *SSR*, 183(1-4):43–60.

Bernardini, F., Zhang, G., Russell, D. M., Gelfand, J. D., Qasim, A. A., AlMannaei, A., Lewis, F., Shaw, A. W., Tomsick, J. A., and Plotkin, R. M. (2017). The optical flux of Swift J1753.5-0127 strikes back. *The Astronomer's Telegram*, 10325:1.

Bondi, H. and Hoyle, F. (1944). On the mechanism of accretion by stars. *MNRAS*, 104:273.

Bowyer, S., Byram, E. T., Chubb, T. A., and Friedman, H. (1965). Cosmic X-ray Sources. *Science*, 147(3656):394–398.

Bradt, H. V., Rothschild, R. E., and Swank, J. H. (1993). X-ray timing explorer mission. *A&AS*, 97(1):355–360.

Bradt, H. V. D. and McClintock, J. E. (1983). The optical Counterparts of Compact discrete galactic X-Ray sources. *ARA&A*, 21:13–66.

Bright, J., Staley, T., Fender, R., Motta, S., and Cantwell, T. (2017). Radio detections of the brightening black hole candidate Swift J1753.5-0127 made with the Arcminute Microkelvin Imager Large Array. *The Astronomer's Telegram*, 10110:1.

Brocksopp, C., Bandyopadhyay, R. M., and Fender, R. P. (2004). "Soft X-ray transient" outbursts which are not soft. *NewA*, 9(4):249–264.

Burrows, D. N., Hill, J. E., Nousek, J. A., Kennea, J. A., Wells, A., Osborne, J. P., Abbey, A. F., Beardmore, A., Mukerjee, K., Short, A. D. T., Chincarini, G., Campana, S., Citterio, O., Moretti, A., Pagani, C., Tagliaferri, G., Giommi, P., Capalbi, M., Tamburelli, F., Angelini, L., Cusumano, G., Bräuninger, H. W., Burkert, W., and Hartner, G. D. (2005). The Swift X-Ray Telescope. *SSR*, 120(3-4):165–195.

Cadolle Bel, M., Ribó, M., Rodriguez, J., Chaty, S., Corbel, S., Goldwurm, A., Frontera, F., Farinelli, R., D'Avanzo, P., Tarana, A., Ubertini, P., Laurent, P., Goldoni, P., and Mirabel, I. F. (2007). Simultaneous Multiwavelength Observations of the Low/Hard State of the X-Ray Transient Source SWIFT J1753.5-0127. *ApJ*, 659(1):549–560.

Cannizzo, J. K. (1993). The Accretion Disk Limit Cycle Model: Toward an Understanding of the Long-Term Behavior of SS Cygni. *ApJ*, 419:318.

Capitanio, F., Campana, R., De Cesare, G., and Ferrigno, C. (2015). Missing hard states and regular outbursts: the puzzling case of the black hole candidate 4U 1630-472. *MNRAS*, 450(4):3840–3854.

Casella, P., Belloni, T., Homan, J., and Stella, L. (2004). A study of the low-frequency quasi-periodic oscillations in the X-ray light curves of the black hole candidate <ASTROBJ>XTE J1859+226</ASTROBJ>. *A&A*, 426:587–600.

Casella, P., Belloni, T., and Stella, L. (2005). The ABC of Low-Frequency Quasi-periodic Oscillations in Black Hole Candidates: Analogies with Z Sources. *ApJ*, 629(1):403–407.

Castro-Tirado, A. J., Geballe, T. R., and Lund, N. (1996). Infrared Spectroscopy of the Superluminal Galactic Source GRS 1915+105 During the September 1994 Outburst. *ApJL*, 461:L99.

Chakrabarti, S. and Titarchuk, L. G. (1995a). Spectral Properties of Accretion Disks around Galactic and Extragalactic Black Holes. *ApJ*, 455:623.

Chakrabarti, S. and Titarchuk, L. G. (1995b). Spectral Properties of Accretion Disks around Galactic and Extragalactic Black Holes. *ApJ*, 455:623.

Chakrabarti, S. K. and Mandal, S. (2006). The Spectral Properties of Shocked Two-Component Accretion Flows in the Presence of Synchrotron Emission. *ApJL*, 642(1):L49–L52.

Chodil, G., Mark, H., Rodrigues, R., Seward, F. D., Swift, C. D., Turiel, I., Hiltner, W. A., Wallerstein, G., and Mannery, E. J. (1968). Simultaneous Observations of the Optical and X-Ray Spectra of SCO XR-1. *ApJ*, 154:645.

Conti, P. S. (1978). Stellar parameters of five early type companions of X-ray sources. *A&A*, 63:225–235.

Cunningham, C. T. (1975). The effects of redshifts and focusing on the spectrum of an accretion disk around a Kerr black hole. *ApJ*, 202:788–802.

Das, S., Chattopadhyay, I., and Chakrabarti, S. i. K. (2001). Standing Shocks around Black Holes: An Analytical Study. *ApJ*, 557(2):983–989.

Dauser, T., Garcia, J., Parker, M. L., Fabian, A. C., and Wilms, J. (2014). The role of the reflection fraction in constraining black hole spin. *MNRAS*, 444:L100–L104.

Davis, S. W., Done, C., and Blaes, O. M. (2006). Testing Accretion Disk Theory in Black Hole X-Ray Binaries. *ApJ*, 647(1):525–538.

Dieters, S. W., Belloni, T., Kuulkers, E., Woods, P., Cui, W., Zhang, S. N., Chen, W., van der Klis, M., van Paradijs, J., Swank, J., Lewin, W. H. G., and Kouveliotou, C. (2000). The Timing Evolution of 4U 1630-47 during Its 1998 Outburst. *ApJ*, 538(1):307–314.

Dihingia, I. K., Das, S., Prabhakar, G., and Mandal, S. (2020). Properties of two-temperature magnetized advective accretion flow around rotating black hole. *MNRAS*, doi : 10.1093/mnras/staa1687. staa1687.

Done, C., Gierliński, M., and Kubota, A. (2007). Modelling the behaviour of accretion flows in X-ray binaries. Everything you always wanted to know about accretion but were afraid to ask. *A & A*, 15(1):1–66.

Dunn, R. J. H., Fender, R. P., Körding, E. G., Belloni, T., and Cabanac, C. (2010). A global spectral study of black hole X-ray binaries. *MNRAS*, 403:61–82.

Dunn, R. J. H., Fender, R. P., Körding, E. G., Belloni, T., and Merloni, A. (2011). A global study of the behaviour of black hole X-ray binary discs. *MNRAS*, 411(1):337–348.

Esin, A. A., McClintock, J. E., Drake, J. J., Garcia, M. R., Haswell, C. A., Hynes, R. I., and Muno, M. P. (2001). Modeling the Low-State Spectrum of the X-Ray Nova XTE J1118+480. *ApJ*, 555(1):483–488.

Esin, A. A., McClintock, J. E., and Narayan, R. (1997). Advection-Dominated Accretion and the Spectral States of Black Hole X-Ray Binaries: Application to Nova Muscae 1991. *ApJ*, 489(2):865–889.

Evans, P. A., Beardmore, A. P., Page, K. L., Osborne, J. P., O'Brien, P. T., Willingale, R., Starling, R. L. C., Burrows, D. N., Godet, O., Vetere, L., Racusin, J., Goad, M. R., Wiersema, K., Angelini, L., Capalbi, M., Chincarini, G., Gehrels, N., Kennea, J. A., Margutti, R., Morris, D. C., Mountford, C. J., Pagani, C., Perri, M., Romano, P., and Tanvir, N. (2009). Methods and results of an automatic analysis of a complete sample of Swift-XRT observations of GRBs. *MNRAS*, 397(3):1177–1201.

Evans, W. D., Belian, R. D., and Conner, J. P. (1970). Observations of the Development and Disappearance of the X-Ray Source Centaurus XR-4. *ApJL*, 159:L57.

Fabian, A. C., Buisson, D. J., Kosec, P., Reynolds, C. S., Wilkins, D. R., Tomsick, J. A., Walton, D. J., Gandhi, P., Altamirano, D., Arzoumanian, Z., Cackett, E. M., Dyda, S., Garcia, J. A., Gendreau, K. C., Grefenstette, B. W., Homan, J., Kara, E., Ludlam, R. M., Miller, J. M., and Steiner, J. F. (2020). The soft state of the black hole transient source MAXI J1820+070: emission from the edge of the plunge region? *MNRAS*, 493(4):5389–5396.

Fender, R. P., Belloni, T. M., and Gallo, E. (2004). Towards a unified model for black hole X-ray binary jets. *MNRAS*, 355(4):1105–1118.

Fender, R. P., Homan, J., and Belloni, T. M. (2009). Jets from black hole X-ray binaries: testing, refining and extending empirical models for the coupling to X-rays. *MNRAS*, 396(3):1370–1382.

Forman, W., Jones, C., and Tananbaum, H. (1976). Uhuru observations of the galactic plane in 1970, 1971, and 1972. *ApJL*, 206:L29–L35.

Froning, C. S., Maccarone, T. J., France, K., Winter, L., Robinson, E. L., Hynes, R. I., and Lewis, F. (2014). Multiwavelength Observations of Swift J1753.5-0127. *ApJ*, 780(1):48.

García, J., Dauser, T., Lohfink, A., Kallman, T. R., Steiner, J. F., McClintock, J. E., Brenneman, L., Wilms, J., Eikmann, W., Reynolds, C. S., and Tombesi, F. (2014). Improved Reflection Models of Black Hole Accretion Disks: Treating the Angular Distribution of X-Rays. *ApJ*, 782(2):76.

Gatuzz, E., Díaz Trigo, M., Miller-Jones, J. C. A., and Migliari, S. (2019). Chandra high-resolution spectra of 4U 1630-47: the disappearance of the wind. *MNRAS*, 482(2):2597–2611.

Gendreau, K. C., Arzoumanian, Z., Adkins, P. W., Albert, C. L., Anders, J. F., Aylward, A. T., Baker, C. L., Balsamo, E. R., Bamford, W. A., Benegalrao, S. S., Berry, D. L., Bhalwani, S., Black, J. K., Blaurock, C., Bronke, G. M., Brown, G. L., Budinoff, J. G., Cantwell, J. D., Cazeau, T., Chen, P. T., Clement, T. G., Colangelo, A. T., Coleman, J. S., Coopersmith, J. D., Dehaven, W. E., Doty, J. P., Egan, M. D., Enoto, T., Fan, T. W.-M., Ferro, D. M., Foster, R., Galassi, N. M., Gallo, L. D., Green, C. M., Grosh, D., Ha, K. Q., Hasouneh, M. A., Heefner, K. B., Hestnes, P., Hoge, L. J., Jacobs, T. M., Jørgensen, J. L., Kaiser, M. A., Kellogg, J. W., Kenyon, S. J., Koenecke, R. G., Kozon, R. P., LaMarr, B., Lambertson, M. D., Larson, A. M., Lentine, S., Lewis, J. H., Lilly, M. G., Liu, K. A., Malonis, A., Manthripragada, S. S., Markwardt, C. B., Matonak, B. D., Mcginnis, I. E., Miller, R. L., Mitchell, A. L., Mitchell, J. W., Mohammed, J. S., Monroe, C. A., de Garcia, K. M. M., Mulé, P. D., Nagao, L. T., Ngo, S. N., Norris, E. D., Norwood, D. A., Novotka, J., Okajima, T., Olsen, L. G., Onyeachu, C. O., Orosco, H. Y., Peterson, J. R., Pevear, K. N., Pham,

K. K., Pollard, S. E., Pope, J. S., Powers, D. F., Powers, C. E., Price, S. R., Prigozhin, G. Y., Ramirez, J. B., Reid, W. J., Remillard, R. A., Rogstad, E. M., Rosecrans, G. P., Rowe, J. N., Sager, J. A., Sanders, C. A., Savadkin, B., Saylor, M. R., Schaeffer, A. F., Schweiss, N. S., Semper, S. R., Serlemitsos, P. J., Shackelford, L. V., Soong, Y., Struebel, J., Vezie, M. L., Villasenor, J. S., Winternitz, L. B., Wofford, G. I., Wright, M. R., Yang, M. Y., and Yu, W. H. (2016). The Neutron star Interior Composition Explorer (NICER): design and development. In den Herder, J.-W. A., Takahashi, T., and Bautz, M., editors, *Space Telescopes and Instrumentation 2016: Ultraviolet to Gamma Ray*, volume 9905, pages 420 – 435. International Society for Optics and Photonics, SPIE.

Ghisellini, G., Haardt, F., and Fabian, A. C. (1993). On re-acceleration, pairs and the high-energy spectrum of AGN and galactic black hole candidates. *MNRAS*, 263:L9–L12.

Ghisellini, G., Haardt, F., and Matt, G. (2004). Aborted jets and the X-ray emission of radio-quiet AGNs. *A&A*, 413:535–545.

Giacconi, R., Gursky, H., Paolini, F. R., and Rossi, B. B. (1962). Evidence for x Rays From Sources Outside the Solar System. *PRL*, 9(11):439–443.

Gierliński, M. and Done, C. (2004). Black hole accretion discs: reality confronts theory. *MNRAS*, 347(3):885–894.

Gierliński, M., Zdziarski, A. A., Poutanen, J., Coppi, P. S., Ebisawa, K., and Johnson, W. N. (1999). Radiation mechanisms and geometry of Cygnus X-1 in the soft state. *MNRAS*, 309(2):496–512.

Hambsch, F. J., Myers, G., Monard, L. A. G., and Patterson, J. (2019). Optical Observations of MAXI J0637-430. *The Astronomer's Telegram*, 13278:1.

Hameury, J. M. (2020). A review of the disc instability model for dwarf novae, soft X-ray transients and related objects. *Advances in Space Research*, 66(5):1004–1024.

Harries, J. R., McCracken, K. G., Francey, R. J., and Fenton, A. G. (1967). A Strong X-ray Source in the Vicinity of the Constellation Crux. *Nature*, 215(5096):38–40.

Holt, S., Kaluzienski, L., Mushotzky, R., Boldt, F., and Serlemitsos, P. (1978). 4U 1630-47. *IAUCirc*, 3292:1.

Huppenkothen, D., Bachetti, M., Stevens, A. L., Migliari, S., Balm, P., Hammad, O., Khan, U. M., Mishra, H., Rashid, H., Sharma, S., Martinez Ribeiro, E., and Valles Blanco, R. (2019). Stingray: A Modern Python Library for Spectral Timing. *ApJ*, 881(1):39.

Ichimaru, S. (1977). Bimodal behavior of accretion disks: theory and application to Cygnus X-1 transitions. *ApJ*, 214:840–855.

Ingram, A., Done, C., and Fragile, P. C. (2009). Low-frequency quasi-periodic oscillations spectra and Lense-Thirring precession. *MNRAS*, 397(1):L101–L105.

Iyer, N., Nandi, A., and Mandal, S. (2015). Determination of the Mass of IGR J17091-3624 from "Spectro-temporal" Variations during the Onset Phase of the 2011 Outburst. *ApJ*, 807(1):108.

James, F. and Winkler, M. (2004). *MINUIT User's Guide*, http://seal.web.cern.ch/seal/documents/minuit/mnusers-guide.pdf.

Jana, A., Jaisawal, G. K., Naik, S., Kumari, N., Chhotaray, B., Altamirano, D., Remillard, R. A., and Gendreau, K. C. (2021). NICER observations of the black hole candidate MAXI J0637-430 during the 2019-2020 outburst. *MNRAS*, 504(4):4793–4805.

Janiuk, A. and Czerny, B. (2011). On different types of instabilities in black hole accretion discs: implications for X-ray binaries and active galactic nuclei. *MNRAS*, 414(3):2186–2194.

Jones, C., Forman, W., Tananbaum, H., and Turner, M. J. L. (1976). Uhuru and Ariel V observations of 3U 1630-47: a recurrent transient X-ray source. *ApJ*, 210:L9–L11.

Jonker, P. G., Kaur, K., Stone, N., and Torres, M. A. P. (2021). The observed mass distribution of Galactic black hole LMXBs is biased against massive black holes. *arXiv e-prints*, page arXiv:2104.03596.

Kajava, J. J. E., Veledina, A., Tsygankov, S., and Neustroev, V. (2016). The origin of seed photons for Comptonization in the black hole binary Swift J1753.5-0127. *A & A*, 591:A66.

Kalemci, E., Maccarone, T. J., and Tomsick, J. A. (2018). A Dust-scattering Halo of 4U 1630-47 Observed with Chandra and Swift: New Constraints on the Source Distance. *ApJ*, 859(2):88.

Kaluzienski, L. J. and Holt, S. S. (1977). X-Ray Flare. *IAUCirc.*, 3144:1.

Kara, E., Steiner, J. F., Fabian, A. C., Cackett, E. M., Uttley, P., Remillard, R. A., Gendreau, K. C., Arzoumanian, Z., Altamirano, D., Eikenberry, S., Enoto, T., Homan, J., Neilsen, J., and Stevens, A. L. (2019). The corona contracts in a black-hole transient. *Nature*, 565(7738):198–201.

Katoch, T., Baby, B. E., Nandi, A., Agrawal, V. K., Antia, H. M., and Mukerjee, K. (2021). AstroSat view of IGR J17091-3624 and GRS 1915 + 105: decoding the 'pulse' in the 'Heartbeat State'. *MNRAS*, 501(4):6123–6138.

Kennea, J. A., Bahramian, A., Evans, P. A., Beardmore, A. P., Krimm, H. A., Romano, P., Yamaoka, K., Serino, M., and Negoro, H. (2019). MAXI J0637-430: Swift localization, optical counterpart. *The Astronomer's Telegram*, 13257:1.

King, A. L., Miller, J. M., and Raymond, J. (2012). Warm Absorbers and Outflows in the Seyfert-1 Galaxy NGC 4051. *ApJ*, 746(1):2.

King, A. L., Walton, D. J., Miller, J. M., Barret, D., Boggs, S. E., Christensen, F. E., Craig, W. W., Fabian, A. C., Fürst, F., Hailey, C. J., Harrison, F. A., Krivonos, R., Mori, K., Natalucci, L., Stern, D., Tomsick, J. A., and Zhang, W. W. (2014). The Disk Wind in the Rapidly Spinning Stellar-mass Black Hole 4U 1630-472 Observed with NuSTAR. *ApJ*, 784(1):L2.

King, A. R. and Ritter, H. (1999). Cygnus X-2, super-Eddington mass transfer, and pulsar binaries. *MNRAS*, 309(1):253–260.

Klein-Wolt, M., Fender, R. P., Pooley, G. G., Belloni, T., Migliari, S., Morgan, E. H., and van der Klis, M. (2002). Hard X-ray states and radio emission in GRS 1915+105. *MNRAS*, 331(3):745–764.

Knoll, G. F. (1989). *Radiative Detection and Measurement.*

Kolb, U., Davies, M. B., King, A., and Ritter, H. (2000). The violent past of Cygnus X-2. *MNRAS*, 317(2):438–446.

Kompaneets, A. S. (1957). The Establishment of Thermal Equilibrium between Quanta and Electrons. *Soviet Journal of Experimental and Theoretical Physics*, 4(5):730–737.

Kravtsov, V., Berdyugin, A., Veledina, A., Poutanen, J., Piirola, V., Berdyugina, S., Sakanoi, T., and Kagitani, M. (2019). Optical polarimetry of the soft-state low-mass X-ray binary MAXI J0637-430. *The Astronomer's Telegram*, 13291:1.

Kubota, A. and Makishima, K. (2004). The Three Spectral Regimes Found in the Stellar Black Hole XTE J1550-564 in Its High/Soft State. *ApJ*, 601(1):428–438.

Kubota, A., Makishima, K., and Ebisawa, K. (2001). Observational Evidence for Strong Disk Comptonization in GRO J1655-40. *ApJ*, 560(2):L147–L150.

Kubota, A., Tanaka, Y., Makishima, K., Ueda, Y., Dotani, T., Inoue, H., and Yamaoka, K. (1998). Evidence for a Black Hole in the X-Ray Transient GRS 1009-45. *PASJ*, 50:667–673.

Kuulkers, E., Parmar, A. N., Kitamoto, S., Cominsky, L. R., and Sood, R. K. (1997). Complex outburst behaviour from the black hole candidate 4U1630-47. *MNRAS*, 291(1):81–90.

Kuulkers, E., Wijnands, R., Belloni, T., Méndez, M., van der Klis, M., and van Paradijs, J. (1998). Absorption Dips in the Light Curves of GRO J1655-40 and 4U 1630-47 during Outburst. *ApJ*, 494(2):753–758.

Kylafis, N. D., Contopoulos, I., Kazanas, D., and Christodoulou, D. M. (2012). Formation and destruction of jets in X-ray binaries. *A & A*, 538:A5.

Kylafis, N. D., Reig, P., and Papadakis, I. (2020). A quantitative explanation of the type-B QPOs in GX 339-4. *A&A*, 640:L16.

Lasota, J.-P. (2001). The disc instability model of dwarf novae and low-mass X-ray binary transients. *NewAR*, 45(7):449–508.

Lazar, H., Tomsick, J. A., Pike, S. N., Bachetti, M., Buisson, D. J. K., Connors, R. M. T., Fabian, A. C., Fuerst, F., García, J. A., Hare, J., Jiang, J., Shaw, A. W., and Walton, D. J. (2021). Spectral and Timing Analysis of NuSTAR and Swift/XRT Observations of the X-Ray Transient MAXI J0637-430. *arXiv e-prints*, page arXiv:2108.03299.

Lewin, W. H. G. and Livingston, W. (1995). Book Review: X-ray binaries / Cambridge U Press, 1995 &amp; 1997. *Journal of the British Astronomical Association*, 105(6):284.

Li, K.-L. and Kong, A. K. H. (2019). Optical observations of the black hole X-ray transient candidate MAXI J0637-430. *The Astronomer's Telegram*, 13276:1.

Li, L.-X., Zimmerman, E. R., Narayan, R., and McClintock, J. E. (2005). Multitemperature Blackbody Spectrum of a Thin Accretion Disk around a Kerr Black Hole: Model Computations and Comparison with Observations. *ApJS*, 157(2):335–370.

Liu, B. F., Done, C., and Taam, R. E. (2011). The Effect of Coronal Radiation on a Residual Inner Disk in the Low/Hard Spectral State of Black Hole X-ray Binary Systems. *ApJ*, 726(1):10.

Liu, B. F. and Taam, R. E. (2009). Application of the Disk Evaporation Model to Active Galactic Nuclei. *ApJ*, 707(1):233–242.

Longair, M. S. (2011). *High Energy Astrophysics*.

Maccarone, T. J. and Coppi, P. S. (2003). Hysteresis in the light curves of soft X-ray transients. *MNRAS*, 338(1):189–196.

Makishima, K., Kubota, A., Mizuno, T., Ohnishi, T., Tashiro, M., Aruga, Y., Asai, K., Dotani, T., Mitsuda, K., Ueda, Y., Uno, S., Yamaoka, K., Ebisawa, K., Kohmura, Y., and Okada, K. (2000). The Nature of Ultraluminous Compact X-Ray Sources in Nearby Spiral Galaxies. *ApJ*, 535(2):632–643.

Makishima, K., Maejima, Y., Mitsuda, K., Bradt, H. V., Remillard, R. A., Tuohy, I. R., Hoshi, R., and Nakagawa, M. (1986). Simultaneous X-Ray and Optical Observations of GX 339-4 in an X-Ray High State. *ApJ*, 308:635.

Malzac, J. (2012). On the Nature of the X-Ray Corona of Black Hole Binaries. In *International Journal of Modern Physics Conference Series*, volume 8 of *International Journal of Modern Physics Conference Series*, pages 73–83.

Mandal, S. and Mondal, S. (2018). Spectral properties of the accretion discs around rotating black holes. *Journal of Astrophysics and Astronomy*, 39(1):19.

Mao, D., Lin, J., Yan, Z., and Yu, W. (2018). A new outburst of 4U 1630-472 and its very soft X-ray spectra. *The Astronomer's Telegram*, 11722:1.

Mark, H., Price, R., Rodrigues, R., Seward, F. D., and Swift, C. D. (1969). Detection of X-Rays from the Large Magellanic Cloud. *ApJL*, 155:L143.

Markoff, S., Falcke, H., and Fender, R. (2001). A jet model for the broadband spectrum of XTE J1118+480. Synchrotron emission from radio to X-rays in the Low/Hard spectral state. *A&A*, 372:L25–L28.

Markoff, S., Nowak, M. A., and Wilms, J. (2005). Going with the Flow: Can the Base of Jets Subsume the Role of Compact Accretion Disk Coronae? *ApJ*, 635(2):1203–1216.

Matsuoka, M., Kawasaki, K., Ueno, S., Tomida, H., Kohama, M., Suzuki, M., Adachi, Y., Ishikawa, M., Mihara, T., Sugizaki, M., Isobe, N., Nakagawa, Y., Tsunemi, H., Miyata, E., Kawai, N., Kataoka, J., Morii, M., Yoshida, A., Negoro, H., Nakajima, M., Ueda, Y., Chujo, H., Yamaoka, K., Yamazaki, O., Nakahira, S., You, T., Ishiwata, R., Miyoshi, S., Eguchi, S., Hiroi, K., Katayama, H., and Ebisawa, K. (2009). The MAXI Mission on the ISS: Science and Instruments for Monitoring All-Sky X-Ray Images. *PASJ*, 61:999.

Mayer, M. and Pringle, J. E. (2007). Time-dependent models of two-phase accretion discs around black holes. *MNRAS*, 376(1):435–456.

McConnell, M. L., Ryan, J. M., Collmar, W., Schönfelder, V., Steinle, H., Strong, A. W., Bloemen, H., Hermsen, W., Kuiper, L., Bennett, K., Phlips, B. F., and Ling, J. C. (2000). A High-Sensitivity Measurement of the MeV Gamma-Ray Spectrum of Cygnus X-1. *ApJ*, 543(2):928–937.

Merloni, A. (2003). Beyond the standard accretion disc model: coupled magnetic disc-corona solutions with a physically motivated viscosity law. *MNRAS*, 341(3):1051–1056.

Merloni, A. and Nayakshin, S. (2006). On the limit-cycle instability in magnetized accretion discs. *MNRAS*, 372(2):728–734.

Meyer, F. and Meyer-Hofmeister, E. (1984). Outbursts in dwarf novae accretion disks. *A&Ap*, 132:143–150.

Meyer, F. and Meyer-Hofmeister, E. (1994). Accretion disk evaporation by a coronal siphon flow. *A&A*, 288:175–182.

Meyer-Hofmeister, E., Liu, B. F., Qiao, E., and Taam, R. E. (2020). Wind accretion in Cygnus X-1. *A&A*, 637:A66.

Miller, J. M. (2007). Relativistic X-Ray Lines from the Inner Accretion Disks Around Black Holes. *ARA&A*, 45(1):441–479.

Miller, J. M., Tomsick, J. A., Bachetti, M., Wilkins, D., Boggs, S. E., Christensen, F. E., Craig, W. W., Fabian, A. C., Grefenstette, B. W., Hailey, C. J., Harrison, F. A., Kara, E., King, A. L., Stern, D. K., and Zhang, W. W. (2015). New Constraints on the Black Hole Low/Hard State Inner Accretion Flow with NuSTAR. *ApJL*, 799(1):L6.

Miniutti, G. and Fabian, A. C. (2004). A light bending model for the X-ray temporal and spectral properties of accreting black holes. *MNRAS*, 349(4):1435–1448.

Misra, R., Yadav, J. S., Verdhan Chauhan, J., Agrawal, P. C., Antia, H. M., Pahari, M., Chitnis, V. R., Dedhia, D., Katoch, T., Madhwani, P., Manchanda, R. K., Paul, B., and Shah, P. (2017). AstroSat/LAXPC Observation of Cygnus X-1 in the Hard State. *ApJ*, 835(2):195.

Mitsuda, K., Inoue, H., Koyama, K., Makishima, K., Matsuoka, M., Ogawara, Y., Shibazaki, N., Suzuki, K., Tanaka, Y., and Hirano, T. (1984). Energy spectra of low-mass binary X-ray sources observed from Tenma. *PASJ*, 36:741–759.

Miyamoto, S., Kitamoto, S., Iga, S., Negoro, H., and Terada, K. (1992). Canonical Time Variations of X-Rays from Black Hole Candidates in the Low-Intensity State. *ApJL*, 391:L21.

Molteni, D., Sponholz, H., and Chakrabarti, S. K. (1996). Resonance Oscillation of Radiative Shock Waves in Accretion Disks around Compact Objects. *ApJ*, 457:805.

Moret, M., Zebende, G., Júnior, E., and Pereira, M. (2003). Fluctuation analysis of stellar x-ray binary systems. *Physical review. E, Statistical, nonlinear, and soft matter physics*, 68:041104.

Morgan, E. H., Remillard, R. A., and Greiner, J. (1997). RXTE Observations of QPOs in the Black Hole Candidate GRS 1915+105. *ApJ*, 482(2):993–1010.

Motta, S., Muñoz-Darias, T., Casella, P., Belloni, T., and Homan, J. (2011). Low-frequency oscillations in black holes: a spectral-timing approach to the case of GX 339-4. *MNRAS*, 418(4):2292–2307.

Motta, S. E. (2016). Quasi periodic oscillations in black hole binaries. *Astronomische Nachrichten*, 337(4-5):398.

Motta, S. E., Casella, P., and Fender, R. P. (2018). Radio-loudness in black hole transients: evidence for an inclination effect. *MNRAS*, 478(4):5159–5173.

Mukerjee, K., Antia, H. M., and Katoch, T. (2020). AstroSat Observations of GRO J2058+42 during the 2019 Outburst. *ApJ*, 897(1):73.

Murata, K. L., Adachi, R., Kawai, N., Miyakawa, K., Morihana, K., Nagayama, T., Shiraishi, K., Oeda, M., Iida, K., Niwano, S., Ogawa, F., Toma, S., Hosokawa, R., and Yatsu, Y. (2019). Near-infrared observation of MAXI J0637-430. *The Astronomer's Telegram*, 13292:1.

Nandi, A., Debnath, D., Mandal, S., and Chakrabarti, S. K. (2012). Accretion flow dynamics during the evolution of timing and spectral properties of GX 339-4 during its 2010-11 outburst. *A & A*, 542:A56.

Nandi, A., Mandal, S., Sreehari, H., Radhika, D., Das, S., Chattopadhyay, I., Iyer, N., Agrawal, V. K., and Aktar, R. (2018). Accretion flow dynamics during 1999 outburst of XTE J1859+226—modeling of broadband spectra and constraining the source mass. *Ap & SS*, 363(5):90.

Narayan, R. and McClintock, J. E. (2008). Advection-dominated accretion and the black hole event horizon. *NewAR*, 51(10-12):733–751.

Narayan, R. and Yi, I. (1995). Advection-dominated Accretion: Underfed Black Holes and Neutron Stars. *ApJ*, 452:710.

Negoro, H., Miike, K., Nakajima, M., Maruyama, W., Aoki, M., Kobayashi, K., Mihara, T., Tamagawa, T., Matsuoka, M., Sakamoto, T., Serino, M., Sugita, S., Nishida, H., Yoshida, A., Tsuboi, Y., Iwakiri, W., Sasaki, R., Kawai, H., Sato, T., Shidatsu, M., Kawai, N., Oeda, M., Shiraishi, K., Nakahira, S., Sugawara, Y., Ueno, S., Tomida, H., Ishikawa, M., Isobe, N., Shimomukai, R., Tominaga, M., Ueda, Y., Tanimoto, A., Yamada, S., Ogawa, S., Setoguchi, K., Yoshitake, T., Tsunemi, H., Yoneyama, T., Asakura, K., Hattori, K., Yamauchi, M., Iwahori, S., Kurihara, Y., Kurogi, K., Kawamuro, T., Yamaoka, K., Kawakubo, Y., Sugizaki, M., and MAXI Team (2019). MAXI/GSC detection of a soft X-ray transient MAXI J0637-430. *The Astronomer's Telegram*, 13256:1.

Novikov, I. D. and Thorne, K. S. (1973). Astrophysics of black holes. In *Black Holes (Les Astres Occlus)*, pages 343–450.

Palmer, D. M., Barthelmey, S. D., Cummings, J. R., Gehrels, N., Krimm, H. A., Markwardt, C. B., Sakamoto, T., and Tueller, J. (2005). BAT detection of a new gamma ray source SWIFT J1753.5-0127. *The Astronomer's Telegram*, 546:1.

Parmar, A. N., Angelini, L., and White, N. E. (1995). Periodic Outbursts from the Ultrasoft X-Ray Transient 4U 1630-47. *ApJ*, 452:L129.

Parmar, A. N., Stella, L., and White, N. E. (1986). The Evolution of the 1984 Outburst of the Transient X-Ray Source 4U 1630-47. *ApJ*, 304:664.

Petterson, J. A. (1978). On the occurrence of streams and disks in massive X-ray binary systems. *ApJ*, 224:625–630.

Podsiadlowski, P. and Rappaport, S. (2000). Cygnus X-2: The Descendant of an Intermediate-Mass X-Ray Binary. *ApJ*, 529(2):946–951.

Priedhorsky, W. (1986). Recurrent Population II X-ray transients — similarities to SU UMa cataclysmic variables. *Ap & SS*, 126(1):89–98.

Radhika, D., Sreehari, H., Nandi, A., Iyer, N., and Mand al, S. (2018). Broad-band spectral evolution and temporal variability of IGR J17091-3624 during its 2016 outburst: SWIFT and NuSTAR results. *Ap & SS*, 363(9):189.

Ramadevi, M. C., Ravishankar, B. T., Sitaramamurthy, N., Meena, G., Singh, B., Jain, A., Yadav, R., Agarwal, A., Babu, V. C., Kumar, Kushwaha, A., Vaishali, S., Iyer, N. K., Nand i, A., Girish, V., Agarwal, V. K., Seetha, S., Bhattacharya, D., Balaji, K., Kumar, M., and Kulshresta, P. (2017). Early In-orbit Performance of Scanning Sky Monitor Onboard AstroSat. *Journal of Astrophysics and Astronomy*, 38(2):32.

Ramadevi, M. C. and Seetha, S. (2007). RXTE observations of the low/hard state X-ray outburst of the new X-ray transient SWIFT J1753.5-0127. *MNRAS*, 378(1):182–188.

Rees, M. J., Begelman, M. C., Blandford, R. D., and Phinney, E. S. (1982). Ion-supported tori and the origin of radio jets. *Nature*, 295(5844):17–21.

Remillard, R. A. and McClintock, J. E. (2006). X-Ray Properties of Black-Hole Binaries. *ARA&A*, 44(1):49–92.

Remillard, R. A., Muno, M. P., McClintock, J. E., and Orosz, J. A. (2002). Evidence for Harmonic Relationships in the High-Frequency Quasi-periodic Oscillations of XTE J1550-564 and GRO J1655-40. *ApJ*, 580(2):1030–1042.

Revnivtsev, M., Gilfanov, M., and Churazov, E. (1999). The frequency resolved spectroscopy of CYG X-1: fast variability of the Fe K_$\alpha$ line. *A&A*, 347:L23–L26.

Reynolds, C. S. (2014). Measuring Black Hole Spin Using X-Ray Reflection Spectroscopy. *SSR*, 183(1-4):277–294.

Rodriguez, J., Bodaghee, A., Kaaret, P., Tomsick, J. A., Kuulkers, E., Malaguti, G., Petrucci, P. O., Cabanac, C., Chernyakova, M., Corbel, S., Deluit, S., Di Cocco, G., Ebisawa, K., Goldwurm, A., Henri, G., Lebrun, F., Paizis, A., Walter, R., and Foschini, L. (2006). INTEGRAL and XMM-Newton observations of the X-ray pulsar IGR J16320-4751/AX J1631.9-4752. *MNRAS*, 366(1):274–282.

Rodriguez, J., Tomsick, J. A., Foschini, L., Walter, R., Goldwurm, A., Corbel, S., and Kaaret, P. (2003). An XMM-Newton observation of IGR J16320-4751 = AX J1631.9-4752. *A & A*, 407:L41–L45.

Russell, T. D., Miller-Jones, J. C. A., Sivakoff, G. R., and Tetarenko, A. J. (2019). ATCA radio detection of the new X-ray transient MAXI J0637-430. *The Astronomer's Telegram*, 13275:1.

Rybicki, G. B. and Lightman, A. P. (1986). *Radiative Processes in Astrophysics.*

Ryu, D., Chakrabarti, S. K., and Molteni, D. (1997). Zero-Energy Rotating Accretion Flows near a Black Hole. *ApJ*, 474(1):378–388.

Seetha, S., Ramadevi, M. C., Babu, V. C., Sharma, M. R., Murthy, N. S. R., Ashoka, B. N., Shyama, K. C., Kulkarni, R., Meena, G., and Sreekumar, P. (2006). The Scanning Sky Monitor (SSM) on ASTROSAT. *Advances in Space Research*, 38(12):2995–2998.

Seifina, E., Titarchuk, L., and Shaposhnikov, N. (2014). Black Hole Mass Determination in the X-Ray Binary 4U 1630-47: Scaling of Spectral and Variability Characteristics. *ApJ*, 789(1):57.

Shakura, N. I. and Sunyaev, R. A. (1973). Reprint of 1973A&amp;A....24..337S. Black holes in binary systems. Observational appearance. *A & A*, 500:33–51.

Shapiro, S. L., Lightman, A. P., and Eardley, D. M. (1976). A two-temperature accretion disk model for Cygnus X-1: structure and spectrum. *ApJ*, 204:187–199.

Share, G., Wood, K., Byram, E., Meekins, J., Shulman, S., Griffiths, R., Kaluzienski, L. J., Boldt, E. A., Holt, S. S., Mushotzky, R. F., Serlemitsos, P. J., and Rothschild, R. E. (1978). 4U 1630-47. *IAUCirc.*, 3197:3.

Shaw, A. W., Charles, P. A., Casares, J., and Hernández Santisteban, J. V. (2016a). No evidence for a low-mass black hole in Swift J1753.5-0127. *MNRAS*, 463(2):1314–1322.

Shaw, A. W., Gandhi, P., Altamirano, D., Uttley, P., Tomsick, J. A., Charles, P. A., Fürst, F., Rahoui, F., and Walton, D. J. (2016b). A low-luminosity soft state in the short-period black hole X-ray binary Swift J1753.5-0127. *MNRAS*, 458(2):1636–1644.

Shaw, A. W., Tetarenko, B. E., Dubus, G., Dinçer, T., Tomsick, J. A., Gandhi, P., Plotkin, R. M., and Russell, D. M. (2019). The curious case of Swift J1753.5-0127: a black hole low-mass X-ray binary analogue to Z cam type dwarf novae. *MNRAS*, 482(2):1840–1857.

Shaw, A. W., Tomsick, J. A., Bahramian, A., Gandhi, P., Russell, D. M., and Charles, P. A. (2016c). Swift J1753.5-0127 no longer detected by Swift. *The Astronomer's Telegram*, 9735:1.

Shimura, T. and Takahara, F. (1995). On the Spectral Hardening Factor of the X-Ray Emission from Accretion Disks in Black Hole Candidates. *ApJ*, 445:780.

Siemiginowska, A., Czerny, B., and Kostyunin, V. (1996). Evolution of an Accretion Disk in an Active Galactic Nucleus. *ApJ*, 458:491.

Singh, K. P., Stewart, G. C., Westergaard, N. J., Bhattacharayya, S., Chandra, S., Chitnis, V. R., Dewangan, G. C., Kothare, A. T., Mirza, I. M., Mukerjee, K., Navalkar, V., Shah, H., Abbey, A. F., Beardmore, A. P., Kotak, S., Kamble, N., Vishwakarama, S., Pathare, D. P., Risbud, V. M., Koyand e, J. P., Stevenson, T., Bicknell, C., Crawford, T., Hansford, G., Peters, G., Sykes, J., Agarwal, P., Sebastian, M., Rajarajan, A., Nagesh, G., Narendra, S., Ramesh, M., Rai, R., Navalgund, K. H., Sarma, K. S., Pandiyan, R., Subbarao, K., Gupta, T., Thakkar, N., Singh, A. K., and Bajpai, A.

(2017). Soft X-ray Focusing Telescope Aboard AstroSat: Design, Characteristics and Performance. *Journal of Astrophysics and Astronomy*, 38(2):29.

Singh, K. P., Tandon, S. N., Agrawal, P. C., Antia, H. M., Manchanda, R. K., Yadav, J. S., Seetha, S., Ramadevi, M. C., Rao, A. R., Bhattacharya, D., Paul, B., Sreekumar, P., Bhattacharyya, S., Stewart, G. C., Hutchings, J., Annapurni, S. A., Ghosh, S. K., Murthy, J., Pati, A., Rao, N. K., Stalin, C. S., Girish, V., Sankarasubramanian, K., Vadawale, S., Bhalerao, V. B., Dewangan, G. C., Dedhia, D. K., Hingar, M. K., Katoch, T. B., Kothare, A. T., Mirza, I., Mukerjee, K., Shah, H., Shah, P., Mohan, R., Sangal, A. K., Nagabhusana, S., Sriram, S., Malkar, J. P., Sreekumar, S., Abbey, A. F., Hansford, G. M., Beardmore, A. P., Sharma, M. R., Murthy, S., Kulkarni, R., Meena, G., Babu, V. C., and Postma, J. (2014). *ASTROSAT mission*, volume 9144 of *Society of Photo-Optical Instrumentation Engineers (SPIE) Conference Series*.

Sobolewska, M. A. and Życki, P. T. (2006). Spectral and Fourier analyses of X-ray quasi-periodic oscillations in accreting black holes. *MNRAS*, 370(1):405–414.

Sreehari, H., Nandi, A., Das, S., Agrawal, V. K., Mandal, S., Ramadevi, M. C., and Katoch, T. (2020). AstroSat view of GRS 1915+105 during the soft state: detection of HFQPOs and estimation of mass and spin. *MNRAS*, 499(4):5891–5901.

Sreehari, H., Nandi, A., Radhika, D., Iyer, N., and Mandal, S. (2018). Observational aspects of outbursting black hole sources: Evolution of spectro-temporal features and X-ray variability. *Journal of Astrophysics and Astronomy*, 39(1):5.

Sreehari, H., Ravishankar, B. T., Iyer, N., Agrawal, V. K., Katoch, T. B., Mandal, S., and Nand i, A. (2019). AstroSat view of MAXI J1535-571: broad-band spectro-temporal features. *MNRAS*, 487(1):928–941.

Stella, L. and Rosner, R. (1984). Magnetic field instabilities in accretion disks. *ApJ*, 277:312–321.

Stella, L. and Vietri, M. (1998). Lense-Thirring Precession and Quasi-periodic Oscillations in Low-Mass X-Ray Binaries. *ApJL*, 492(1):L59–L62.

Stella, L., Vietri, M., and Morsink, S. M. (1999). Correlations in the Quasi-periodic Oscillation Frequencies of Low-Mass X-Ray Binaries and the Relativistic Precession Model. *ApJL*, 524(1):L63–L66.

Strader, J., Aydi, E., Sokolovsky, K., and Shishkovsky, L. (2019). Optical spectroscopy of MAXI J0637-430 confirms a new low-mass X-ray binary. *The Astronomer's Telegram*, 13260:1.

Strohmayer, T. E. (2001). Discovery of a 450 HZ Quasi-periodic Oscillation from the Microquasar GRO J1655-40 with the Rossi X-Ray Timing Explorer. *ApJL*, 552(1):L49–L53.

Sunyaev, R. A. and Truemper, J. (1979). Hard X-ray spectrum of CYG X-1. *Nature*, 279:506–508.

Tanaka, Y. and Lewin, W. H. G. (1995). Black hole binaries. pages 126–174.

Tandon, S. N., Subramaniam, A., Girish, V., Postma, J., Sankarasubramanian, K., Sriram, S., Stalin, C. S., Mondal, C., Sahu, S., Joseph, P., Hutchings, J., Ghosh, S. K., Barve, I. V., George, K., Kamath, P. U., Kathiravan, S., Kumar, A., Lancelot, J. P., Leahy, D., Mahesh, P. K., Mohan, R., Nagabhushana, S., Pati, A. K., Kameswara Rao, N., Sreedhar, Y. H., and Sreekumar, P. (2017). In-orbit Calibrations of the Ultraviolet Imaging Telescope. *AJ*, 154(3):128.

Tetarenko, B. E., Shaw, A. W., Manrow, E. R., Charles, P. A., Miller, J. M., Russell, T. D., and Tetarenko, A. J. (2021). Using optical spectroscopy to map the geometry and structure of the irradiated accretion discs in low-mass X-ray binaries: the pilot study of MAXI J0637-430. *MNRAS*, 501(3):3406–3420.

Tetarenko, B. E., Sivakoff, G. R., Heinke, C. O., and Gladstone, J. C. (2016). WATCH-DOG: A Comprehensive All-sky Database of Galactic Black Hole X-ray Binaries. *ApJs*, 222(2):15.

Theuns, T. and Jorissen, A. (1993). Wind accretion in binary stars - I. Intricacies of the flow structure. *MNRAS*, 265:946–967.

Thomas, N. T., Gudennavar, S. B., Misra, R., and Bubbly, S. G. (2019). AstroSat observation of the newly discovered transient X-ray binary source: MAXI J0637-430. *The Astronomer's Telegram*, 13296:1.

Titarchuk, L. and Fiorito, R. (2004). Spectral Index and Quasi-Periodic Oscillation Frequency Correlation in Black Hole Sources: Observational Evidence of Two Phases and Phase Transition in Black Holes. *ApJ*, 612(2):988–999.

Tomsick, J. A., Corbel, S., Goldwurm, A., and Kaaret, P. (2005). X-Ray Observations of the Black Hole Transient 4U 1630-47 during 2 Years of X-Ray Activity. *ApJ*, 630(1):413–429.

Tomsick, J. A., Garcia, J., Fabian, A., Walton, D., Jiang, J., Fuerst, F., Buisson, D., Shaw, A., Hare, J., Bachetti, M., Connors, R., Gandhi, P., and Xu, Y. (2019). A NuSTAR Observation of MAXI J0637-430: A New X-ray Transient and Likely Black Hole X-ray Binary. *The Astronomer's Telegram*, 13270:1.

Tomsick, J. A., Lapshov, I., and Kaaret, P. (1998). An X-Ray Dip in the X-Ray Transient 4U 1630-47. *ApJ*, 494(2):747–752.

Tomsick, J. A., Nowak, M. A., Parker, M., Miller, J. M., Fabian, A. C., Harrison, F. A., Bachetti, M., Barret, D., Boggs, S. E., Christensen, F. E., Craig, W. W., Forster, K., Fürst, F., Grefenstette, B. W., Hailey, C. J., King, A. L., Madsen, K. K., Natalucci, L., Pottschmidt, K., Ross, R. R., Stern, D., Walton, D. J., Wilms, J., and Zhang, W. W.

(2014). The Reflection Component from Cygnus X-1 in the Soft State Measured by NuSTAR and Suzaku. *ApJ*, 780(1):78.

Tomsick, J. A., Shaw, A., Gandhi, P., Rahoui, F., and Dincer, T. (2017). Increasing X-ray/UV flux from Swift J1753.5-0127. *The Astronomer's Telegram*, 10114:1.

Trudolyubov, S. P., Borozdin, K. N., and Priedhorsky, W. C. (2001). RXTE observations of 4U 1630-47 during the peak of its 1998 outburst. *MNRAS*, 322(2):309–320.

Vadawale, S. V., Rao, A. R., Bhattacharya, D., Bhalerao, V. B., Dewangan, G. C., Vibhute, A. M., Mithun, N. P. S., Chattopadhyay, T., and Sreekumar, S. (2016). *In-orbit performance AstroSat CZTI*, volume 9905 of *Society of Photo-Optical Instrumentation Engineers (SPIE) Conference Series*, page 99051G.

Vahdat Motlagh, A., Kalemci, E., and Maccarone, T. J. (2019). Investigating state transition luminosities of Galactic black hole transients in the outburst decay. *MNRAS*, 485(2):2744–2758.

van Paradijs, J. (1996). On the Accretion Instability in Soft X-Ray Transients. *ApJL*, 464:L139.

Verner, D. A., Ferland, G. J., Korista, K. T., and Yakovlev, D. G. (1996). Atomic Data for Astrophysics. II. New Analytic FITS for Photoionization Cross Sections of Atoms and Ions. *ApJ*, 465:487.

Wang, J., Mastroserio, G., Kara, E., García, J. A., Ingram, A., Connors, R., van der Klis, M., Dauser, T., Steiner, J. F., Buisson, D. J. K., Homan, J., Lucchini, M., Fabian, A. C., Bright, J., Fender, R., Cackett, E. M., and Remillard, R. A. (2021). Disk, Corona, Jet Connection in the Intermediate State of MAXI J1820+070 Revealed by NICER Spectral-timing Analysis. *ApJL*, 910(1):L3.

Wardziński, G., Zdziarski, A. A., Gierliński, M., Grove, J. E., Jahoda, K., and Johnson, W. N. (2002). X-ray and γ-ray spectra and variability of the black hole candidate GX 339-4. *MNRAS*, 337(3):829–839.

White, N. E. and Marshall, F. E. (1983). Potential Black-Hole Candidates. *IAUCirc*, 3806:2.

Wijnands, R. and van der Klis, M. (1999). The Broadband Power Spectra of X-Ray Binaries. *ApJ*, 514(2):939–944.

Wilms, J., Allen, A., and McCray, R. (2000). On the Absorption of X-Rays in the Interstellar Medium. *ApJ*, 542(2):914–924.

Xu, Y., Harrison, F. A., García, J. A., Fabian, A. C., Fürst, F., Gandhi, P., Grefenstette, B. W., Madsen, K. K., Miller, J. M., Parker, M. L., Tomsick, J. A., and Walton, D. J. (2018a). Reflection Spectra of the Black Hole Binary Candidate MAXI J1535-571 in the Hard State Observed by NuSTAR. *ApJL*, 852(2):L34.

Xu, Y., Harrison, F. A., Kennea, J. A., Walton, D. J., Tomsick, J. A., Miller, J. M., Barret, D., Fabian, A. C., Forster, K., Fürst, F., Gandhi, P., and García, J. A. (2018b). The Hard State of the Highly Absorbed High Inclination Black Hole Binary Candidate Swift J1658.2-4242 Observed by NuSTAR and Swift. *ApJ*, 865(1):18.

Yadav, J. S., Chauhan, J. V., Agrawal, P. C., Antia, H. M., Pahari, M., Chitnis, V. R., Misra, R., Dedhia, D., Katoch, T., Madhwani, P., Manchanda, R. K., Paul, B., Shah, P., Altamirano, D., Gandhi, P., Navalgund, K. H., Sarma, K. S., Seetha, S., and Subbarao, K. (2016). AstroSat/LAXPC observed 4U 1630-472 on very first day of a new outburst. *The Astronomer's Telegram*, 9515:1.

Zdziarski, A. A., Johnson, W. N., and Magdziarz, P. (1996). Broad-band γ-ray and X-ray spectra of NGC 4151 and their implications for physical processes and geometry. *MNRAS*, 283(1):193–206.

Zdziarski, A. A., Szanecki, M., Poutanen, J., Gierliński, M., and Biernacki, P. (2020). Spectral and temporal properties of Compton scattering by mildly relativistic thermal electrons. *MNRAS*, 492(4):5234–5246.

Zhang, G. B., Bernardini, F., Russell, D. M., Gelfand, J. D., Lasota, J. P., Qasim, A. A., AlMannaei, A., Koljonen, K. I. I., Shaw, A. W., Lewis, F., Tomsick, J. A., Plotkin, R. M., Miller-Jones, J. C. A., Maitra, D., Homan, J., Charles, P. A., Kobel, P., Perez, D., and Doran, R. (2019). Bright Mini-outburst Ends the 12 yr Long Activity of the Black Hole Candidate Swift J1753.5-0127. *ApJ*, 876(1):5.

Zhang, G. B., Qu, J. L., Zhang, S., Zhang, C. M., Zhang, F., Chen, W., Song, L. M., and Yang, S. P. (2007). X-Ray Spectral and Timing Properties of the Black Hole X-Ray Transient SWIFT J1753.5-0127. *ApJ*, 659(2):1511–1518.

Zhang, W., Jahoda, K., Swank, J. H., Morgan, E. H., and Giles, A. B. (1995). Dead-Time Modifications to Fast Fourier Transform Power Spectra. *ApJ*, 449:930.

Zurita, C., Durant, M., Torres, M. A. P., Shahbaz, T., Casares, J., and Steeghs, D. (2008). Swift J1753.5-0127: The Black Hole Candidate with the Shortest Orbital Period. *ApJ*, 681(2):1458–1463.

Życki, P. T., Done, C., and Smith, D. A. (1999). The 1989 May outburst of the soft X-ray transient GS 2023+338 (V404 Cyg). *MNRAS*, 309(3):561–575.

*I have learned that I still have a lot to learn....*

**-Maya Angelou**